NeuroImage 298 (2024) 120793

Contents lists available at ScienceDirect

NeuroImage

journal homepage: www.elsevier.com/locate/ynimg

Review

A comprehensive overview of diffuse correlation spectroscopy: Theoretical framework, recent advances in hardware, analysis, and applications

Quan Wang [a], Mingliang Pan [a], Lucas Kreiss [b], Saeed Samaei [c,f], Stefan A. Carp [d], Johannes D. Johansson [e], Yuanzhe Zhang [a], Melissa Wu [b], Roarke Horstmeyer [b], Mamadou Diop [c,f], David Day-Uei Li [a,*]

[a] Department of Biomedical Engineering, Faculty of Engineering, University of Strathclyde, Glasgow, United Kingdom
[b] Department of Biomedical Engineering, Duke University, Durham, NC, United States
[c] Department of Medical and Biophysics, Schulich School of Medical & Dentistry, Western University, London, Ontario, Canada
[d] Massachusetts General Hospital, Optics at Athinoula A. Martinos Center for Biomedical Imaging, Harvard Medical School, Charlestown, MA, United States
[e] Department of Biomedical Engineering, Linköping University, Linköping, Sweden
[f] Lawson Health Research Institute, Imaging Program, London, Ontario, Canada

ARTICLE INFO

Keywords:
Diffuse correlation spectroscopy (DCS)
Continuous-wave
Time-domain
Frequency domain
Blood flow indices
Clinical application
Near-infrared

ABSTRACT

Diffuse correlation spectroscopy (DCS) is a powerful tool for assessing microvascular hemodynamic in deep tissues. Recent advances in sensors, lasers, and deep learning have further boosted the development of new DCS methods. However, newcomers might feel overwhelmed, not only by the already-complex DCS theoretical framework but also by the broad range of component options and system architectures. To facilitate new entry to this exciting field, we present a comprehensive review of DCS hardware architectures (continuous-wave, frequency-domain, and time-domain) and summarize corresponding theoretical models. Further, we discuss new applications of highly integrated silicon single-photon avalanche diode (SPAD) sensors in DCS, compare SPADs with existing sensors, and review other components (lasers, sensors, and correlators), as well as data analysis tools, including deep learning. Potential applications in medical diagnosis are discussed and an outlook for the future directions is provided, to offer effective guidance to embark on DCS research.

1. Introduction

Blood flow (BF) in a healthy person ensures stable delivery of oxygen and energy substrates (glucose and lactate) to and timely removal of metabolic waste products from organs (Zauner et al., 2002). Specifically, well-regulated cerebral blood flow (CBF) ensures healthy brain functions (Uludağ et al., 2004; Durduran and Yodh, 2014), brain metabolisms (Kaiser and During, 1995; Devor et al., 2012), and supports metabolic responses to external stimuli (Cheung et al., 2001; Quaresima et al., 2012). The average CBF for an adult human is around 50 ml/(100 g min) (Fantini et al., 2016) and 10-30 ml/(100 g min) for a newborn (Rhee et al., 2018). Irregular CBF can cause brain damage through ischemic injury or stroke (Campbell et al., 2013; Durduran et al., 2009).

Effective real-time BF monitoring can aid in the diagnosis and management of broad range of medical conditions such as stroke, traumatic or hypoxic-ischemic encephalopathy (HIE) (Weigl et al., 2016; Durduran et al., 2004), neurological disorders, cardio-cerebral diseases, cancer treatment strategies, tissue perfusion in peripheral vascular diseases (Ma et al., 2019), brain health/functions (Duncan et al., 1996), wound healing, sepsis and shock (Becker et al., 2004), skeletal muscle (Gurley et al., 2012) injuries or tissue viability during surgeries.

Available real-time BF measurement tools are predominantly Doppler ultrasound based. However, Doppler ultrasonography requires a highly-skilled operator at the bedside and is operator-dependent (Tupprasoot and Blaise, 2023). Cerebral perfusion can be mapped using medical imaging scanners, including positron emission tomography (PET) (Vaquero and Kinahan, 2015), single photon emission computed tomography (SPECT) (Ljungberg and Pretorius, 2018), xenon-enhanced computed tomography (XeCT) (Yonas et al., 1996), dynamic susceptibility contrast magnetic resonance imaging (DSC-MRI) (Kwong et al., 1992), and arterial spin labelling MRI (ASL-MRI) (Barbier et al., 2001; Durduran et al., 2010; Yu et al., 2007). However, these techniques only provide 'snapshot' observations, are inappropriate for continuous monitoring, and typically require moving patients to

* Corresponding author.
E-mail address: David.Li@strath.ac.uk (D.D.-U. Li).

https://doi.org/10.1016/j.neuroimage.2024.120793
Received 19 May 2024; Received in revised form 23 July 2024; Accepted 14 August 2024
Available online 15 August 2024

Glossary

DCS	diffuse correlation spectroscopy
DCT	diffuse correlation tomography
SPAD	single-photon avalanche diode
APD	avalanche photon diode
PMT	photomultiplier
SNSPD	superconducting nanowire single-photon detector
DL	deep learning
BF	blood flow
BFi	blood flow index
CBF	cerebral blood flow
PET	positron emission tomograph
SPECT	single photon emission computed tomograph
XeCT	xenon-enhanced computed tomography
MRI	magnetic resonance imaging
DSC-MRI	dynamic susceptibility contrast magnetic resonance imaging
LDF	laser Doppler flowmetry
NIR	near-infrared
NIRS	near-infrared spectroscopy
DOS	diffuse optical spectroscopy
CBV	cerebral blood volume
FCS	fluorescence correlation spectroscopy
DLS	dynamic light scattering
QELS	Quasi-elastic light
CHS	coherent hemodynamics spectroscopy
RBC	red blood cells
AI	artificial intelligence
CMOS	complementary metal-oxide-semiconductor
CW	continuous wave
TD	time domain
FD	frequency domain
RTE	radiative transfer equation
PDE	**photon diffuse equation** (Section 2); **Photon detection efficiency** of detectors (Section 3)
CTE	correlation transport equation
CDE	correlation diffusion equation
MRI-ASL	MRI-based arterial spin labelling
RF	radio-frequency
ANSI	American National Standards Institute
MPE	maximal permissible exposure
LSCA	laser speckle contrast analysis
LSCI	laser speckle contrast imaging
DSCA	diffuse speckle contrast analysis
SCOS	speckle contrast optical spectroscopy
DWS	diffusing wave spectroscopy
DUS	Doppler ultrasound
PDT	photodynamic therapy
TCD	transcranial Doppler ultrasound
pO_2	oxygen partial pressure
$CMRO_2$	cerebral metabolic rate of oxygen
FPGA	field programmable gate arrays
D	core diameter of multimode fiber
d	speckle diameter
SNR	signal to noise ratio
g	anisotropy factor
μ_s	scattering coefficient
μ_s'	reduced scattering coefficient
$\langle \Delta r^2(\tau) \rangle$	mean square displacement of moving scatterers
D_B	effective diffusion coefficient for moving particles
V^2	mean square velocity
r_1	distance between the detector and an approximated positive isotropic imaging source for a semi-infinite geometry
r_2	distance between the detector and an approximated negative isotropic imaging source for a semi-infinite geometry
$G1/g1$	unnormalized/normalized electric field autocorrelation function
$G2/g2$	unnormalized/normalized intensity autocorrelation function
λ	wavelength
k_0	wavenumber in the medium
n	refraction index
α	fraction of scattering events due to dynamic
β	coherent factor
τ	correlation delay time
R_{eff}	effective reflection coefficient
ρ	distance between source and detection fibers
J_0	the zeros order Bessel function of the first kind
s_0	point-like monochromatic light source
l_c	coherence length
$\Delta\lambda$	the optical bandwidth
w	frequency corresponding to time in Fourier domain
q	the radial spatial frequency
p	layer number of tissues
ω	the source modulation frequency
T	the correlator bin time interval
T_{int}	integration time (measurement duration) or the measurement time window
τ_c	decay constant
$\langle M \rangle$	average number of photons within bin time T
I	detected photon count
m	bin index
s	photon pathlength
ToF	time-of-flight
t	photon time-of-flight
NL	Nth-order
SVR	support vector regression
EEG	electroencephalogram
ECG	electrocardiogram
2DCNN	2-dimentional convolution neural networks
3D	three-dimensional
LSTM	long short-term memory
RNN	recurrent neural network
StO_2	cerebral tissue oxygenation

imaging suites, which is unpractical for many patients. Additionally, a supine scan is necessary for MRI, PET and CT techniques. Further, PET, SPECT, and CT present additional risks of radiation exposure. Laser Doppler flowmetry (LDF) (Shepherd and Öberg, 2013) is another perfusion technique, but it can only measure superficial tissue blood flow; thus, tissue samples must be thin to permit adequate sampling. Thus, there is a critical need to develop bedside techniques that are free from the limitations mentioned above and can noninvasively monitor microvascular BF in deep tissue at the bedside with a high sampling rate and at a low cost. For a thorough comparison of the modalities mentioned above, readers can refer to previous reviews (Durduran and Yodh, 2014; Fantini et al., 2016; Wintermark et al., 2005).

In the late 1970s, Jöbsis observed a spectral window in the near-infrared (low optical absorption, μ_a and reduced scattering, μ_s', ~ 650-950 nm) wherein photons can penetrate deep/thick tissues up to several centimetres (Jöbsis, 1977; Jöbsis-vanderVliet and Jöbsis, 1999;

Jöbsis-vanderVliet, 1999). Subsequently, near-infrared spectroscopy (NIRS) or diffuse optical spectroscopy (DOS) was applied to study deep tissue hemodynamics, including cerebral oxygenation and cerebral blood volume (CBV), as early as the mid-1980s (Benaron et al., 1992; Pope and Stevens, 1953). However, traditional NIRS primarily measures blood oxygenation saturation and hemoglobin concentrations, instead of tissue blood flow. Although NIRS can estimate tissue perfusion, this requires injecting exogenous contrast agents (such as indocyanine green) (Habazettl et al., 2010; Hawrysz and Sevick-Muraca, 2000; Keller et al., 2003), limiting its applications in continuous monitoring.

Diffuse light correlation techniques, on the other hand, are rooted in the fundamental principles of dynamic light scattering (DLS). These methods, sometimes called 'quasi-elastic light (QELS) scattering' techniques (Berne and Pecora, 1990; Chu, 1991; Clark et al., 1970; Van de Hulst, 1981), measure light intensity fluctuations scattered from samples to observe motions of sample constituents, e.g., Brownian motions of particles or macromolecules. Conventionally, DLS can provide detailed information about the dynamics of scattering media by using photon correlation techniques to analyze scattered light fluctuations (Berne and Pecora, 2000). However, QELS belongs to the single-scattering regime (Clark et al., 1970; Fuller et al., 1980) and is unsuitable for turbid media in which the incident light is scattered multiple times. In 1987, Maret and Wolf (Maret and Wolf, 1987) reported experimental measurements of the intensity autocorrelation function in the multiple-scattering regime and suggested a simple method for analyzing the measurements. One year later, Stephen derived a theoretical framework that extends QELS to the multiple-scattering regime (Stephen, 1988).

Near-infrared diffuse correlation spectroscopy (DCS), also known as diffusing wave spectroscopy (DWS) (Pine et al., 1990; Maret and Wolf, 1987) relates multi-scattered light's fluctuations to the underlying dynamics of scattering media. Despite the name, DCS is not a traditional spectroscopic technique (Liu et al., 2019; Liu et al., 2018; Liu et al., 2020) that uses multiple wavelengths; instead, it is a laser speckle method that analyzes light scattered over long distances through tissue. DCS, LDF (Fredriksson et al., 2007; Vo-Dinh, 2014), laser speckle contrast imaging (LSCI) (Briers et al., 2013), and diffuse speckle contrast analysis (DSCA) (Bi et al., 2013b; Bi et al., 2013a; Bi et al., 2024) are all based on laser speckles. The term 'DCS', first coined by Yodh's group in 2001 (Cheung et al., 2001), has gained popularity as it provides a theoretical framework that describes the underlying phenomenon using the popular diffuse approximation to the radiative transfer equation. Notably, a comprehensive diffuse correlation theory of diffuse speckle fields for predicting particle motions in highly scattered media was first introduced by Boas and Yodh in 1995 (Boas et al., 1995; Boas et al., 1996). The DCS theoretical model can be used to estimate deep-tissue microvascular blood flow index (BFi), which is a good surrogate for *in vivo* BF (Boas et al., 2016). In the last two decades, DCS technologies have been further developed (Boas et al., 1996; Boas et al., 1995; Boas and Yodh, 1997), validated, and employed for non-invasive BF

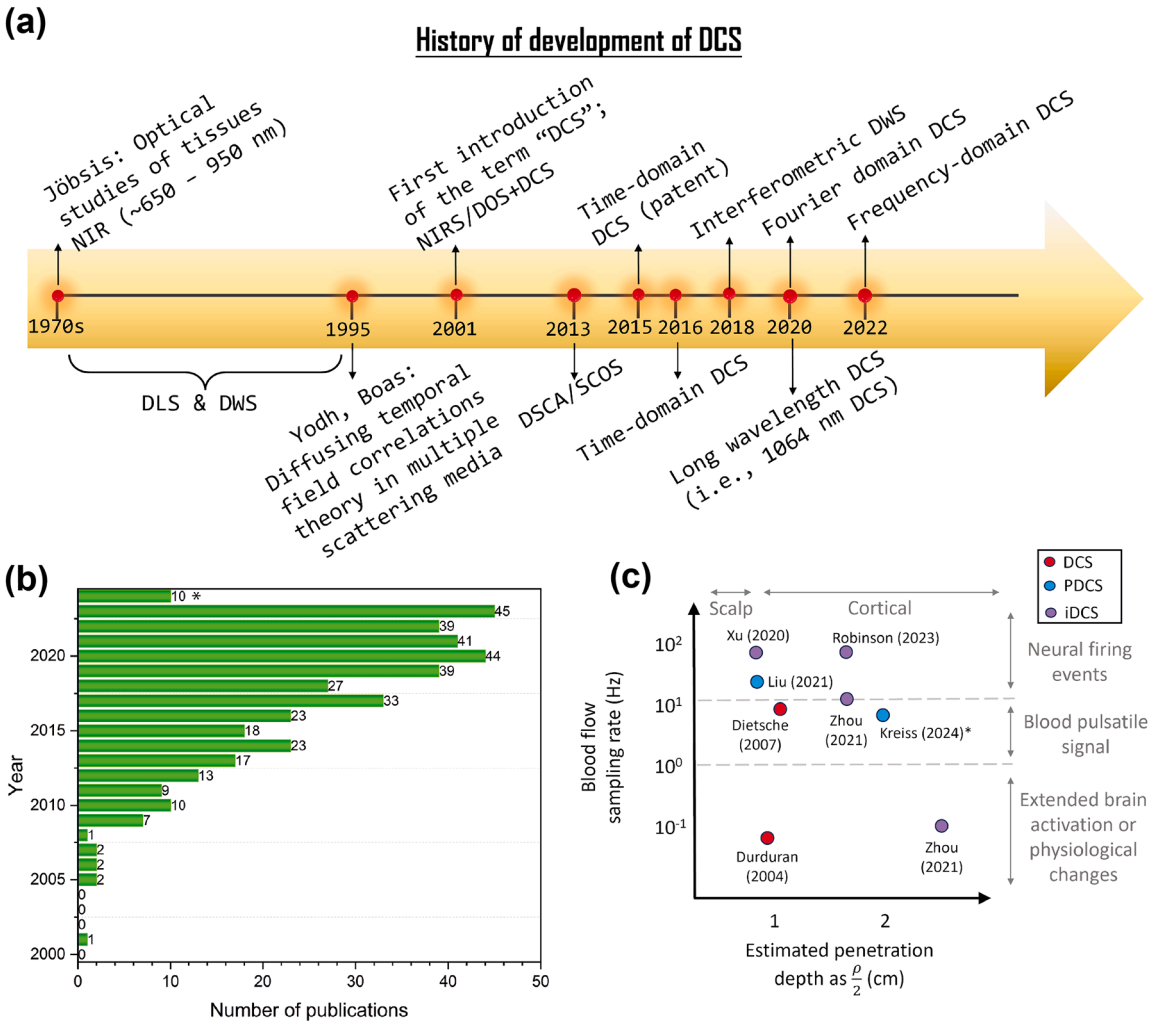

Fig. 1. (a) The roadmap of DCS historical development; (b) the number of published DCS papers based on PUBMED (*value for 2024 extrapolated as of the date of writing); (c) blood flow sampling rate vs measurement depths. PDCS: parallelized DCS, iDCS: interferometric DCS.

measurements in deep tissue (up to ~ 2 centimeters (Kreiss et al., 2024; Zhou et al., 2021; Mattioli della Rocca et al., 2024)), such as skin, muscle (Yu et al., 2007; Yu et al., 2005; Belau et al., 2010; Shang et al., 2010; Yu et al., 2011; Munk et al., 2012; Guoqiang Yu, 2013; Quaresima et al., 2019), breast tumor (Yazdi et al., 2017; Grosenick et al., 2016; He et al., 2015; Choe et al., 2014; Chung et al., 2015; Zhou et al., 2007; Durduran et al., 2005) and the brain (Durduran et al., 2009; Durduran et al., 2004; Cheung et al., 2001; Culver et al., 2003; Li et al., 2005; Zhou et al., 2006; Kim et al., 2010; Buckley et al., 2009). In 2001, the combination of DCS with NIRS/DOS was first introduced for cerebral monitoring in rats (Cheung et al., 2001) and then in adult brains in 2004 (Durduran et al., 2004). This combination allows for simultaneous monitoring of tissue BF and oxygenation.

A diagram of the history of DCS development is shown in Fig. 1(a). Fig. 1(b) displays the number of DCS publications over the past 20 years, with more than 400 publications to date (we only counted articles containing "DCS"). Fig. 1(c) presents DCS measurements from human brain tissue, organizing current studies by ρ (x-axis) and the blood flow sampling rate (y-axis). It highlights the trend of using parallel or multispeckle and interferometric DCS for higher sampling rates at a larger ρ and indicates the required penetration depth.

Fig. 2 illustrates the principle of DCS. Briefly, a long-coherence laser emits NIR light through an optical fiber to the tissue, Fig. 2(a), and the recorded light intensity exhibits temporal fluctuations, Fig. 2(b). These fluctuations are attributed to the motion of moving scatterers, such as red blood cells (RBC). To quantify the motion of RBC, a hardware or software correlator calculates the normalized intensity autocorrelation, $g_2(\tau)$ as shown in Fig. 2(c). Typically, DCS systems are implemented in a reflection geometry, where a source and a detector are placed at a finite distance, ρ. Photons travelling from the source to the detector follow a "banana-shaped", stochastic scattering profile, as shown in Fig. 2(d), where the penetration depth of these DCS instruments is roughly between $\rho/3 \sim \rho/2$)(Buckley et al., 2014). Fig. 2(c) and (e) show that the $g_2(\tau)$ curves decay faster with increased flow or ρ. The slope or the decay rate provides information about the optical properties and the motion of the scatters. The largest ρ in the current state-of-the-art is 4 cm, corresponding to a depth of about 2 cm (Kreiss et al., 2024; Mattioli della Rocca et al., 2024).

Although there have been around 15 review DCS papers (Durduran and Yodh, 2014; Fantini et al., 2016; Buckley et al., 2014; Mesquita et al., 2011; Yu, 2012; Yu, 2012; Zhou et al., 2022; Ayaz et al., 2022; Li et al., 2022; Carp et al., 2023; James and Munro, 2023; Durduran et al., 2010; Lee, 2020; Shang et al., 2017; Bi et al., 2015) in the last two decades, new approaches have emerged, including theoretical layered models, artificial intelligence (AI) methods for DCS analysis, and the use of novel sensors like highly integrated complementary metal-oxide-semiconductor (CMOS) single-photon avalanche diodes (SPAD) cameras. These aspects were not covered in previous reviews, which is why this review summarizes and systematically compares various analytical layered models, including continuous-wave (CW)-, time-domain (TD)-DCS, AI-enhanced DCS analysis methods, as well as the use of SPAD cameras in DCS. Furthermore, we also derived analytical models for the frequency domain (FD)-DCS, which was newly introduced in 2022 (Moka et al., 2022). The main contributions of this review include:

- We thoroughly derive and compare different layered analytical models used in CW-, TD-, and FD-DCS, highlighting their strengths and applications (Section 2).
- Section 3.3 examines new applications of CMOS SPAD cameras and compares them with existing sensors used in DCS..
- Section 3.5 compares TD-DCS and CW-DCS systems and emphasizes the benefits of TD-DCS and its potential for future development.
- We discuss novel AI-enhanced DCS analysis strategies, addressing their effectiveness and potential (Section 4).
- Discussion and outlooks are provided in Section 6.

This review aims to serve as a practical information resource for researchers and newcomers venturing into the field, offering a clearer understanding of the evolving DCS landscape and equipping them with the necessary knowledge to navigate it effectively.

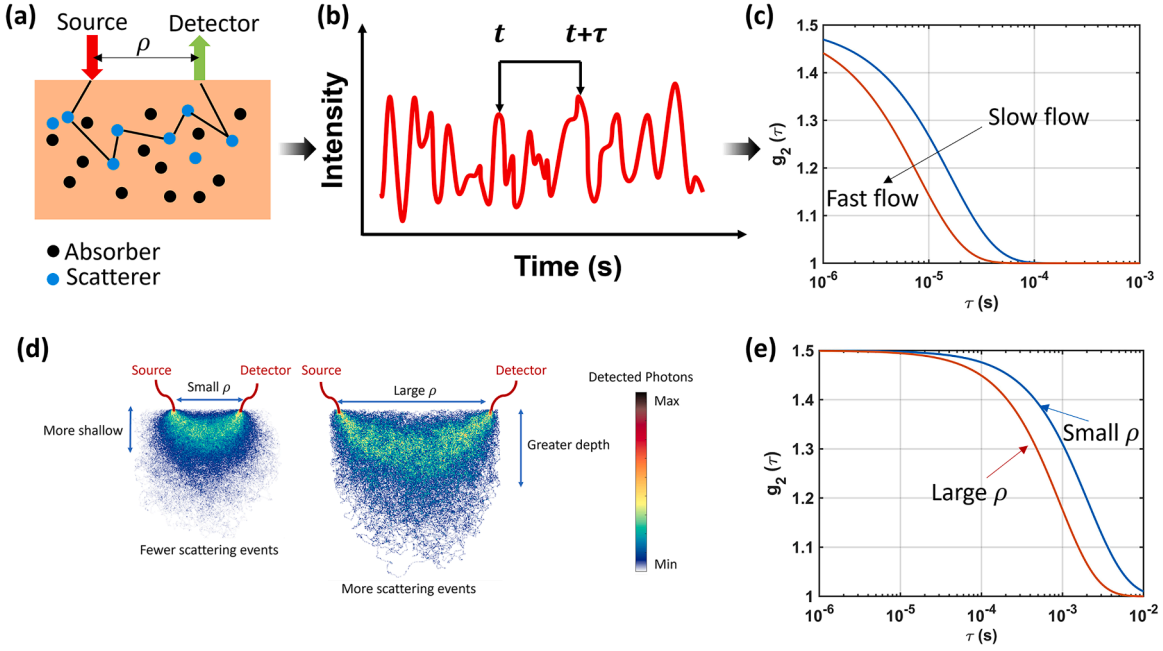

Fig. 2. The DCS principle for blood flow measurements. (a) The schematic of DCS measurements in the semi-infinite geometry. Highly coherent laser light is used to illuminate the sample via optical fibers. The source and detector fibers are placed on the tissue surface within a distance ρ; (b) the scattered light intensity fluctuates due to moving scatterers (e.g., red blood cells); (c) two intensity autocorrelation curves ($g_2(\tau)$) showing different flow rates. (d) Photons scattered from moving particles travel along "banana-shaped" paths between source and detection fibers; (e) Autocorrelation functions for different ρ.

2. Theory background

The propagation of light in highly scattering media such as biological tissues can be characterized by an absorption coefficient μ_a and a reduced scattering coefficient μ_s' using the radiative transfer equation (RTE) (Durduran et al., 2010). Similarly, to study the photon propagation under dynamic scatterers, the correlation transport equation (CTE) (Durduran and Yodh, 2014; Mesquita et al., 2011) is adopted to obtain the field (electrical) autocorrelation function $G_1(\tau)$ under general conditions of photon migration. The primary difference between the CTE and RTE lies in the fact that CTE describes the time-dependent specific intensity, reflecting an angular spectrum of the mutual coherence function. In the NIR spectral window, the unnormalized $G_1(\tau)$ can be expressed as, $G_1^T(\boldsymbol{r},\hat{\Omega},\tau) = \langle E(\boldsymbol{r},\hat{\Omega},t)\cdot E^*(\boldsymbol{r},\hat{\Omega},t+\tau)\rangle$, where $\langle\cdots\rangle$ denotes a time average. $E(\boldsymbol{r},\hat{\Omega},t)$ is the electric field at the position $\boldsymbol{r}$ and time t propagating in the $\hat{\Omega}$ direction, inside the tissue that can be described by CTE (Ackerson et al., 1992; Dougherty et al., 1994; Boas and Yodh, 1997) applicable for CW systems analogous to RTE:

$$\nabla\cdot G_1^T(\boldsymbol{r},\hat{\Omega},\tau)\hat{\Omega} + \mu_t G_1^T(\boldsymbol{r},\hat{\Omega},\tau) = S(\boldsymbol{r},\hat{\Omega}) + \mu_s\int G_1^T(\boldsymbol{r},\hat{\Omega}',\tau)g_1^s(\hat{\Omega},\hat{\Omega}',\tau)f(\hat{\Omega},\hat{\Omega}')d\hat{\Omega}', \tag{1}$$

where $\mu_t = \mu_s + \mu_a$ is the transport coefficient. $S(\boldsymbol{r},\hat{\Omega})$ is the source distribution; $g_1^s(\hat{\Omega},\hat{\Omega}',\tau)$ is the normalized field correlation function for single scattering; and $f(\hat{\Omega},\hat{\Omega}')$ is the normalized differential cross-section.

For a time dependent source, Eq. (1) becomes:

$$\nabla\cdot G_1^T(\boldsymbol{r},\hat{\Omega},\tau,t)\hat{\Omega} + \mu_t G_1^T(\boldsymbol{r},\hat{\Omega},\tau,t) + \frac{1}{v}\frac{\partial}{\partial t}G_1^T(\boldsymbol{r},\hat{\Omega},\tau,t) = S(\boldsymbol{r},\hat{\Omega},\ t) + \mu_s\int G_1^T(\boldsymbol{r},\hat{\Omega}',\tau,\ t)g_1^s(\hat{\Omega},\hat{\Omega}',\tau,t)f(\hat{\Omega},\hat{\Omega}')d\hat{\Omega}', \tag{2}$$

where v is the light speed in the medium.

DCS BF measurements can be analyzed using the correlation diffusion equation (CDE) (Durduran and Yodh, 2014; Boas et al., 1995), derived from CTE using the standard diffusion approximation. The derivation procedure is summarized in Fig. 3.

Furthermore, DCS instruments can be divided into three categories according to the light illumination strategy. The most straightforward approach is employing a CW laser, as the instrumentation is relatively simple. The frequency-domain approach utilizes an amplitude-modulated laser, with the modulation frequency set to a radio-frequency (RF) ranging (from tens to a thousand MHz). In contrast, the time-domain (TD) approach uses a short pulse laser and measures the delayed and temporally broadened output pulse. Time domain measurements have the most information content; however, they are more complex and expensive than the other two methods.

The depth sensitivity of the DCS measurements can be improved using advanced techniques, such as TD- and FD-DCS. However, it may not be sufficient to minimize the superficial layer contamination. For this aim, different analytical models have been introduced to account for the contribution of the individual layers. These models typically include parameters of the optical system (e.g., the wavelength) and presumptions of optical tissue properties (e.g., μ_a, μ_s', n) to fit mathematical models to the measurements. A summary of the analytical models commonly used in DCS analysis is shown in Fig. 4.

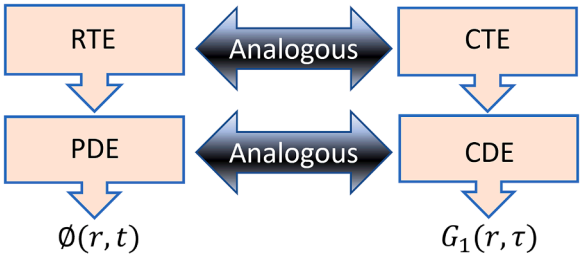

Fig. 3. Green's function for DCS derivation process.

2.1. CW Semi-infinite homogenous (one layer) model

In traditional DCS systems, the tissue is commonly considered a homogenous semi-infinite medium, as shown in Fig. 4(a). Under the standard diffusion approximation (Boas, 1996), we reduce Eq. (1) to CDE as:

$$\left(-\frac{D(\boldsymbol{r})}{v}\nabla^2 + \mu_a + \frac{1}{3}\alpha\mu_s' k_0^2\langle\Delta r^2(\tau)\rangle\right)G_1(\boldsymbol{r},\tau) = S(\boldsymbol{r}), \tag{3}$$

where $G_1(\boldsymbol{r},\tau) \equiv \left\langle \vec{E}(\boldsymbol{r},\tau)\cdot\vec{E}^*(\boldsymbol{r},t+\tau)\right\rangle$ is the electric field autocorrelation function. $D(\boldsymbol{r}) = v/(3\mu_s')$ is the photon diffusion coefficient, v is the speed of light in the medium, and $\mu_s' = \mu_s(1-g)$ is the reduced scattering coefficient, where $g \equiv \langle cos\theta\rangle$ (ranging from -1 to 1) is the scattering anisotropy factor. k_0 is the wavenumber in the medium, α represents the probability that a light scattering event is with a moving scatterer (e.g., a flowing red blood cell (RBC)), and $\langle\Delta r^2(\tau)\rangle$ represents the mean square displacement of moving scatterers, and is commonly described using two different models, including the Brownian motion and random ballistic models in biological tissues. For the Brownian motion, $\langle\Delta r^2(\tau)\rangle = 6D_B\tau$ (Maret and Wolf, 1987), where D_B is an 'effective' diffusion coefficient for moving particles. For random ballistic flow, $\langle\Delta r^2(\tau)\rangle = 6V^2\tau^2$, where V^2 is the mean square velocity of the scatterer in the vasculature. The relationships between the RBC movements and the flow models (random ballistic flow and Brownian motion) have already been investigated (Boas et al., 2016; Zhu et al., 2020; Sie et al., 2020).

In particular, for a semi-infinite, homogenous system with a point source $S(\boldsymbol{r}) = S_0\delta(\boldsymbol{r})$, $G_1(\boldsymbol{r},\tau)$ is the solution of Eq. (3), obtained using an image source approach following Kienle and Patterson (Kienle and Patterson, 1997) as,

$$G_1(\vec{r},\tau) = \frac{3\mu_s' S_0}{4\pi}\left[\frac{exp(-Kr_1)}{r_1} - \frac{exp(-Kr_2)}{r_2}\right], \tag{4}$$

where $K = \sqrt{3\mu_s'\mu_a + \alpha\mu_s'^2 k_0^2\langle\Delta r^2(\tau)\rangle}$, r_1 and r_2 are the distances between the detector and the source/image source, respectively. $r_1 = \sqrt{\rho^2 + z_0^2}$ and $r_2 = \sqrt{\rho^2 + (z_0 + 2z_b)^2}$; $z_0 = 1/\mu_s'$ is the depth at which a collimated source on the tissue surface can be approximated as a point source; $z_b = 2(1 + R_{eff})/3\mu_s'(1 - R_{eff})$ and $R_{eff} = -1.440n^{-2} + 0.71n^{-1} + 0.668 + 0.0636n$ is the effective reflection coefficient, $n = \frac{n_{tissue}}{n_{air}} \approx 1.33$. Typically, αD_B is referred to as the blood flow index (BFi) in biological tissues (Durduran, 2004). In practice, the Brownian model can fit the observed correlation decay curves better over a wide range of tissue types, including rat (Culver et al., 2003; Zhou et al., 2006; Cheung et al., 2001; Carp et al., 2010), piglet (Zhou et al., 2009; Forti et al., 2023), human brains (Durduran et al., 2004; Jaillon et al., 2007; Dietsche et al., 2007; Koban et al., 2010; Zirak et al., 2010; Edlow et al., 2010), mouse tumours (Yu et al., 2005; Sunar et al., 2007), human skeletal muscles (Yu et al., 2007; Yu et al., 2005; Belau et al., 2010; Shang et al., 2010; Shang et al., 2009), and human tumors (Durduran et al., 2005; Sunar et al., 2006; Yu et al., 2006; Dong et al., 2012).

2.2. CW two-layer model

We have stated above that the DCS theory is based on the correlation transport (Boas et al., 1995; Ackerson et al., 1992; Dougherty et al.,

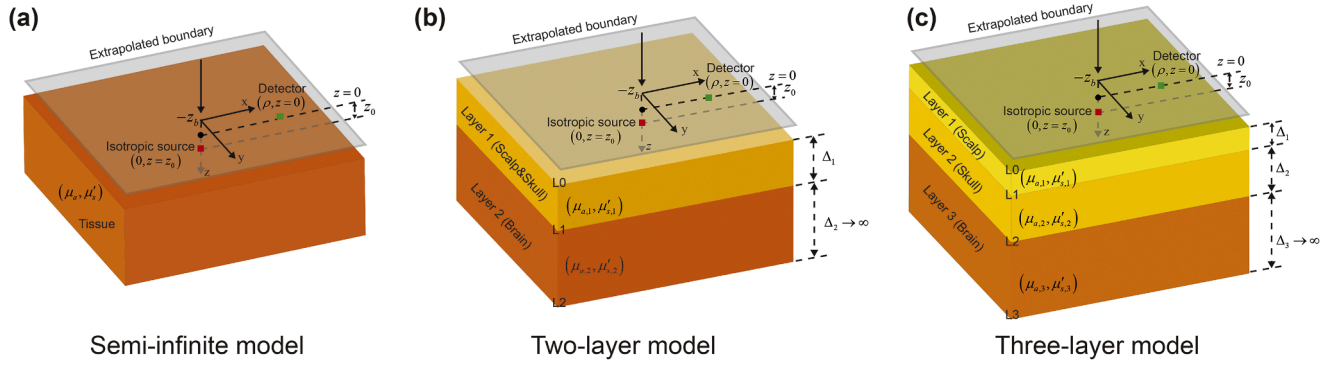

Fig. 4. Analytical models including the source and the detector for DCS (a) homogenous semi-infinite model, (b) two-layer analytical model, (c) three-layer analytical model. Here, $\mu_{a(n)}$ and $\mu_{s(n)}^{'}$ are the absorption and reduced scattering coefficients in the *n-th* layer, respectively. Δ_i is the thickness of Layer *i*.

1994), approximated by CDE (Boas and Yodh, 1997, Boas, 1996). By assuming that light propagates in a homogenous medium, the simple solution of Eq. (3) has been widely used in the DCS community (Durduran, 2004). However, biological tissues (Kienle et al., 1998) are usually layered encompassing unique physiological and optical properties (Gagnon et al., 2008b, Lesage et al., 2008). For example, the simple two-layer model is useful in cerebral blood flow monitoring in newborns, especially preterm infants, because their skull and scalp are relatively thin, allowing clear differentiation between the superficial scalp layer and the deeper brain tissue layer. Gagnon et al. (2008a) first proposed a two-layer analytical model, based on Kienle *et al.*'s model for reflectance spectroscopy with the two-layered geometry in Fig. 4(b).

We assume that an infinitely thin beam shines the turbid two-layered medium. The first layer of the two-layer medium has a thickness Δ_1, and the second layer is semi-infinite. The beam is scattered isotropically in the upper layer at a depth of $z = z_0$, where $z_0 = 1/(\mu_{a1} + \mu_{s1}^{'})$. We also assume that the Brownian movement is independent in each layer, meaning that the particles can not move from one layer to another in the medium. The incident light is perpendicular to the surface of the turbid medium (on the x-y plane). Then Eq. (3) becomes:

$$\left(-D_1\nabla^2 + \mu_{a1} + \frac{1}{3}k_0^2\mu_{s1}^{'}\left\langle \Delta r_1^2(\tau)\right\rangle\right)G_1^1(x,y,z,\tau) = S(x,y,z-z_0),\ 0 \le z \le \Delta_1, \tag{5}$$

$$\left(-D_2\nabla^2 + \mu_{a2} + \frac{1}{3}k_0^2\mu_{s2}^{'}\left\langle \Delta r_2^2(\tau)\right\rangle\right)G_1^2(x,y,z,\tau) = 0,\ \Delta_1 \le z, \tag{6}$$

where $D_i = 1/3\left(\mu_{a(i)} + \mu_{s(i)}^{'}\right)$ is the diffusion constant of Layer *i*. The mean-squared displacement $\left\langle \Delta r_i^2(\tau)\right\rangle = 6D_{B(i)}\tau$ for Layer *i*.

Although Kienle *et al.*'s derivations (Kienle et al., 1998; Kienle and Glanzmann, 1999; Kienle et al., 1998) are initially for diffuse reflectance spectroscopy (DRS), we re-derive them for DCS following the same procedure and obtain the solution of Eqs. (5) and (6) at z = 0 (Layer 1) in the Fourier domain by

$$\begin{aligned}\widetilde{G}_1^1(\boldsymbol{q},z,\tau) = &\frac{\sinh[\mathfrak{Z}_1(z_b+z_0)]}{D_1\mathfrak{Z}_1} \\ &\times \frac{D_1\mathfrak{Z}_1\cosh[\mathfrak{Z}_1(\Delta_1 - z)] + D_2\mathfrak{Z}_2\sinh[\mathfrak{Z}_1(\Delta_1 - z)]}{D_1\mathfrak{Z}_1\cosh[\mathfrak{Z}_1(\Delta_1 + z_b)] + D_2\mathfrak{Z}_2\sinh[\mathfrak{Z}_1(\Delta_1 + z_b)]} \\ &- \frac{\sinh[\mathfrak{Z}_1(z_0 - z)]}{D_1\mathfrak{Z}_1},\end{aligned} \tag{7}$$

where $\mathfrak{Z}_j^2 = \left(D_j\boldsymbol{q}^2 + \mu_{aj} + 2c\mu_{sj}^{'}k_0^2D_{Bj}\right)/D_j$, j =1 and 2, $\boldsymbol{q}$ is the radial spatial frequency and

$$z_b = \frac{1+R_{eff}}{1-R_{eff}}2D_1. \tag{8}$$

And $G_1^1(\boldsymbol{\rho}, z=0, \tau)$ at $\boldsymbol{r} = \{\rho, z=0\}$ on the medium surface is then obtained from the inverse spatial Fourier transform as,

$$G_1^1(\boldsymbol{\rho}, z=0, \tau) = \frac{1}{2\pi}\int_0^\infty \widetilde{G}_1^1(\boldsymbol{q}, z=0, \tau)\boldsymbol{q}J_0(\boldsymbol{q}\boldsymbol{\rho})d\boldsymbol{q}, \tag{9}$$

where J_0 stands for the zeroth order Bessel function of the first kind computed by the MATLAB function *besselj*.

2.3. CW three-layer model

Also, in the three-layer DCS model (Li et al., 2005; Verdecchia et al., 2016; Zhao et al., 2021; Wang et al., 2024), $G_1(r,z,\tau)$ can be modelled similarly by CDE. A turbid medium consisting of 3 slabs was considered as shown in Fig. 4(c). Each slab has a thickness $\Delta_p = L_p - L_{p-1}$, p =1, 2, 3. To solve $G_1(r,z,\tau)$, Eq. (3) can be revised for the three-layer model as:

$$\left[\nabla^2 - \left(3\mu_a^{(p)}\mu_s^{'(n)} + 6k_0^2\mu_s^{'2}D_B^{(p)}\tau\right)\right]G_1(r,z,\tau) = -s_0\delta(r-r^{'}), \tag{10}$$

where s_0 is a point-like monochromatic light source located at $r^{'} = \{\rho^{'} = 0,\ z^{'}\}$ inside Layer 1; ρ represents the transverse coordinate. The field autocorrelation at the tissue surface, $G_1(r, z = 0, \tau)$, can be obtained by solving Eq. (10) in the Fourier domain with respect to ρ as:

$$\widehat{G}(\boldsymbol{q},z,\tau) = \int d^2\rho G_1(r,\tau)\exp(i\boldsymbol{q}\cdot\rho), \tag{11}$$

where $\boldsymbol{q}$ is the radial spatial frequency. Thus, in the Fourier domain Eq. (10) can be rewritten:

$$\left[\frac{\partial^2}{\partial z^2} - \kappa^2(\boldsymbol{q},\tau)\right]\widehat{G}(\boldsymbol{q},z,\tau) = -s_0\delta(z-z^{'}), \tag{12}$$

where $\kappa_{(p)}^2(\boldsymbol{q},\tau) = 3\mu_a^{(p)}\mu_s^{'(p)} + 6k_0^2\mu_s^{'2}D_B^{(p)}\tau + \boldsymbol{q}^2$.

We divided the top layer into two sublayers: Sub-layer 0 ($0 < z < z^{'}$) identified by $p = 0$, and Sub-layer 1 ($z^{'} < z < L_1$), identified by p hereafter. The solution of Eq. (12) at Layer p (p = 1, 2, 3) can be written as:

$$\widehat{G}_p(\boldsymbol{q},z,\tau) = A_p\exp\left(\kappa_{(p)}z\right) + B_p\exp\left(-\kappa_{(p)}z\right), \tag{13}$$

where A_p and B_p are constant factors for Layer p determined by the boundary conditions:

$$\begin{cases} \widehat{G}_0(\boldsymbol{q},z,\tau) - z_0\dfrac{\partial}{\partial z}\widehat{G}_0(\boldsymbol{q},z,\tau) = 0, z = 0 \\ \widehat{G}_0(\boldsymbol{q},z,\tau) = \widehat{G}_1(\boldsymbol{q},z,\tau), z = z' \\ \dfrac{\partial}{\partial z}\widehat{G}_0(\boldsymbol{q},z,\tau) = \dfrac{\partial}{\partial z}\widehat{G}_1(\boldsymbol{q},z,\tau) + 3\mu_s^{'1}, z = z' \\ \widehat{G}_p(\boldsymbol{q},z,\tau) = \widehat{G}_{p+1}(\boldsymbol{q},z,\tau),\ z = L_p, p = 1,2 \\ D_p\dfrac{\partial}{\partial z}\widehat{G}_p(\boldsymbol{q},z,\tau) = D_{p+1}\dfrac{\partial}{\partial z}\widehat{G}_{p+1}(\boldsymbol{q},z,\tau), z = L_p, p = 1,2 \\ \widehat{G}_3(\boldsymbol{q},z,\tau) + z_3\dfrac{\partial}{\partial z}\widehat{G}_3(\boldsymbol{q},z,\tau) = 0, z = L_3 \end{cases} \tag{14}$$

where $z_0 \sim 1/\mu_s^{'1}$ and $z_3 \sim 1/\mu_s^{'3}$ are the extrapolation lengths taking into account internal reflections at external ($z = 0$ and $z = L_4$) boundaries.

Substituting Eq. (13) into Eq. (14), we can obtain A_p and B_p ($p = 1, 2, 3$). The Fourier transform $\widehat{G}_0(\boldsymbol{q},z,\tau)$ measured at $z = 0$ (the surface of the slab) is then obtained by substituting A_0 and B_0 into Eq. (13) under $\Delta_3 \to \infty$ to obtain:

$$\widehat{G}_0(\boldsymbol{q},z,\tau) = \frac{Num}{Denom}, \tag{15}$$

where *Num* and *Denom* when $p = 3$ and $\Delta_3 \to \infty$ are:

$$\begin{aligned} Num = {} & 3\mu_s^{'1}z_0(\kappa_1 D_1 cosh(\kappa_1(\Delta_1 - z')))(\kappa_2 D_2 \cosh(\kappa_2\Delta_2) + \kappa_3 D_3 \sinh(\kappa_2\Delta_2)) \\ & + \kappa_2 D_2(\kappa_3 D_3 \cosh(\kappa_2\Delta_2) + \kappa_2 D_2 \sinh(\kappa_2\Delta_2))\sinh(\kappa_1(\Delta_1 - z'))), \end{aligned} \tag{16}$$

$$\begin{aligned} Denom = {} & \kappa_2 D_2 \cosh(\kappa_2 D_2)\left(\kappa_1(D_1 + \kappa_3 D_3 z_0)\cosh(\kappa_1 D_1)\right. \\ & + \left(\kappa_3 D_3 + \kappa_1^2 D_1 z_0\right)\sinh(\kappa_1 D_1)) + \left(\kappa_1\left(\kappa_3 D_1 D_3 + \kappa_2^2 D_2^2 z_0\right)\cosh(\kappa_1 D_1)\right. \\ & + \left(\kappa_2^2 D_2^2 + \kappa_1^2 \kappa_3 D_1 D_3 z_0\right)\sinh(\kappa_1 D_1))\sinh(\kappa_2\Delta_2). \end{aligned} \tag{17}$$

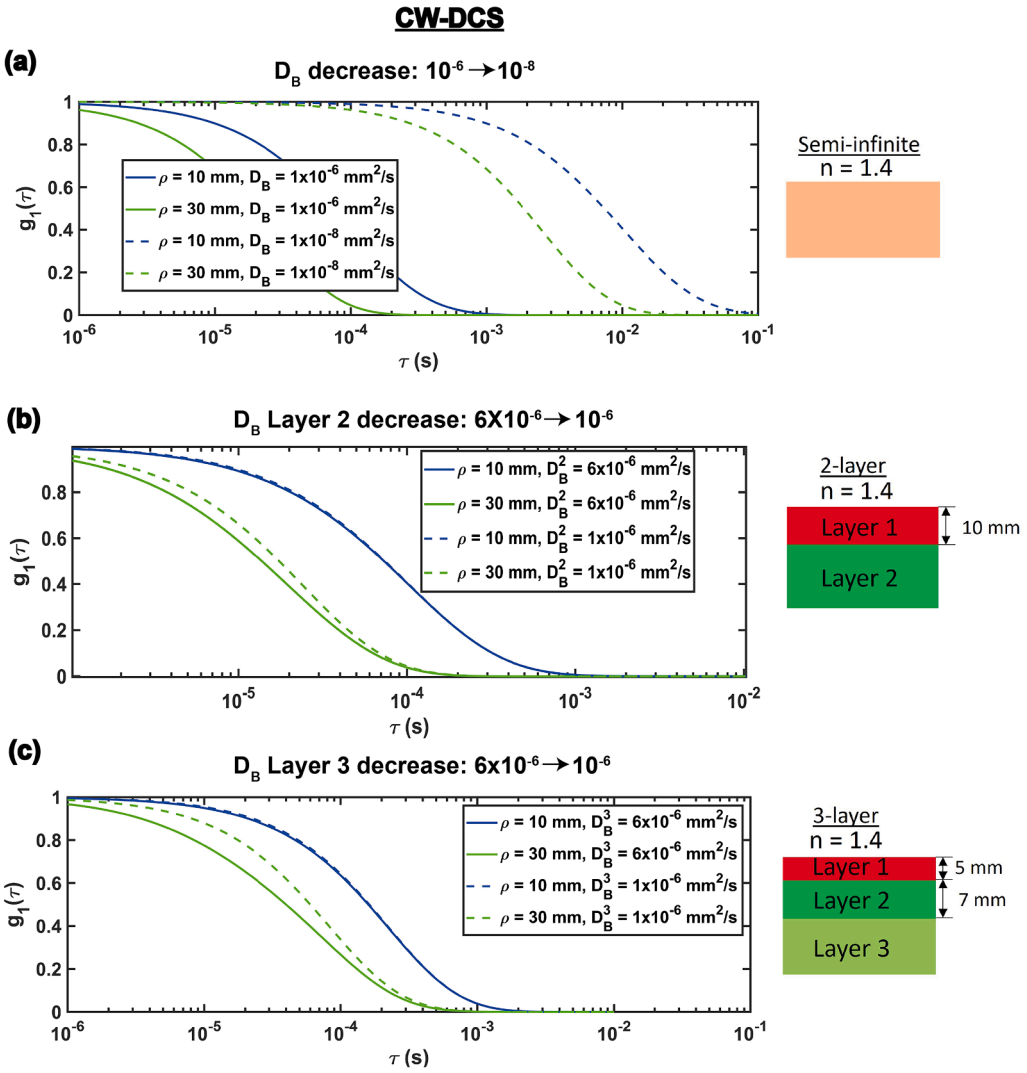

Fig. 5. (a) Representative $g_1(\tau)$ simulated from a sample with $\rho = 10\ mm$ (blue solid line) and $= 30\ mm$ (green solid line), varying D_B from $1 \times 10^{-6} mm^2/s$ to $1 \times 10^{-8} mm^2/s$ (blue and green dot lines), $\mu_a = 0.013 mm^{-1}$, $\mu_s' = 0.86 mm^{-1}$, $\lambda = 785 nm$. (b) Representative $g_1(\tau)$ simulated from a sample with $\rho = 10\ mm$ (blue solid line) and $= 30\ mm$ (green solid line), characterized with $\mu_a^{(1)} = 0.013 mm^{-1}$, $\mu_s^{'(1)} = 0.86 mm^{-1}$, $\Delta_1 = 10 mm$, $D_B^{(1)} = 1 \times 10^{-6} mm^2/s$, (Parameters for the top layer); $\mu_a^{(2)} = 0.018 mm^{-1}$, $\mu_s^{'(2)} = 1.11 mm^{-1}$, varying $D_B^{(2)}$ from $1 \times 10^{-6} mm^2/s$ to $1 \times 10^{-8} mm^2/s$ (Parameters for the bottom layer; blue and green dot lines); (c) Representative $g_1(\tau)$ simulated from a sample with $\rho = 10\ mm$ (blue solid line) and $= 30\ mm$ (green solid line) characterized with $\mu_a^{(1)} = 0.013 mm^{-1}$, $\mu_s^{'(1)} = 0.86 mm^{-1}$, $D_B^{(1)} = 1 \times 10^{-8} mm^2/s$, $\Delta_1 = 5 mm$ (Parameters for the first layer); $\mu_a^{(2)} = 0.018 mm^{-1}$, $\mu_s^{'(2)} = 1.11 mm^{-1}$, $D_B^{(2)} = 1 \times 10^{-6} mm^2/s$, $\Delta_2 = 7 mm$ (Parameters for the second layer); $\mu_a^{(3)} = 0.03 mm^{-1}$, $\mu_s^{'(3)} = 1.19 mm^{-1}$, varying $D_B^{(3)}$ from $1 \times 10^{-6} mm^2/s$ to $1 \times 10^{-8} mm^2/s$ (Parameters for the third layer), the spatial frequency $\boldsymbol{q} \in (0,\ 30] mm^{-1}$. All graphs are plotted using homemade software using MATLAB (Mathworks, Inc.).

By performing the inverse Fourier transform of Eq. (15) with respect to $\boldsymbol{q}$, $\widehat{G}_0(\boldsymbol{q},z,\tau)$ can be obtained as:

$$G_0(r,\tau)=\frac{1}{(2\pi)^2}\int d^2\boldsymbol{q}\widehat{G}_0(\boldsymbol{q},z=0,\tau)\exp(-i\boldsymbol{q}\cdot\boldsymbol{\rho})$$
$$=\frac{1}{2\pi}\int d\boldsymbol{q}\widehat{G}_0(\boldsymbol{q},z=0,\tau)qJ_0(\rho\boldsymbol{q}), \tag{18}$$

where J_0 denotes the first-kind zero-order Bessel function.

This three-layered solution has been tested with Monte Carlo simulations and used to analyze *in vivo* measurements (Verdecchia et al., 2016; Zhao et al., 2021; Zhao et al., 2023). The three-layer model can be used in monitoring cerebral blood flow in adults, particularly in clinical settings such as during surgery or in intensive care units because it is necessary to account for scalp, skull, and brain tissues, which can significantly affect light propagation and DCS signals.

Fig. 5(a), (b), and (c) show g_1 curves for semi-infinite, two-, and three-layer analytical models, respectively. Typically, in DCS data analysis, the measured g_2 is fitted with one of the models shown in Fig. 4, using the Siegert relation $g_2(\tau)=1+\beta g_1^2(\tau)$. Usually, the homogenous semi-infinite analytical model is used in data analysis, assuming free diffusion for speckle decorrelation, giving rather poor agreement with experimental scenarios. This is because homogeneous fitting is more sensitive to the dynamic properties of the superficial layers. Compared with the semi-infinite model, two- and three-layered models can separate the signal between the superficial and brain layers. The layered models can mitigate the discrepancies between the one-layer model and realistic tissues. The accuracy of the three-layer analytical model has been investigated in previous studies (Mesquita et al., 2011; Li et al., 2005; Zhao et al., 2021). Although multi-layered models provide a superior fit to measured data and are more accurate, they are susceptible to measurement noise, and much longer BFi estimation time is needed (Wang et al., 2024).

2.4. TD semi-infinite (one layer) model

For TD-DCS systems, $G_1(\vec{\boldsymbol{r}},\tau,t)$ obeys the time-dependent correlation equation:

$$\left(-\frac{D(\boldsymbol{r})}{v}\nabla^2+\mu_a+\frac{1}{3}\alpha\mu_s'k_0^2\langle\Delta r^2(\tau)\rangle+\frac{1}{v}\frac{\partial}{\partial_t}\right)G_1(\boldsymbol{r},t,\tau)=S(\boldsymbol{r},t). \tag{19}$$

For a semi-infinite medium, it is straightforward to obtain the analytical solution of Eq. (19) under the boundary condition (Farrell et al., 1992). Thus $G_1(\rho,t,\tau)$ on the tissue surface ($z=0$) is (Sutin et al., 2016):

$$G_1(\rho,t,\tau)=c\left(\frac{3\mu_s'}{4\pi ct}\right)^{\frac{3}{2}}\exp\left[-(\mu_a+2\mu_s'\,D_Bk_0^2\tau)ct\right]\exp\left(-\frac{3\mu_s'\rho^2}{4ct}\right)$$
$$\times\left[\exp\left(-\frac{3\mu_s'\,z_0^2}{4ct}\right)-\exp\left(-\frac{3\mu_s'(z_0+2z_b)^2}{4ct}\right)\right]. \tag{20}$$

Thus, $g_1(\tau,s)$ for a photon pathlength s can be written as:

$$g_1^{single}(\tau,s)=\frac{G_1(\rho,t,\tau)}{G_1(\rho,t,\tau=0)}$$
$$=\exp\left(-2\mu_s'D_Bk_0^2s\tau\right). \tag{21}$$

However, it is not easy to measure the pathlength of a photon in tissues. Therefore, the total scattered electric-field autocorrelation function $g_1(\tau,s)$ is obtained by incoherently summing the contributions over all s (Maret and Wolf, 1987; Yodh et al., 1990). Thus $g_1(\tau,s)$ is a weighted average over all possible pathlengths as:

$$g_1(\tau)=\int_0^\infty P(s)g_1^{single}(\tau,s)ds$$
$$=\int_0^\infty P(s)\exp\left(-2\mu_s'D_Bk_0^2s\tau\right)ds. \tag{22}$$

where $P(s)$ represents the probability that an incident photon travels a distance s before emerging from the medium; it can be calculated as (Kienle and Patterson, 1997):

$$P(s)=\frac{v}{(4\pi Ds/v)^{3/2}}\exp(-\mu_s s)\times\left[\exp\left(-\frac{r_1^2}{4Ds}\right)-\exp\left(-\frac{r_2^2}{4Ds}\right)\right], \tag{23}$$

where the variables are the same as in Eq. (4) and $s=vt$, with t being the photon time-of-flight (ToF) and v the speed of light in the medium.

By employing a sufficiently narrow time gate, Eq. (22) can be simplified, and the normalized time-gated $g_1(\tau)$ is modelled by a single exponential term:

$$g_1(\tau)=\exp\left(-2\mu_s'\,k_0^2vtD_B\right), \tag{24}$$

Then $g_2(\tau)$ can be linked to $g_1(\tau)$through the Siegert relation:

$$g_2(\tau)=1+\beta|g_1(\tau)|^2. \tag{25}$$

2.5. TD two-layer model

For the second layer model, Eq. (19) can be rewritten:

$$\left[\nabla^2-\left(3\mu_a^{(p)}\mu_s'^{(p)}+6k_0^2\mu_s'^2D_B^{(p)}\tau\right)-\frac{3\mu_s'}{v}\frac{\partial}{\partial t}\right]G(\boldsymbol{r},\tau,t)=-3\mu_s'\delta(\boldsymbol{r}-\boldsymbol{r}'). \tag{26}$$

Similarly, we can derive the Fourier transform of $G(\boldsymbol{r},\tau,t)$ for the real space (ρ,z), as well as time t, and then solve Eq. (26) in the Fourier space $(\boldsymbol{q},z,w)$.

$$\widehat{G}(\boldsymbol{q},z,w,\tau)=\int dt\exp(iwt)\int d^2\rho G(\rho,z,t,\tau)\exp(i\boldsymbol{q}\cdot\rho), \tag{27}$$

yielding

$$\left[\frac{\partial^2}{\partial z^2}-\left(3\mu_a^{(p)}\mu_s'^{(p)}+6k_0^2\mu_s'^2D_B^{(p)}\tau-3\mu_s'^{(p)}\cdot\frac{iw}{c}\right)-\boldsymbol{q}^2\right]\widehat{G}(\boldsymbol{q},z,w,\tau)=-3\mu_s'\delta(z-z'). \tag{28}$$

The solution of Eq. (28) can be written as:

$$\widehat{G}(q,z,w,\tau)=\gamma_p\exp(\Psi_pz)+\varphi_p\exp(-\Psi_pz), \tag{29}$$

where $\Psi_p=\sqrt{\left(3\mu_a^{(p)}\mu_s'^{(p)}+6k_0^2\mu_s'^2D_B^{(p)}\tau-3\mu_s'^{(p)}\cdot\frac{iw}{c}\right)+\boldsymbol{q}^2}$, γ_p and φ_p are constant for Layer p ($p=1,\ 2$), determined by the boundary conditions:

$$\begin{cases}\widehat{G}_0(\boldsymbol{q},z,w,\tau)-z_0\dfrac{\partial}{\partial z}\widehat{G}_0(\boldsymbol{q},z,w,\tau)=0,\ z=0\\ \widehat{G}_0(\boldsymbol{q},z,w,\tau)=\widehat{G}_1(\boldsymbol{q},z,w,\tau),\ z=z'\\ \dfrac{\partial}{\partial z}\widehat{G}_0(\boldsymbol{q},z,w,\tau)=\dfrac{\partial}{\partial z}\widehat{G}_1(\boldsymbol{q},z,w,\tau)+3\mu_s'^1,\ z=z'\\ \widehat{G}_p(\boldsymbol{q},z,w,\tau)=\widehat{G}_{p+1}(\boldsymbol{q},z,w,\tau),\ z=L_p,p=1,2\\ D_p\dfrac{\partial}{\partial z}\widehat{G}_p(\boldsymbol{q},z,w,\tau)=D_{p+1}\dfrac{\partial}{\partial z}\widehat{G}_{p+1}(\boldsymbol{q},z,w,\tau),z=L_p,p=1,2\\ \widehat{G}_3(\boldsymbol{q},z,w,\tau)+z_3\dfrac{\partial}{\partial z}\widehat{G}_3(\boldsymbol{q},z,w,\tau)=0,z=L_3\end{cases} \tag{30}$$

Thus, we can obtain the solution of Eq. (28):

$$\widehat{G}_0(\boldsymbol{q}, z=0, w, \tau) = \frac{3\mu_s^{'} z_0[\Psi_1 D_1 \cosh(\Psi_1(\Delta_1 - z_0)) + \Psi_2 D_2 \sin(\Psi_1(\Delta_1 - z_0))]}{\Psi_1(D_1 + \Psi_2 D_2 z_0)\cosh(\Psi_1\Delta_1) + (\Psi_2 D_2 + {\Psi_1}^2 D_1 z_0)\sinh(\Psi_1\Delta_1)}. \tag{31}$$

The inverse Fourier transform for $G(\rho, z, t, \tau)$ at $z = 0$ is:

$$G_0(\rho, z=0, t, \tau) = \frac{1}{2\pi}\int dw \exp(-iwt)\frac{1}{(2\pi)^2}\int d^2q \widehat{G}_0(\boldsymbol{q}, z=0, w, \tau)\exp(-i\boldsymbol{q}\cdot\rho) = \frac{1}{(2\pi)^2}\int dw \int dq \widehat{G}_0(\boldsymbol{q}, z=0, w, \tau)\boldsymbol{q}J_0(\rho\boldsymbol{q})\exp(-iwt). \tag{32}$$

$$\begin{aligned} Num = {} & 3\mu_s^{'} z_0[\Psi_1 D_1 \cosh(\Psi_1(\Delta_1 - z^{'}))(\Psi_2 D_2 \cosh(\Psi_2 D_2) + \Psi_3 D_3 \sinh(\Psi_2 D_2)) \\ & + \Psi_2 D_2(\Psi_3 D_3 \cosh(\Psi_2 D_2) + \Psi_2 D_2 \sinh(\Psi_2 D_2))\sinh(\Psi_1(\Delta_1 - z^{'})). \end{aligned} \tag{33}$$

$$\begin{aligned} Demo = {} & \Psi_2 D_2 \cosh(\Psi_2\Delta_2)\left[\Psi_1(D_1 + \Psi_3 D_3 z_0)\cosh(\Psi_1\Delta_1) + \right. \\ & \left.(\Psi_3 D_3 + {\Psi_1}^2 D_1 z_0)\sinh(\Psi_1\Delta_1)\right] + \left[\Psi_1(\Psi_3 D_1 D_3 + {\Psi_2}^2 {D_2}^2 z_0)\cosh\right. \\ & \left.(\Psi_1\Delta_1) + ({\Psi_2}^2 {D_2}^2 + {\Psi_1}^2 \Psi_3 D_1 D_3 z_0)\sinh(\Psi_1\Delta_1)\right]\sinh(\Psi_2\Delta_2). \end{aligned} \tag{34}$$

2.6. TD three-layer model

We start from Eq. (26), but derive similarly with Section 2.3 and $\Delta_3 \to \infty$, to obtain derive $G(\rho, z, t, \tau)$ for the three-layer model as the same with Eq. (32), where $\widehat{G}_0(q, z=0, w, \tau) = \frac{Num}{Demo}$, where *Num* and *Demo* are shown below respectively,

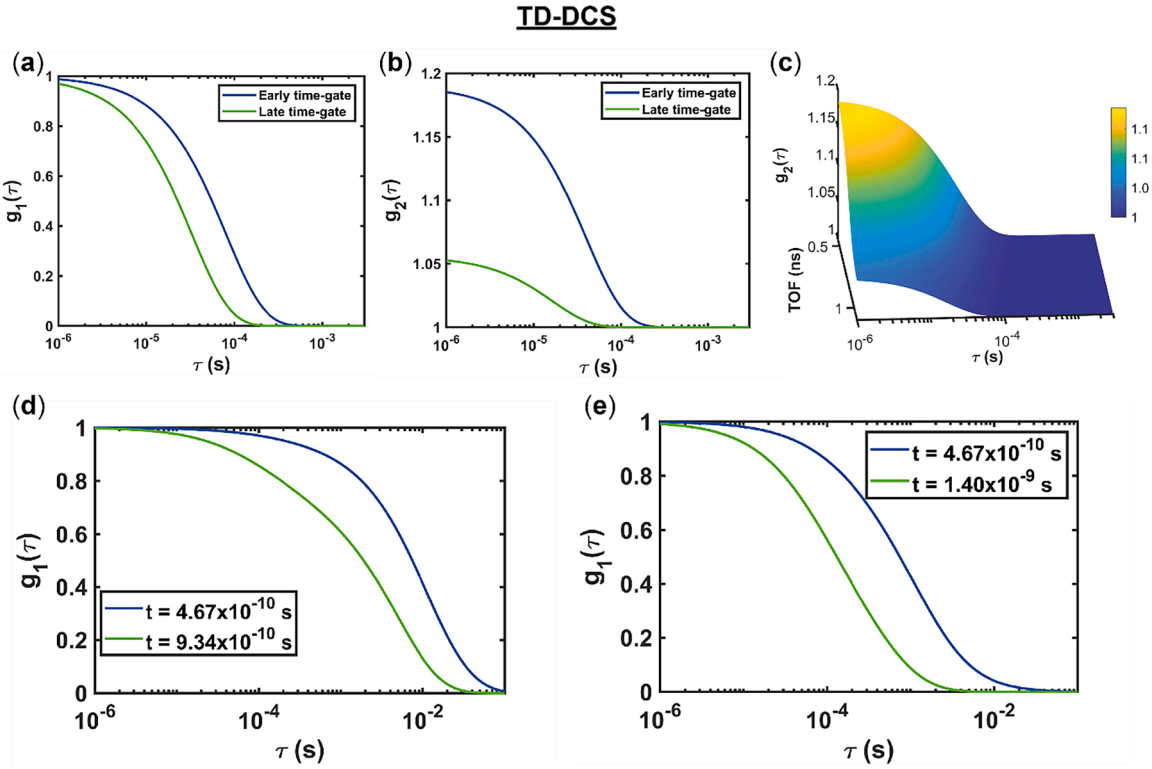

Fig. 6. (a) Simulated $g_1(\tau)$ with Eq. (24) $g_2(\tau)$ with (25), with $\rho = 10\ mm$, $D_B = 1.09 \times 10^{-8} mm^2/s$, $\mu_a = 0.013 mm^{-1}$, $\mu_s^{'} = 0.86 mm^{-1}$, $\lambda = 785 nm$, $s = 135\ mm$ (ToF = 450 ps, data provided by Samaei (Samaei et al., 2021)); (b) Simulated $g_1(\tau)$ from Eqs. (31) and (32) with $\mu_a^{(1)} = 0.013 mm^{-1}$, $\mu_s^{'(1)} = 0.86 mm^{-1}$, $\Delta_1 = 10 mm$, $D_B^{(1)} = 1 \times 10^{-6} mm^2/s$, $\mu_a^{(2)} = 0.018 mm^{-1}$, $\mu_s^{'(2)} = 1.11 mm^{-1}$, $D_B^{(2)} = 1 \times 10^{-6} mm^2/s$, $q \in (0,\ 30]$, $w \in (0\ 20]$Hz and $t = 4.67 \times 10^{-10} s$ and $t = 9.34 \times 10^{-10} s$. We adopted these parameters from Ref. Li et al. (2017) (c) $g_1(\tau)$ with $\mu_a^{(1)} = 0.013 mm^{-1}$, $\mu_s^{'(1)} = 0.86 mm^{-1}$, $D_B^{(1)} = 1 \times 10^{-6} mm^2/s$, $\Delta_1 = 2 mm$, $\mu_a^{(2)} = 0.018 mm^{-1}$, $\mu_s^{'(2)} = 1.11 mm^{-1}$, $D_B^{(2)} = 1 \times 10^{-7} mm^2/s$, $\Delta_2 = 5 mm$, $\mu_a^{(3)} = 0.03 mm^{-1}$, $\mu_s^{'(3)} = 1.19 mm^{-1}$, $D_B^{(3)} = 1 \times 10^{-6} mm^2/s$, $q \in (0,\ 30] mm^{-1}$, $w \in (0\ 20]$Hz, and $t = 4.67 \times 10^{-10} s$ and $t = 1.40 \times 10^{-9} s$. The settings are the same with Ref. Li et al. (2017).

$G_0(q, z=0, t, \tau)$ measured on the top of the surface ($z = 0$) of the slab is the inverse Fourier transform of $\widehat{G}_0(q, z=0, w, \tau)$,

$$G_0(\boldsymbol{q}, z=0, t, \tau) = \frac{1}{(2\pi)^2}\int dw \int d\boldsymbol{q}\widehat{G}_0(\boldsymbol{q}, z=0, w, \tau)\boldsymbol{q}J_0(\rho\boldsymbol{q})\exp(-iwt). \tag{35}$$

Fig. 6 displays the numerical simulation g_1 for time-domain DCS from the semi-infinite, two-, and three-layer analytical models. Fig. 6(a) is $g_1(\tau)$ for the early gate and late gate; Fig. 6(b) is corresponding $g_2(\tau)$ for the early gate and late gate and Fig. 6(c) is the $g_2(\tau)$ at different gate and lag time. Fig. 6(d) is performed for $\rho = 10$ mm, two pathlengths are selected, t = 4.67×10^{-10} s and t = 9.34×10^{-10} s. Similarly, Fig. 6(e) is performed for $\rho = 10$ mm, two pathlengths are selected, t = 4.67×10^{-10} s and t = 1.40×10^{-9} s.

2.7. Frequency domain semi-infinite model

We also obtain $G_1(\rho, \omega, \tau)$ when modulated illumination is used, $G_1(\rho, \omega, \tau)$ follows a slightly different CDE as:

$$\left[\nabla^2 - 3\mu_s'\left(\mu_a + 2\mu_s' k_0^2 D_B\tau - \frac{i\omega}{v}\right)\right]G_1(\rho, \omega, \tau) = -3\mu_s' s_0 e^{-i\omega t}, \tag{36}$$

where ω is the source modulation frequency and $s_0 e^{-i\omega t}$ is the modulated source term. For a semi-infinite homogeneous tissue, the solution of Eq. (36) is given by

$$G_1(\rho, \omega, \tau) = \frac{3\mu_s'}{4\pi}\left[\frac{\exp(-K_D(\omega,\tau)r_1)}{r_1} - \frac{\exp(-K_D(\omega,\tau)r_2)}{r_2}\right], \tag{37}$$

where $K_D(\omega, \tau) = \sqrt{3\mu_s'\left(\mu_a + 2\mu_s' k_0^2 D_B\tau - i\omega/v\right)}$ is the frequency-dependent wave vector. The other parameters are the same as before. Fig. 7 shows $g_1(\tau)$ for the FD semi-infinite model. By fitting the measurement data from FD-DCS systems to Fig. 7, we can extract optical properties (μ_a and μ_s') and blood flow simultaneously by multi-frequency measurements. In contrast, the traditional CW-DCS system is only used for blood flow measurements. Another merit is that the laser source for FD-DCS is much cheaper than CW-DCS and TD-DCS systems. There are two reasons: 1) FD-DCS removes the necessity for collocating the source and phase-sensitive detectors; 2) FD-DCS can be executed by simply substituting the source of a traditional DCS system with an intensity-modulated coherent laser.

Although the two- and three-layer theoretical DCS models shown in Fig. 4 have improved the SNR, those with regular tissue boundaries (including the simi-infinite model) may lead to BFi estimation errors in small-volume tissues with large curvatures. To address this, Shang *et al.* developed an *Nth*-order linear model that can accurately extract BFi without tissue volume and geometry restrictions. They demonstrated the algorithm's accuracy with computational simulations and *in vivo* experiments. Interested readers can consult the referenced studies (Shang et al., 2014; Shang and Yu, 2014; Zilpelwar et al., 2022) for more details.

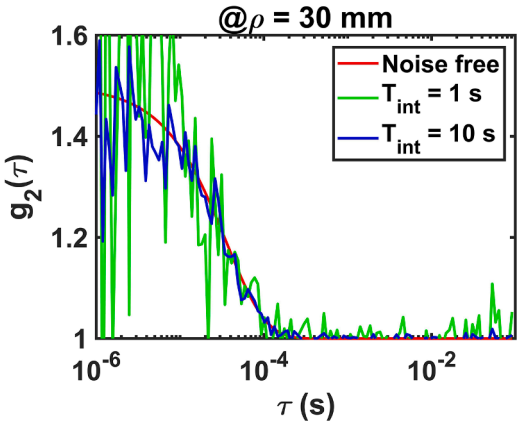

Fig. 8. Simulated $g_2(\tau)$ curves with $\rho = 30mm$ on a homogeneous sample with $\mu_a = 0.01mm^{-1}$, $\mu_s' = 1.2mm^{-1}$, $\lambda = 785\,nm$, $\beta = 0.5$, and $D_B = 2 \times 10^{-9}mm^2/s$. The curves include a noise-free scenario (red solid line) and with realistic noise added using Eq. (38), assuming an 8.05 kcps at 785 nm (Carp et al., 2010), at different noise levels with $T_{int} = 1\ s$ (green line) and $T_{int} = 10\ s$ (blue line).

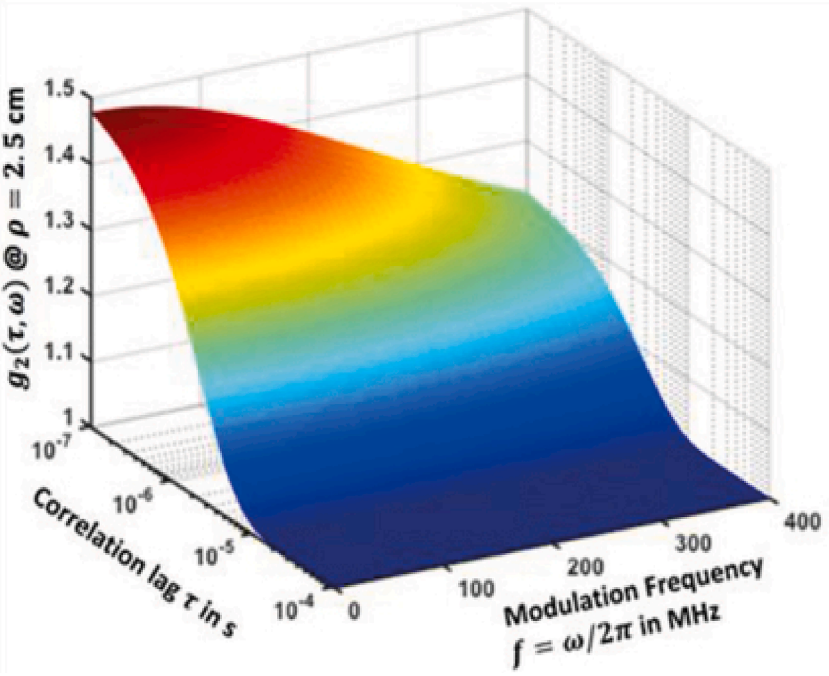

Fig. 7. Numerical simulated FD $g_1(\rho, \omega, \tau)$ at $\rho = 25mm$ with various modulation frequency. Image adopted from Ref. Moka et al. (2022).

2.8. Noise model

In most simulation reports (Dong et al., 2013; Carp et al., 2020; Mazumder et al., 2021; Irwin et al., 2011), a proper estimate of measurement noise is needed to reflect practical scenarios. A noise model suitable for photon correlation measurements was previously developed for a single scattering limit (Schätzel, 1983; Koppel, 1974). Later on, the noise model developed by Koppel (Koppel, 1974) for fluorescence correlation spectroscopy (FCS) in the single scattering limit was introduced into DCS in 2006 (Zhou et al., 2006). In DCS, the noise comes from photon counting statistics (Schätzel, 1983), and it has been derived (Zhou et al., 2006) with the standard deviation of $(g_2(\tau) - 1)$, $\sigma(\tau)$ estimated as:

$$\sigma(\tau) = \sqrt{\frac{T}{T_{int}}}\left[\beta^2\frac{\left(1+e^{-T/\tau_c}\right)\left(1+e^{-\tau/\tau_c}\right)+2m\left(1-e^{-T/\tau_c}\right)e^{-\tau/\tau_c}}{1-e^{-T/\tau_c}} + \langle M\rangle^{-2}\left(1+\beta e^{-\tau 2\tau_c}\right)+2\langle M\rangle^{-1}\beta\left(1+\ e^{-\tau/\tau_c}\right)\right]^{1/2}, \tag{38}$$

where T is the frame exposure time (equal to the correlator bin time interval). T_{int} is the integration time (measurement duration) or the measurement time window. τ_c is the speckle correlation time. $\langle M\rangle$ ($\langle M\rangle = IT$, where I is the detected photon count rate) is the average number of photons within bin time T, m is the bin index. To obtain τ_c, $g_2(\tau)$ usually approximated with a single exponential function as $g_2(\tau) \approx 1 + \beta\exp(-\tau/\tau_c)$ under the Brownian motion model (Zhou et al., 2006). Once τ_c is obtained, we can obtain $\sigma(\tau)$. This noise model was then adopted by (Sie et al., 2020; Cheng et al., 2021; Helton et al., 2023; Zhang et al., 2018).

Fig. 8 shows noise (orange line) and noiseless (blue line) $g_2(\tau)$. The noise model predicted standard deviations for $g_2(\tau)$ at each τ was applied by randomly sampling a normal distribution, where the $T_{int} = 1s$ and 10 s and the delay time $1 \times 10^{-6}\ s \le \tau \le 1 \times 10^{-1} s$ (128 data points) was used. Considering realistic photon budgets, the photon count rate at 785 nm was assumed to be 8.05 kcps (Carp et al., 2020) at ρ of 30 mm. In Fig. 8, the DCS measurement noise decreases as τ increases.

3. Instrumentation

A DCS system consists of a laser source, source/detection fibers and sensors. Fig. 9 shows a schematic of the representative systems for CW-, TD-, FD-, and Hybrid DCS systems. Fig. 9(a) and (b) are for CW- and TD-DCS systems, respectively. The primary difference lies in the pulsed laser (Ti:Sa laser) in the TD system. Fig. 9(c) showcases the schematic of FD-DCS system, representing the latest DCS technology in the frequency domain. Lastly, Fig. 9(d) presents a typical hybrid DCS system. To date, very few companies have initiated commercialization of DCS systems, including HemoPhotonics S.L. (http://www.hemophotonics.com), and ISS Inc. (https://iss.com/biomedical/metaox).

3.1. Lasers

There are three types of laser used in DCS: CW, modulated, and pulsed lasers corresponding to CW-, FD-Moka et al., 2022), and TD-DCS systems. As was mentioned above, the estimated BFi is derived from intensity fluctuations of the speckle pattern of back scattered light from the tissue surface, and the bright and dark patterns arise because photons emerging from the sample have travelled along different paths that interfere constructively and destructively at different detector positions (Durduran and Yodh, 2014; Durduran et al., 2010; Maret and Wolf, 1987). Consequently, one of the main challenges is to select a laser with

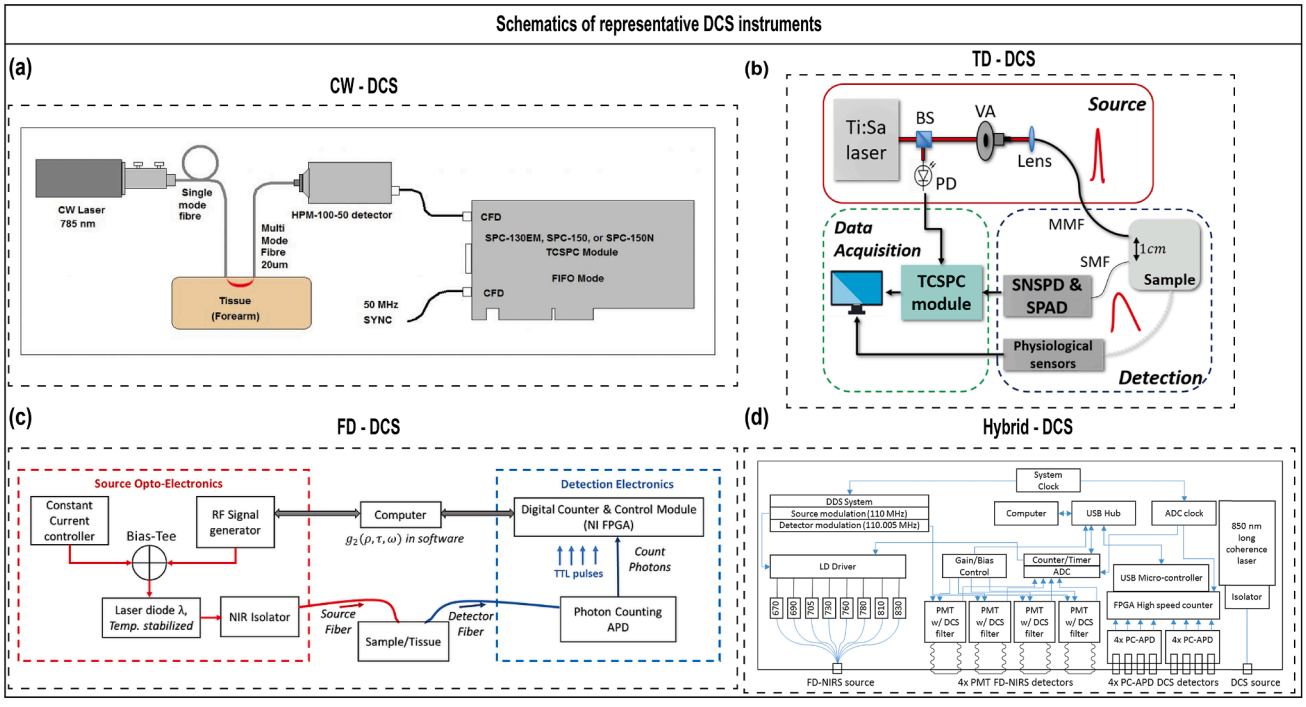

Fig. 9. (a) A typical CW-DCS system, adopted from https://www.becker-hickl.com/applications/dcs-diffuse-correlation/, (b) Parfentyeva *et al.*'s TD-DCS system (Parfentyeva et al., 2023), (d) Sadhu *et al.*'s FD-DCS system (Moka et al., 2022), (d) Carp *et al.*'s hybrid DCS system (Carp et al., 2017).

a long coherence length (Maret and Wolf, 1987), l_c, designated by Eq. (39) assuming that the measured power spectral density has a Gaussian profile (Bigio and Fantini, 2016),

$$l_c = \frac{\lambda^2}{\Delta\lambda} \tag{39}$$

where λ is the central wavelength and $\Delta\lambda$ is the optical bandwidth. The diffusion theory and Monte Carlo simulations of light transport show that the minimum coherence length must be longer than the width of the photon path-length distribution (Bellini et al., 1991), typically around $5\rho \sim 10\rho$ (e.g., 100 mm for $\rho = 10mm$) (Biswas et al., 2021). For homodyne measurements, the coherence length needs to be substantially longer than the spread of pathlengths in tissue (which is within an order of ρ), and in heterodyne, care needs to be taken that the difference in length of the reference vs. sample arms, when summed with the expected pathlength variation, should also be substantially lower than the laser coherence length. Therefore, generally, the minimum coherence length is recommended as $l_{c,\ min} \gg 10\rho \sim 15\rho$, and since most practical DCS systems utilize $\rho \sim 3$ cm (Durduran and Yodh, 2014; Carp et al., 2020; Kim et al., 2010), the coherence length should be $35 \sim 50\ cm$, accounting for the variations of differential pathlength distances (Delpy et al., 1988).

For clinical applications, the laser power should comply with the American National Standard for Safe Use of Lasers (ANSI) (Institute, 2007) limit for safe skin exposure with an proper irradiance. Spacers or prisms (Biswas et al., 2021; Zavriyev et al., 2021; Wu et al., 2023; Lee et al., 2019) are often between source fiber and sample to illuminate a larger area, which allows a higher laser power (more photons) while maintaining the same maximal permissible exposure (MPE) limit for intensity. Typically, lasers with wavelengths of 670 nm (Liu et al., 2021), 760nm (Samaei et al., 2021), 785 nm (Biswas et al., 2021; Huang et al., 2016), 850 nm (James and Munro, 2023; Zauner et al., 2002; Maret and Wolf, 1987; Carp et al., 2017), or 1064 nm(Carp et al., 2020) are employed. Although NIR wavelengths provide a higher number of photons for the same output power ($P = E/t = h\ c\ /\ \lambda$, E is photon energy), a higher MPE (more photons) and a deeper penetration depth, the photon detection efficiency (PDE) of most detectors is typically reduced for longer wavelengths. As a result, 785 nm and, more recently, 850 nm lasers are the most prevalent choice for most DCS techniques. This trade-off between the laser and the detector PDE is discussed in detail below.

Regarding TD-DCS, we can pinpoint the photons (either through gating or time-correlated single-photon counting (Wahl and GmbH, 2009)) that exhibit a similar path length in the tissue to provide depth-resolved information. This allows relaxing the requirement for a high coherence length compared with the scenario in which all the photon paths are considered. Moreover, the laser pulse width limits the maximum coherence length for a pulsed laser. Usually, a narrow laser pulse is preferable for precise depth-resolved measurements, however, a narrow pulse means a lower l_c, meaning a g_2 curve is closer to the noise floor. Therefore, there is a trade-off between l_c and the pulse width (Tamborini et al., 2019). In fact, $g_2's$ maximum amplitude depends on l_c, with β ranging from 0 for incoherence light to 1 for linearly polarized light (Ferreira et al., 2020) (0.5 for unpolarized light) with l_c longer than the longest photon path. Therefore, the main limitation of the broad use of TD-DCS is the availability of an ideal pulsed laser considering power settings, pulse width, coherence, stability, and robustness. To obtain a more in-depth investigation, readers can check Refs. Samaei et al. (2021), Tamborini et al. (2019), Ozana et al. (2022). In Table 1, we extend the conclusions made by Samaei et al. (2021), Ozana et al. (2022) and Tamborini et al. (2019) to show the relevant parameters of pulse lasers.

3.2. Source and detection fibers

In DCS experiments, a pair of source and detection fibers are strategically placed on the tissue surface, with a separation of ρ (ranging from millimeters to centimeters). The laser emits long-coherence light through the source fiber into tissues, and the fiber collects the scattered light to a sensor. This distance ρ then defines the extent of the scattering paths of all detected photons, and thereby, the maximal measurement depth of DCS, as illustrated above in Fig. 2(d). The diagrams in Fig. 10 (a)–(c) illustrate three fibers with distinct modes, namely single-mode, few-mode, and multi-mode. Usually, a multi-mode fiber (core diameter D = 62.5, 200, 400, 600, 1000 μm) (Dong et al., 2012; Ozana et al., 2022; Shang et al., 2011; Lin et al., 2012) is used for the source side. Here, it should be noted that a larger diameter fiber translates to a larger illumination area allowing a higher laser power (more photons) at the same MPE limit for intensity (see Section 3.1). For the detection, previously published DCS systems used single-mode (e.g., 5 μm) (Gurley et al., 2012; Zhou et al., 2007; Dong et al., 2012; Shang et al., 2011; Cheng et al., 2012; Han et al., 2015; Stapels et al., 2016; Farzam et al., 2017; Sathialingam et al., 2018; Poon et al., 2020, Cortese et al., 2021; Cowdrick et al., 2023; Nakabayashi et al., 2023), few-mode (Li et al., 2005), or multi-mode fibers (Sie et al., 2020; Liu et al., 2021; Wayne et al., 2023; Samaei et al., 2022). Single-mode fibers are usually directly coupled to the respective detector. For parallelized DCS with SPAD arrays, multi-mode fibers are used for detection. In that case, the fiber is placed at a distance z to the detector, to match the speckle diameter (d) to the diameter of the detector's active area, according to Ref. Freund (2007)

$$d = \frac{\lambda\ z}{D} \tag{40}$$

where D is the core diameter of the detection fiber. Thus, adjusting the distance between fiber and detector (z) allows controlling the speckle size on the detector and therefore the number of measured speckles per pixel. Using single-mode fibers limits the measured light intensity because only the fundamental mode of light can be transported, limiting ρ's dynamic range. Unlike conventional fibers, few-mode fibers allow not only the fundamental mode but also a few higher-order modes of light. Expanding the fiber diameter and numerical aperture (NA) in few-mode fibers to encompass multiple speckles enhances the detected signal intensity, consequently enhancing the signal-to-noise ratio (SNR). However, the multiple speckles detected by the few-mode fibers exhibit uncorrelated behaviour, and the decrease in β effectively counteracts the SNR enhancement. Finally, this flattens the autocorrelation function curve, potentially diminishing the sensitivity of DCS flow measurements

Table 1
Parameters of laser source used in TD-DCS, adopted from Samaei et al. (2021), Ozana et al. (2022) and Tamborini et al. (2019).

Laser	Central wavelength (nm)	Temporal Coherence length (mm)	Spectrum bandwidth [nm]	Pulse width (ps)	Average output power (mw)
VIRIS-500	767	38	N.A	550	50
LDH-P-C-N-760 (Samaei et al., 2021)	760.4	6.1	0.095	106	12
Ti: Sapphire (Samaei et al., 2021)	763.8	6.3	0.093	185	50
VisIR-765-HP "STED" (Tamborini et al., 2019)	765.7	38	N.A	535	<1500
PicoQuant GmbH (Ozana et al., 2022)	1064	60	N.A	600	100

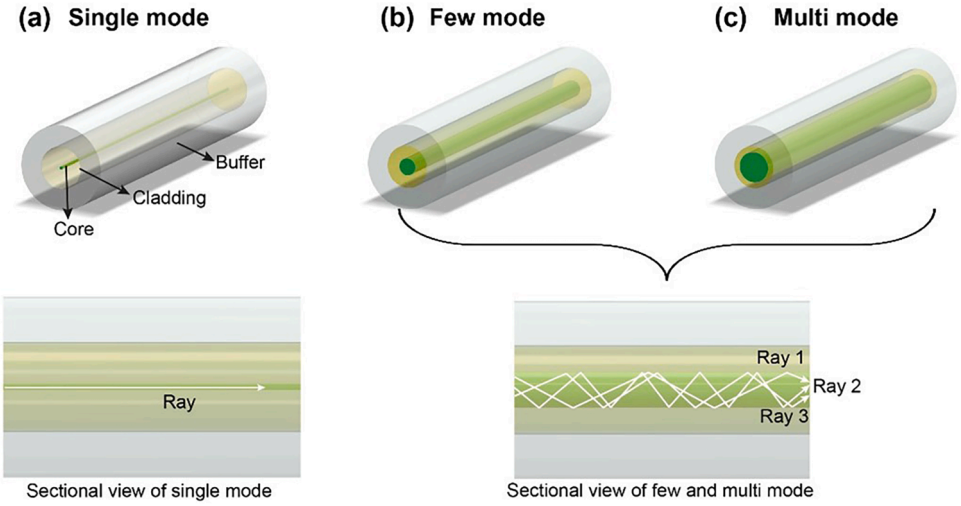

Fig. 10. Different optical fibers: (a) a single-mode fiber (SMF), (b) a few-mode fiber, (3) a multi-mode fiber.

(Zhou et al., 2006, Zhou, 2007). To further increase the detected light intensity, multi-mode fibers with a larger core diameter have been used to accommodate larger sensor arrays (e.g., 5 × 5, 32 × 32, 192 × 128, 500 × 500, 512 × 512 SPAD arrays). Usually, these SPAD arrays are set up in a way (Eq. (40)) that each pixel measures a single speckle on average. However, these detectors only have fill factors of 1-15% so there can be mismatches in the position.

Additionally, the PDE of SPAD arrays is often lower than single detectors, reducing *SNR* (Sie et al., 2020; Liu et al., 2021; Wayne et al., 2023; Johansson et al., 2019; Mattioli della Rocca et al., 2023). For more details on large SPAD arrays, see Section 3.3. He *et al.* (He et al., 2013) compared single-mode, few-mode, and multi-mode fibers on the detection side, and concluded that few-mode and multi-mode detection fibers can improve SNR compared with single-mode fibers, but it reduces β.

3.3. Sensors

Detectors are pivotal in DCS systems for accurate BF measurements, with the advances being intricately connected to the adoption of new high-efficiency massively parallel detectors.

In early DCS systems, photomultipliers (PMTs) were commonly employed for detecting single photons (Boas and Yodh, 1997; Boas et al., 1995). However, PMTs are bulky, so early systems only contain a few channels. Additionally, driving these PMTs requires a high bias voltage, at least hundreds of volts, to start the electron multiplication process. These requirements pose challenges for developing compact and portable devices.

In the last two decades, avalanche photon diodes (e.g., APDs, such as the SPCM series, Excelitas, Canada) (Irwin et al., 2011; Han et al., 2015; He et al., 2013) were used nearly exclusively in DCS systems, replacing PMTs. APDs, known for their high sensitivity, leverage an internal avalanche multiplication effect for capturing single photons. These detectors offer several benefits compared with PMTs, including lower cost, simpler operations, and a smaller size. Although APDs offer high quantum efficiency, they are prone to higher dark current and noise in low-light conditions (Lawrence et al., 2008). Additionally, these detectors are typically single-channel devices. In DCS, each speckle grain carries independent information about the dynamic scattering process. By averaging the autocorrelation signals from multiple speckles, we can enhance the SNR. However, advances in CMOS manufacturing

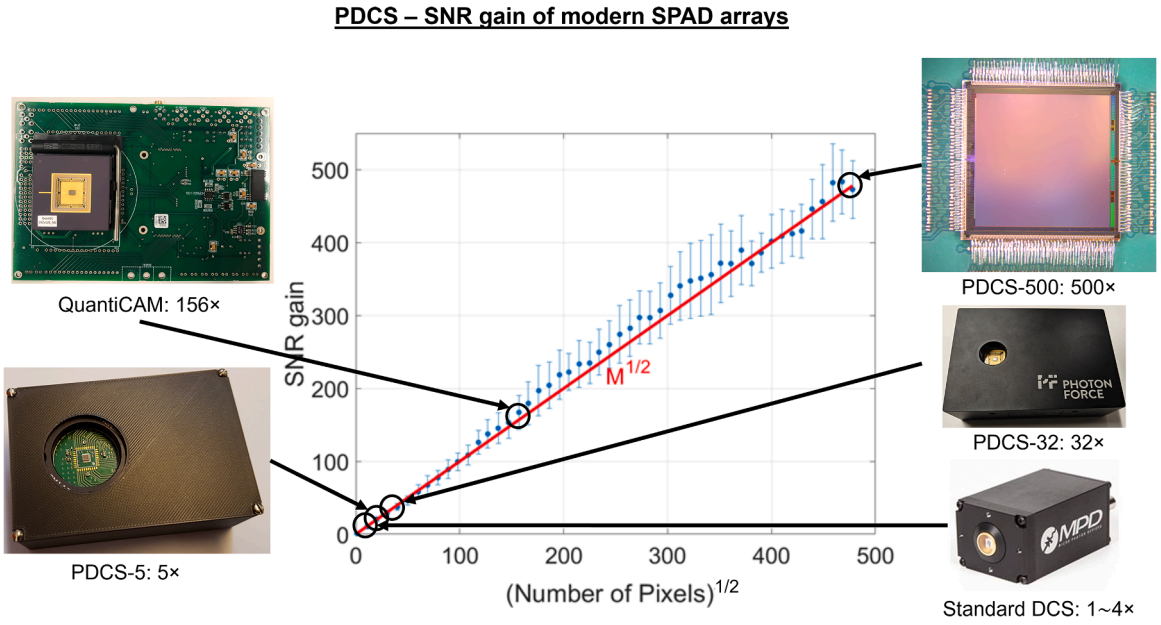

Fig. 11. SNR-vs-pixels plot adopted from Wayne et al. (2023), with different SPAD sensors employed in DCS systems.

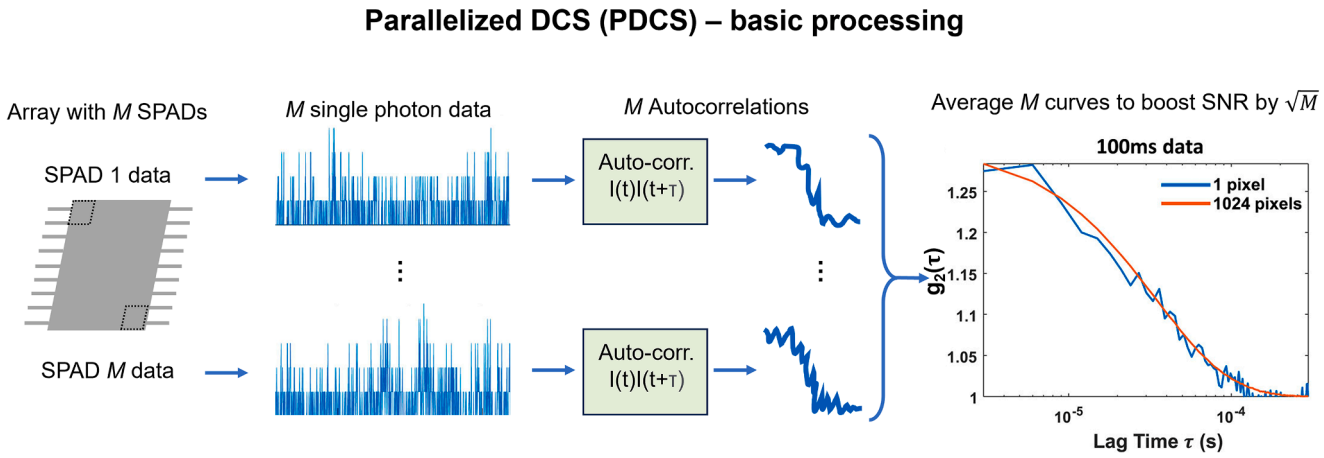

Fig. 12. A schematic layout of the SPAD array with representative raw data of temporal light intensity fluctuations from single pixels and the corresponding intensity autocorrelation curves. The blue and red lines in the rightmost figure represent the autocorrelation curves of a single pixel and the whole SPAD array (1024 pixels), respectively. Data and plots are adopted from Liu et al. (2021).

technologies have enabled the integration of large SPAD arrays on a single chip, offering highly parallel single-photon detection.

Highly integrated CMOS SPAD arrays were boosted first by 3D/time-resolved fluorescence imaging applications (Niclass et al., 2005; Stoppa et al., 2007; Mosconi et al., 2006), and later Richardson *et al.*'s low-noise SPAD structures (Richardson et al., 2009) emerged from the EU6 MEGAFRAME project (EU6 MEGAFRAME, 2024). These SPAD arrays contain either time-correlated single-photon counting (TCSPC) or time-gating modules for time-of-flight or traditional photon counting measurements (Mattioli della Rocca et al., 2023; Li et al., 2010; Richardson et al., 2009; Veerappan et al., 2011; Le Francois et al., 2021; Xiao et al., 2021; Morimoto et al., 2020).

Using SPAD arrays in a multispeckle approach directly enhances SNR, with an enhancement of the square root of the number of independent speckle measurements. Using such new sensors in DCS experiments is straightforward without increasing the setup complexity. Dietsche et al. (2007) verified this method by grouping 28 individual SPADs, enhancing SNR by $\sqrt{28}$. Johansson et al. (2019) first developed a 5 × 5 SPAD DCS system to demonstrate an improved SNR on milk phantoms and *in vivo* blood occlusion tests, followed by 32 × 32 (Liu et al., 2021; Sie et al., 2020; Xu et al., 2022), 192 × 128 (Mattioli della Rocca et al., 2023), 500 × 500 (Kreiss et al., 2024; Wayne et al., 2023), and 512 × 512 (Mattioli della Rocca et al., 2024) (not shown in Fig. 11). These systems significantly improve SNR by a factor of $\sqrt{N}$, where N is the number of individual pixels. Fig. 11 highlights the evolution of SPAD-based DCS systems (from APD to the state-of-the-art large SPAD arrays 512 × 512) with an enhanced SNR gain from 1 to ~500.

Besides SNR and PDE, the exposure time of SPAD arrays is another critical consideration, as it defines the interval between two adjacent time lags $\Delta\tau$ of the autocorrelation curves. Especially for fast decay rates (e.g., at large source-detector separations or for high flow rates), the relatively slow frame rate of large SPAD arrays (3 μs for 32 × 32(Liu

Table 2
Existing DCS systems using SPAD array and other representative sensors.

Approaches	Detector	Laser, wavelength (nm)	N_{pixel}	Applications	PDE	Fill factor	Frame rate (kHz/kfps)	ρ (cm)	year	Refs.
CW	SPAD	785	5 × 5	Phantom, blood perfusion	8%	1.5%	1000	2.5	2019	(Johansson et al., 2019)
CW	SPAD	785	32 × 32	Food, skin	8%	1.5%	333	1.1	2020	(Sie et al., 2020)
CW	SPAD	670	32 × 32	Phantom, *in vivo*	16%	1.5%	333	2.1	2021	(Liu et al., 2021)
CW	SPAD	785	500 × 500	Milk phantom, rotating diffuser	15%	10.6%	92.2	3.3	2023	(Wayne et al., 2023)
CW	SPAD	785	192 × 128	rotating diffuser	8%	13%	26	N.A.	2023	(Mattioli della Rocca et al., 2023)
CW	SPAD	785	500 × 500 128 × 500	Human forearm and brain, *in vivo*	15%	10.6%	100 for arm, 300 for brain	4	2024	(Kreiss et al., 2024)
iDCS	SPAD	785	1 × 1	Intralipid phantom	61%	N.A.	N.A.	3.6	2020	(Robinson et al., 2020)
LW-iDCS	InGaAs Linescan camera	1064	2048 × 1	Human brain, *in vivo*	N.A.	N.A.	300	3.5	2023	(Robinson et al., 2023)
iDWS	CMOS	852	512 × 2	Human brain, *in vivo*	N.A.	N.A.	333	2.5	2018	(Zhou et al., 2018)
fiDWS	Line-scan CMOS	852	512 × 2	Human brain, *in vivo*	>35%	N.A.	333	4	2021	(Zhou et al., 2021)
πNIRS	CMOS	785	1024 × 1024	Forearm, forehead, human brain	80%	N.A.	16	2.5	2022	(Samaei et al., 2022)
TD	SNSPD	785	N.A.	Phantom, *in vivo*	99%	N.A.	N.A	1	2023	(Parfentyeva et al., 2023)

Notes: iDCS stands for interferometric diffuse correlation spectroscopy; iDWS is interferometric diffusing wave spectroscopy; fiDWS presents functional interferometric diffusing wave spectroscopy; πNIRS is abbreviation of parallel interferometric near-infrared spectroscopy, ρ is source-detection separation; SNSPD stands for superconducting nanowire single-photon detectors; PDE is photon detection efficiency.

et al., 2021; Sie et al., 2020; Xu et al., 2022) or 10 μs for 500 × 500 (Wayne et al., 2023)) can be a limiting factor in *in vivo* experiments. Another limitation of the SPAD arrays, though, is the difficulty in light coupling and the thinner active areas – thus an element of the SPAD array has a sensitivity lower than a dedicated SPAD. Nevertheless, the large number of elements allows one to exceed the performance of individual SPADs. Fig. 12 shows the primary processing of a Parallelized DCS (PDCS) system (Liu et al., 2021).

Commercial CMOS cameras are also used in DCS due to their larger array sizes, higher fill factors, and lower cost. However, they do not have single-photon sensitivity. To address this, Zhou et al. (2018) employed a heterodyne detection method to enhance the signal; they also used MMFs to capture multiple speckle patterns, thereby increasing the throughput. They successfully conducted pulsatile blood flow measurements. Meanwhile, Liu et al. (2024) integrated a CMOS detector into a wearable, fiber-free probe, enabling the testing of CBF in neonatal pigs. Of note, the heterodyne detection approach can also be applied in SPAD-based DCS systems, where it offers at least a doubling of SNR and reduced sensitivity to dark counts and environmental light (Robinson et al., 2020).

Very recently, superconducting nanowire single-photon detectors (SNSPDs), a relatively new class of photo-detectors, have been used in TD-DCS systems (Parfentyeva et al., 2023). SNSPD has many advantages, including a high PDE of >80% at longer wavelengths (e.g., 1064 nm), and a better timing resolution (< 20 ps) (Schuck et al., 2013; Esmaeil Zadeh et al., 2021). Nevertheless, SNSPD detectors come with a high cost, necessitating cryostats to maintain an operational temperature of 2 -3.1 K (Esmaeil Zadeh et al., 2021). Moreover, their cooling time spans several hours, and they are noisy and emit a significant amount of heat, constraining their practical applicability in clinical settings. Table 2 summarizes the existing DCS systems with SPAD and representative non-SPAD sensors.

Table 2 shows the existing SPAD-DCS systems. Some SPAD are equipped with a TCSPC module, and TD-DCS systems can timetag detected photons to obtain their ToF, allowing distinguishing early and late arriving photons from fewer or more scattering events respectively, thereby enabling depth-resolved evaluation of BFi within tissues.

Table 3
Existing commercial correlator.

Company	Correlator	Refs.
LSI Instruments	LSI Correlator	(lsinstruments.ch, 2024)
Becker & Hickl GmbH	SPC-QC-004	(becker-hickl, 2024)
ALV	ALV-5000/EPP	(alvgmbh.de, 2024)
Photon Force, Ltd.	On-FPGA in PF's MF32 Sensor	(photon-force.com, 2024)

3.4. Correlators (incl. on-FPGA correlators)

To date, most DCS instruments employ commercial hardware correlators (Durduran et al., 2009; Munk et al., 2012; Cheung et al., 2001; Durduran et al., 2004; Sunar et al., 2007; Shang et al., 2009) to process detected signals and record the arrival of a Transistor-Transistor Logic (TTL) digital pulse for every photon from a photon counting detector. A commercial correlator (Diop et al., 2011), for example, uses the distribution of arrival times to quantify the temporal fluctuation of detected intensity. Traditionally, correlators embed a multi-τ processor (Schätzel et al., 1988; Schatzel, 1990; Schätzel, 1987) to compute the autocorrelation functions over a long delay period; this design was derived from early experiments in DLS (Cipelletti and Weitz, 1999) and diffusing wave spectroscopy (DSW) (Dietsche et al., 2007), primarily conducted on non-biological samples.

There are two kinds of hardware digital correlators, linear and multi-τ correlators, as shown in Fig. 13. Usually, the multi-τ framework is based on a logarithmic spacing spanning a massive lag-time range with a small number of channels without substantial sampling errors. Additionally, the multi-τ scheme significantly reduces the computational load compared with linear correlators. Although hardware correlators can operate at a faster sampling speed and offer real-time computing with a wide lag time dynamic range, they are relatively costly and not

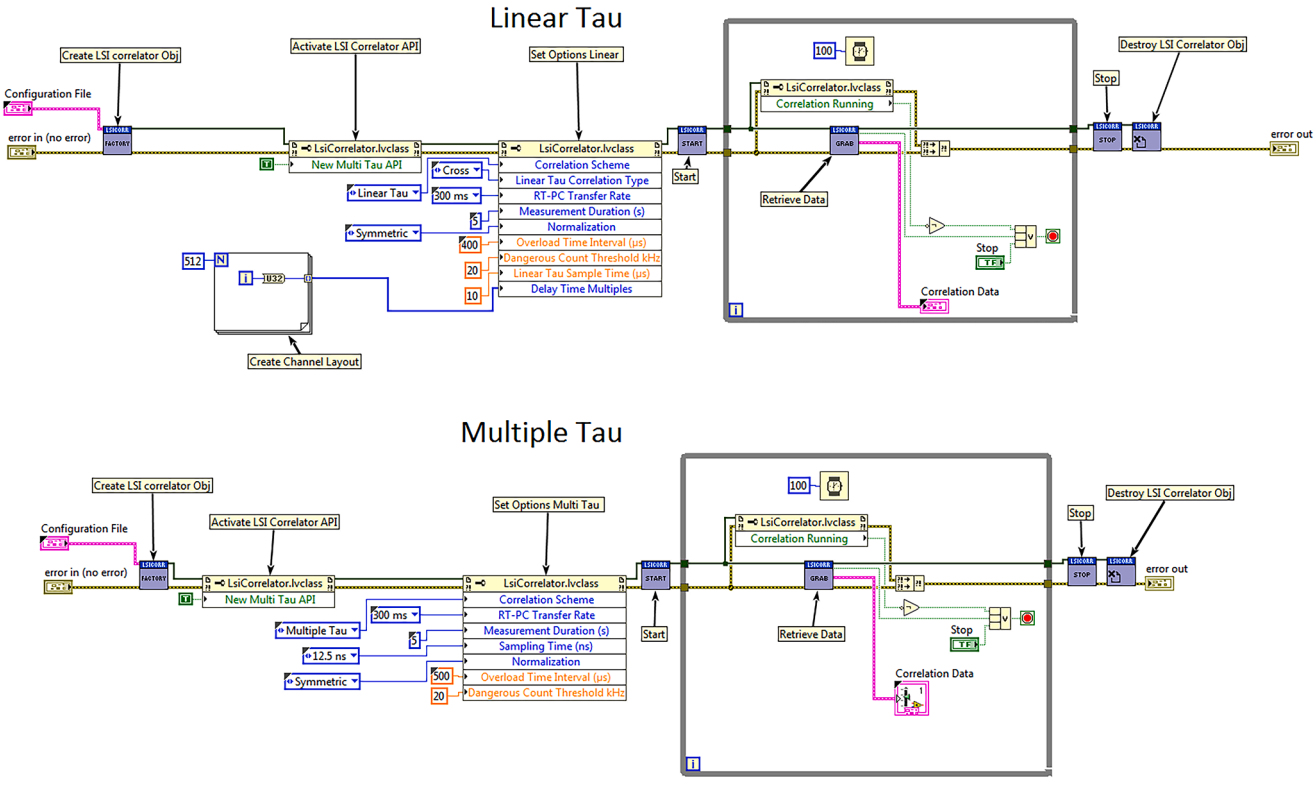

Fig. 13. Diagrams for linear- and multi-tau correlators provided by the CCO of LS Instruments, Dr Ian Block.

flexible since the fixed number of bits per channel results in a fixed lag time scale. Meanwhile, software correlators (Magatti and Ferri, 2001; Magatti and Ferri, 2003) have also been developed. For example, Dong et al. (2012) proposed a fast Fourier transform (FFT)-based software correlator in 2012, reaching a sampling rate of ~ 400 kHz. In 2016, Wang et al. (2016) designed another software correlator using the shift-and-add method, and the temporal resolution can be 50 ~ 100 Hz. Compared with Dong's FFT correlator, Wang's correlator is less memory intensive. Although they show comparable performances to commercial hardware correlators and have notable flexibility, cost-effectiveness and adaptability advantages, they require high-performance processors for real-time data analysis. As a result, field programmable gate array (FPGA) based correlators (Mattioli della Rocca et al., 2023; Moore and Lin, 2022; Moore et al., 2024) are becoming popular, as they significantly increase computational power, making low-cost real-time applications possible. For most DCS applications with SPAD arrays, the autocorrelations are usually post-processed (Wayne et al., 2023; Johansson et al., 2019; Sie et al., 2020; Liu et al., 2021) and on-FPGA solutions (Mattioli della Rocca et al., 2023) are trendy. Table 3 shows the existing commercial correlators.

3.5. Comparison between CW-, TD- and FD-DCS

Conventionally, enhancing depth sensitivity in CW-DCS measurements involves using a larger ρ. This allows detecting photons with longer pathlengths. An inherent drawback of this approach is the reduced detection of photons at a large ρ, reducing the SNR of g_2. Although Yodh et al. (1990) have demonstrated pathlength-resolved DCS, their method required nonlinear optical gating and high laser powers, which are unsuitable for *in vivo* applications. Sutin et al. (2016) first reported a novel time-domain (or pathlength-resolved) DCS on phantoms and a rat brain, showing the potential for clinical applications. Compared with CW-DCS, there are many advantages in TD-DCS:

Firstly, TD-DCS can measure the time point spread function (TPSF) of the tissue. Consequently, we can apply photon diffusion theories developed for time-domain near-infrared spectroscopy (TD-NIRS) to estimate tissue optical properties using the TPSF. Thus, we reduce errors in estimating dynamical properties, as we do not need to assume optical property values as traditional CW-DCS systems do (Sutin et al., 2016).

Secondly, TD-DCS adds one further variable time, which can be exploited to select photons to increase the depth sensitivity (Martelli et al., 2016). Typically, the photons with a longer pathlength travelled deeper into the medium before reaching the detector. In contrast, those taking a shorter pathlength from source to detector reach only superficial tissue layers. Time-of-flight (ToF) measurements can achieve a higher depth resolution, as the ToF is proportional to the pathlength through the medium. Consequently, when computing the autocorrelation only with photons showing a ToF below a specific threshold, we can estimate the dynamic properties of the superficial layers, whereas a longer ToF allows for assessing deeper layers.

Thirdly, the pulsed laser utilized in the TD-DCS system can be integrated into the TD-NIRS setup (Samaei et al., 2021). This integration enables simultaneous measurements of NIRS and DCS, providing a comprehensive understanding of blood flow and hemodynamics variations. A temporal resolution of approximately one second and a favourable SNR in dynamic *in vivo* measurements was validated (Pagliazzi et al., 2017).

However, the primary obstacle preventing the broad adoption of TD-DCS is the need for an optimal pulsed laser (in power, pulse width, coherence, stability, and cost, around 6-fold more expensive than CW lasers). The effect of each of these factors has been evaluated in different studies, and various data processing strategies have been introduced to overcome the destructive influence of the instrument response function (IRF) (Colombo et al., 2019) and the limited coherence length of the emitter. Moreover, Colombo et al. (2020) demonstrated the contamination of non-moving scatters on the TPSF using a coherent pulsed laser utilized in the TD-DCS technique. Samaei et al. (2021) have conducted the systematic discussion. Another drawback is that using narrow time gates to calculate the autocorrelation limits the SNR due to the scarcity of photons. Consequently, its applicability to *in vivo* experiments on human tissue is also restricted (Pagliazzi et al., 2017). Although Ozana et al. (2022) have designed a functional TD-DCS system that combines an optimized pulsed laser (a custom 1064 nm pulse-shaped, quasi transform-limited, amplified laser source), it is still costly, primarily due

Table 4
Representative existing time-domain DCS systems.

Year	Laser	Wavelength (nm)	Average power (mW)	Repetition rate (MHz)	Detection technique	IRF FWHM (ps)	Applications	Refs.
2016	DBR	852	50	150	Red-enhanced SPAD	150	Homogenous liquid phantom and small animal	(Sutin et al., 2016)
2017	Ti: Sapphire	785	NA	100	SPAD	100	Two-layer liquid phantoms, forearm muscle, and adult human forehead	(Pagliazzi et al., 2017)
2018	VisIR STED, PicoQuant	767	50	NA	Red-enhanced SPAD	500	Homogenous liquid phantoms	(Cheng et al., 2018)
2018	Ti:Sapphire	785	NA	100	Gated single-photon avalanche diode	350	Forearm muscle	(Pagliazzi et al., 2018)
2019	VisIR-500	767	$\leq$ 1500	$\leq$ 80	SPAD	550	Homogenous liquid phantoms, forearm muscle, and adult human forehead	(Tamborini et al., 2019)
2019	Ti:Sapphire	785	NA	100	SPAD	400	Homogenous liquid phantoms	(Colombo et al., 2019)
2020	Ti:Sapphire	1000	30	100	InGaAs PMT	NA	Homogenous liquid phantoms and forearm muscle	(Colombo et al., 2020)
2021	LDH-P-C-760, Picquant	760	12	80	SPAD	90	Two-layer liquid phantoms, forearm muscle, and adult human forehead	(Samaei et al., 2021)
2022	Custom-made two-stage fiber amplified pulsed laser	1064	100	1-100	SNSPD	150-600	Two-layer liquid phantoms and adult human forehead	(Ozana et al., 2022)
2023	Ti:Sapphire	785	NA	100	SNSPD	100-200	Homogenous liquid phantoms and adult human forehead	(Parfentyeva et al., 2023)

Note: SPAD stands for Single-Photon Avalanche Diode, and SNSPD stands for Superconducting Nanowire Single-Photon Detectors

to the SNSPD.

Unlike CW-DCS, both TD- and FD-DCS can retrieve dynamic optical properties (e.g., BFi) and static optical properties (e.g., μ_a and μ_s'), which are typically assumed in the conventional CW-DCS measurements. FD-DCS eliminates the requirement for collocated sources and phase-sensitive detectors, promising a portable and cost-effective system. Through data acquisition at a single ρ, FD-DCS effectively minimizes partial volume effects. This technology eliminates the need for extensive calibration in data analysis by acquiring flow and absorption from intensity-normalized data. FD-DCS shows high-speed acquisition, as flow and oxygenation information are inherently present in the dataset. Moreover, the implementation of FD-DCS is simplified by replacing a traditional DCS system's source with an intensity-modulated coherent laser. The detection mechanism remains unchanged, leading to reduced development time and cost.

Typically, to separate deep from superficial blood flow signals for CW-DCS, adding more detectors at different ρ to obtain multiple-distance measurements is needed, which, however, increases the cost. General linear models (GLM) have been applied to CW-DCS data from multiple source-detector separations (ρ) to regress out the effect of superficial flow. Therefore, large-ρ DCS data is expressed as a linear combination of superficial blood flow (measured at a small ρ) and the desired deep blood flow (Cowdrick et al., 2023), a method derived from fNIRS (Von Lühmann et al., 2020). Table 4 summarizes representative existing TD-DCS systems, which use time-gating and TCSPC electronics to distinguish between photons travelling superficial layers and those propagating deeper into the tissue.

In contrast to fNIRS, which measures flow volume, DCS directly measures the BFi, which is related to flow speed. Since the flow speed differs significantly over different vessel diameters and tissue layers, the relation between superficial BFi and deep BFi is not linear. Therefore, new analysis tools that integrate additional data on vasculature structure are required to derive more accurate deep flow estimation from such multiple-distance DCS measurements.

4. Data processing

The accuracy and performance of multilayered analytical models have been extensively evaluated in prior literatures (Gagnon et al., 2008a; Verdecchia et al., 2016; Zhao et al., 2021; Zhao et al., 2023; Samaei et al., 2021; Milej et al., 2020; Wu et al., 2022; Forti et al., 2023). In addition to the analytical models described in Section 2, other data processing methods have been introduced to distinguish cerebral and extracerebral information. Baker et al. (2015) introduced a pressure measurement paradigm combined with the modified Beer-Lambert law (Baker et al., 2014) and multi-distance measurement to reduce the extracerebral contamination from the signal associated with the deep layers. Furthermore, Samaei et al. (2021) extended the bi-exponential model utilized in interferometric near-infrared spectroscopy (iNIRS) (Kholiqov et al., 2020) to describe the TD-DCS signals influenced by scatterers moving at different speeds. They also conducted experimental validation using layered phantoms and *in vivo* experiments.

Traditionally, to extract BFi and β, we fit measured g_2 with Eqs. (4), (9), (18), (24), (25), (31), (32) and (35) in Section 2 by minimizing the cost function $\chi^2 = \sum_i \left[g_{2,analytical}(\rho,\tau_i) - g_{2,measured}(\rho,\tau_i)\right]^2$. Nonlinear least square fitting routines, e.g., Levenberg-Marquardt (Li et al., 2005, Mazumder et al., 2021), fminsearchbnd (Verdecchia et al., 2016) are

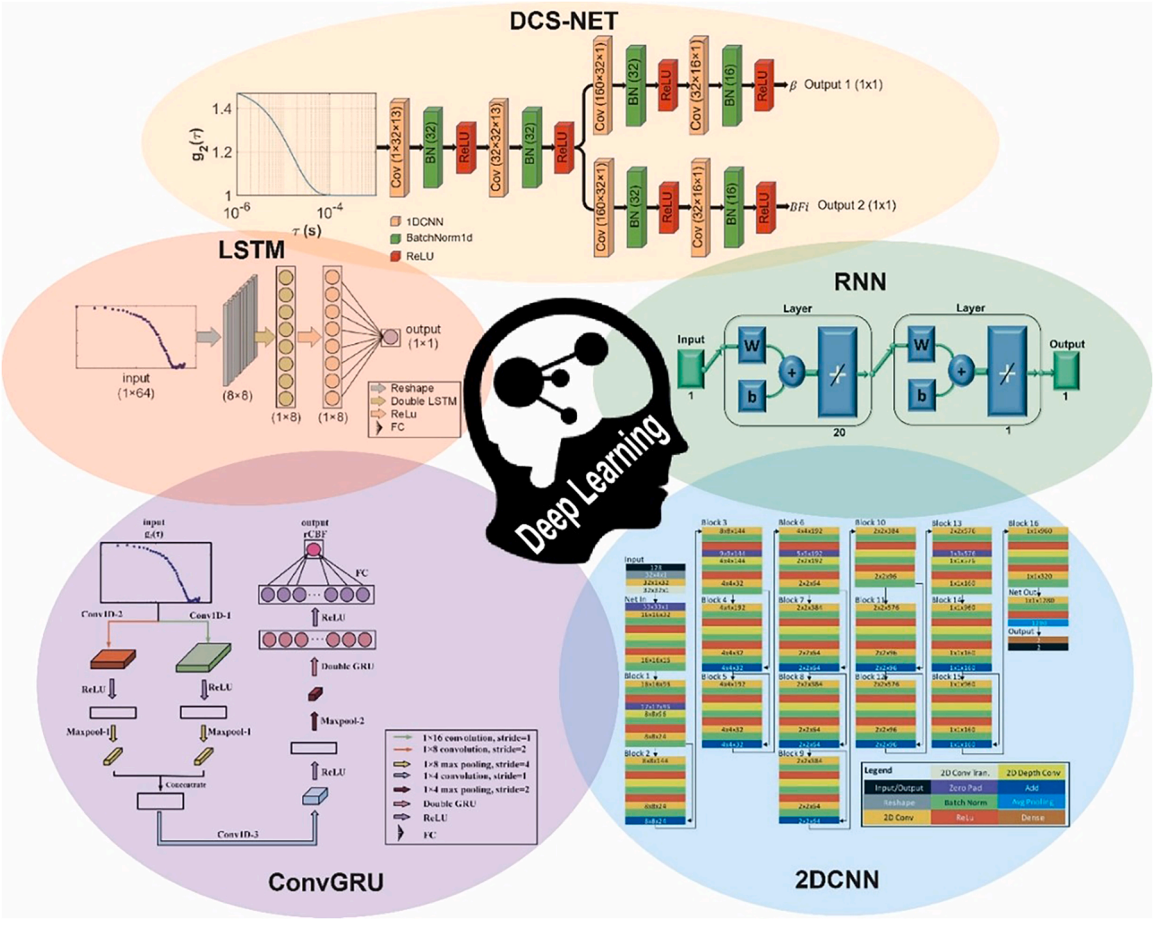

Fig. 14. The existing deep learning model applied in DCS, including RNN (Zhang et al., 2019), 2DCNN (Poon et al., 2020), LSTM (Li et al., 2021), ConvGRU (Feng et al., 2023) and DCS-NET. All of the graphs are re-printed from the published literatures.

Table 5
Comparison of existing AI methods for BFi estimation.

Model	Training Parameters	Training time	Total layer	ρ (mm)	Year
RNN (Zhang et al., 2019)	174080	N/A	20	25	2019
CNN(2D) (Poon et al., 2020)	75552	~ 30.5 (hour)	161	27.5	2020
LSTM (Li et al., 2021)	1161	N/A	2	15	2021
ConvGRU (Feng et al., 2023)	11557	N/A	10	20	2022
LSTM (Nakabayashi et al., 2023)	N/A	N/A	5	30	2023
DCS-NET (Wang et al., 2024)	25506	~ 13 (minute)	18	5 to 30	2024

Notes: the training parameters of RNN and CNN(2D) are not given in the literature; we calculate them according to the structure shown in the literature.

usually used to quantify BFi. These approaches, however, are iterative, and sensitive to data noise. To address these constraints, the N^{th}-order (NL) algorithm (Shang et al., 2014; Shang and Yu, 2014), least-absolute minimization (L1 norm), and support vector regression (SVR) were introduced (Zhang et al., 2018). Yet, with the NL framework, the extraction of BFi is determined by the chosen linear regression approach (Zhang et al., 2018). Although L1 norm and SVR are novel for processing DCS data, they are sensitive to signal deviations (Vapnik, 1999). For example, the computation time for BFi is 28.07 and 52.93 s (Zhang et al., 2018) (using the Lenovo ThinkCentre M8600t desktop with a 3.4 GHz CPU and 16GB memory) when employing L1 norm and SVR, respectively, still too slow for real-time applications.

In 1986, Dechter introduced "deep learning" (DL) to the machine learning community (Dechter, 1986). With rapid advances in computing technologies, DL has become a game-changer in many fields, including photonics (Ma et al., 2021), chemistry (Mater and Coote, 2019), biology (Ching et al., 2018), and medical diagnosis (such as electroencephalogram (EEG) and electrocardiogram (ECG) (Zhang et al., 2020; Liu et al., 2021)), but is not yet broadly used in DCS. Recently, Zhang et al. (Zhang et al., 2019) proposed the first recurrent neural network (RNN) regression model to DCS, followed by 2D convolution neural networks (2DCNN) (Poon et al., 2020), long short-term memory (LSTM) (Li et al., 2021) and ConvGRU (Feng et al., 2023). LSTM, as a typical RNN structure, has proven stable and robust for quantifying relative blood flow in phantom and *in vivo* experiments (Li et al., 2021). 2DCNN, on the other hand, tends to require massive training datasets for complex structures, demanding memory resources. ConvGRU, the newest deep learning method introduced to DCS, has also exhibited excellent performances in *BFi* extraction. Although the training of DL takes a long time, once it is done, DL is much faster than traditional fitting methods and more promising for real-time analysis and display. Fig. 14 and Table 5 summarize existing DL methods applied to DCS. It shows that DCS-NET's training is much faster than two-dimensional CNN, approximately 140~fold faster. Although the remaining models, RNN, LSTM and ConvGRU have fewer total layers, they are limited to a specific ρ (Wang et al., 2024). Xu et al. (2022) introduced a different DL approach and trained a deep neural network on DCS data of temporal speckle fluctuations from 12 fibers at different surface locations to reconstruct videos of flow dynamics 8 mm beneath a decorrelating tissue phantom. The reconstructed images had a millimetre-scale spatial resolution and a temporal resolution of 0.1-0.4 s.

5. Applications

DCS has a broad range of applications, particularly when integrated with near-infrared spectroscopy (NIRS) (Buckley et al., 2014), Doppler ultrasound, time-resolved near-infrared technique (TR-NIR) (Diop et al., 2010, Diop et al., 2010), and frequency-domain NIRS (Shang et al., 2017). This integration provides valuable insight into tissue oxygenation, blood oxygen metabolism, and hemodynamics (Milej et al., 2020; Milej et al., 2020), making DCS useful for neuromonitoring, tissue and skeletal muscle blood flow monitoring, tumor diagnosis and therapy, and neonatal cardio-cerebrovascular health evaluation (Shang et al., 2017).

This section includes an overview of DCS applications in animals, followed by applications in neonates, focusing on perinatal care, cardio-

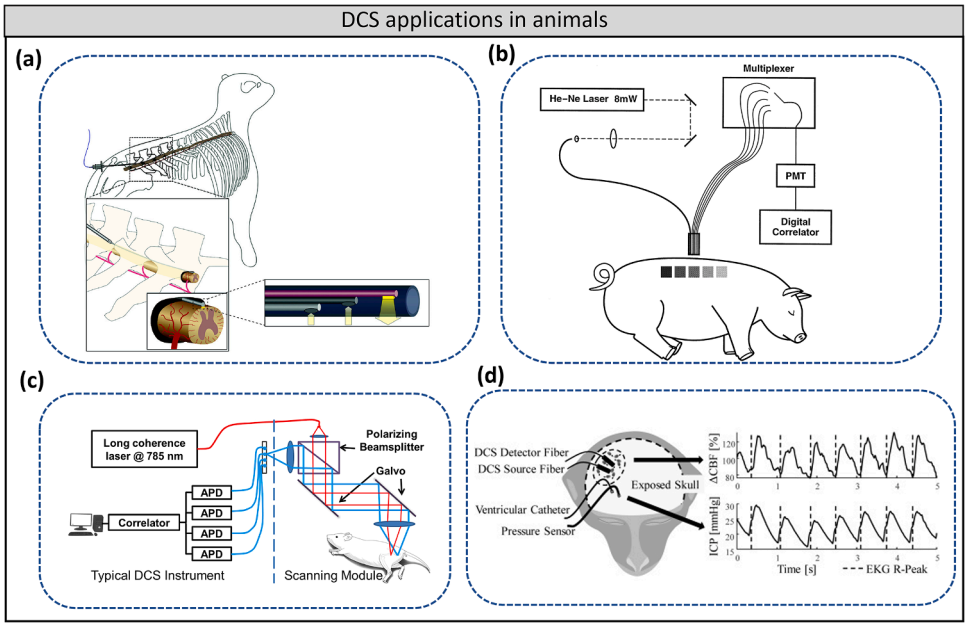

Fig. 15. (a) Detailed schematics of measurements on sheep, featuring the instrument and its thin fiber optic probe, images adopted from Ref. Mesquita et al. (2013); (b) The setup for pig experiments. The shaded areas on the pig indicate burns of various depths. Figures were reproduced from Ref (Boas and Yodh, 1997); (c) The non-contact scanning system set-up for mice. (black lines: outline of the bones; red lines: outline of the graft). Figures were reproduced from Ref. Han et al. (2016); (d) Experiment setup with the placement of optical fibers and pressure sensor as well as the catheter on the exposed skull of monkey. The traces at the right show an example of changes in cerebral blood flow (ΔCBF) and ICP. Figures were reproduced from Ref. Ruesch et al. (2020).

cerebral diseases, and children's brain health. Finally, it explores DCS applications in adults, divided into neurovascular assessment, cardio-cerebrovascular diseases, skeletal muscle health, and tumor diagnosis and therapy.

5.1. Animals

DCS has been applied to animals since the late 1990s, such as estimating burn depth in pigs (Boas and Yodh, 1997) (Fig. 15(b)) and probing rat vascular hemodynamics (Cheung et al., 2001) with a hybrid DCS-NIRS instrument in 2001. Carp *et al.* used DCS to examine CBF during hypercapnia-induced cerebrovascular perturbation, with MRI-ASL as the standard measuring reference (Carp et al., 2010). In addition, Menon *et al.* were the first to use DCS for tumor monitoring (Menon et al., 2003) by assessing tumor oxygenation in mice with human melanoma xenografts achieved by vascular endothelial growth factor (VEGF) transfection. They combined DCS with Doppler ultrasound (DUS) to investigate microvessel density (MVD), BF, blood volume (BV), blood oxygen saturation, tissue oxygen partial pressure (pO_2), and oxygen consumption rate.

Moreover, DCS is pivotal in monitoring tumor blood flow changes in animal studies related to photodynamic therapy (PDT). Marrero et al. (2011), Yu et al. (2005), and Busch et al. (2009) have employed DCS to monitor BF in tumors before, during, and after PDT. Sunar et al. (2007) also used DCS to assess anti-vascular and ionizing radiation therapies. Farzam et al. (2017) observed a dropped BFi in the high oxygen saturation tumor region using DCS and DOS after anti-vascular chemotherapy. These preclinical investigations have paved the way for human cancer research and clinical applications.

Ischemia monitoring assesses potential damage to the brain or the secondary brain injury and paraparesis. Experiments have been conducted to study the perturbation of hemodynamics and cerebral blood metabolism induced by ischemia brain injury in rats (Culver et al., 2003), piglets (Diop et al., 2011) and sheep (Mesquita et al., 2013), see Fig. 15. Notably, Diop *et al.* developed a method integrating (TR-NIR) and DCS to quantify the absolute cerebral metabolic rate of oxygen ($CMRO_2$) (Diop et al., 2011; Verdecchia et al., 2013).

To further investigate vessel hemodynamics, diffuse correlation tomography (DCT) has been developed to provide 3D blood flow contrast imaging by measuring blood flow perturbations caused by optical heterogeneities, providing blood flow contrast imaging of the region of interest (Zhou et al., 2006; Han et al., 2016; Huang et al., 2021). DCT is a safe and cost-effective imaging technique offering real-time monitoring and functional information on hemodynamics, complementing other imaging modalities like MRI, CT, or PET scans.

5.2. Neonates

The cortex of newborns is more easily detectable as the scalp and skull are much thinner in newborns and more light reaches the cerebral tissue than in adults. Thus, neonates are an attractive population for bedside DCS measurements. Generally, DCS is often combined with NIRS, which can measure human blood metabolism (Villringer and Chance, 1997; Danen et al., 1998) or transcranial Doppler ultrasound (TCD), enabling comprehensive measurements of microvascular blood flow and oxygen metabolism in neonatal human subjects (Buckley et al., 2014).

5.2.1. Perinatal care

Babies born before 37 weeks of pregnancy are premature, and preterm birth is the leading cause of neonatal mortality (Ohuma et al., 2023). According to the World Health Organization (WHO) 2023 report, there are around 13.4 million premature babies worldwide (Preterm birth, 2023). Premature babies are more likely to suffer from brain injuries such as HIE, stroke, and periventricular leukomalacia, related to neurological deficits (Kiechl-Kohlendorfer et al., 2009). Roche-Labarbe *et al.* developed a hybrid instrument combining DCS for measuring CBF and quantitative FD-NIRS for assessing cerebral tissue oxygenation (StO_2) and CBV in premature neonates. The results indicate that the CBF-CBV correlation is unstable in premature neonates (Roche-Labarbe et al., 2010). In addition, Germinal matrix-intraventricular hemorrhage (GM-IVH) in premature neonates can be monitored by measuring CBF and $CMRO_2$ to identify the vulnerability of potential brain damage in newborns (Lin et al., 2016). Buckley *et al.* used DCS for continually monitoring CBF in the middle cerebral arteries of low birthweight premature infants during a postural manipulation, discovering a significant correlation between TCD and DCS measurements (Buckley et al., 2009). CBF monitoring during the first three days after birth was conducted to assess the risk of brain injury due to CBF instabilities in preterm infants (Rajaram et al., 2022). DCS holds a promising potential for preterm human infants' brain health care.

5.2.2. Neonatal cardio-cerebral diseases

DCS is also a promising tool for the monitoring of congenital heart defects in newborns. Durduran *et al.* used a hybrid NIRS-DCS instrument to study the changes in oxyhemoglobin, deoxyhemoglobin, total hemoglobin concentrations, $CMRO_2$, and CBF during hypercapnia. The validation of CBF and $CMRO_2$ was conducted using MRI-ASL, and the results showed a good agreement with DCS measurements ($R = 0.7$, $p = 0.01$) (Durduran et al., 2010). Buckley et al. (2013) and Shaw et al. (2023) measured changes in cerebral hemodynamics and oxygen metabolism during cardiac surgeries using DCS and DOS to evaluate the risk of surgery duration and surgical procedures, respectively. In addition, therapeutic hypothermia (TH) for neonatal HIE has also been studied using hybrid FD-NIRS and DCS (Dehaes et al., 2014; Sutin et al., 2023). Sutin et al. (2023) revealed the effects presented by therapeutic hypothermia (TH) on cerebral hemodynamics and blood oxygen metabolism by measuring CBF and $CMRO_2$, indicating that $CMRO_2$ is a good indicator of TH evaluation and can be measured repeatedly at the point of care.

5.2.3. Children brain health assessment

Busch et al. (2016) observed CBF attenuation in the brains of children (aged 6-16 years) diagnosed with obstructive sleep apnoea syndrome (OSAS) and hypercapnia using DCS. Besides, Nourhashemi et al. (2023) combined EEG, NIRS, and DCS to simultaneously capture changes in electrical and optical dynamics in children (aged 6-10 years) affected by absence epilepsy. The outcomes revealed a consistent correlation among EEG, NIRS, and DCS, suggesting that DCS holds promise in detecting hemodynamic changes of pediatric brain disorders. Moreover, DCS has been employed for real-time CBF measurements during chronic transfusion therapy for children with autism spectrum disorder (Lin et al., 2023) and sickle cell diseases (Lee et al., 2019; Cowdrick et al., 2023; Lee et al., 2022). Fig. 16 shows representative applications of DCS in neonates.

5.3. Adults

In this section, we focus on DCS applications in human adults and divide them into four sections: neuroscience study, cardio-cerebrovascular diseases, skeletal muscle and exercise physiology study, and tumor diagnosis and therapy evaluation. Fig. 17 shows the use of DCS in adults.

5.3.1. Neurovascular assessment

Measuring CBF facilitates investigating neurovascular coupling, brain injuries, stroke, and neurological disorders. Neurovascular coupling denotes the connection between regional neural activity and subsequent alterations in CBF. The extent and spatial positioning of blood flow fluctuations are intricately connected to shifts in neural activity through a sophisticated sequence of coordinated processes involving neurons, glial cells, and vascular elements (Pasley and

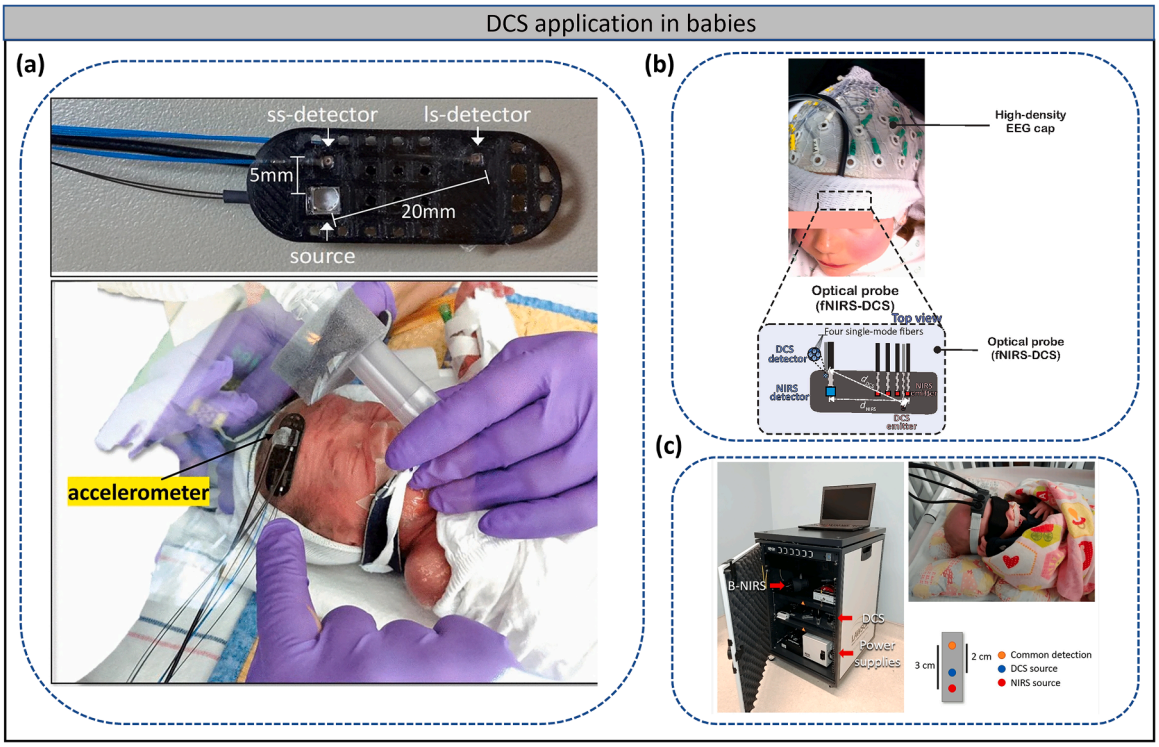

Fig. 16. (a) DCS sensor was attached to the infant's head for blood flow monitoring, figures adopted from Ref. Sunwoo et al. (2022) (b) The high-density EEG cap and optical probe (NIRS-DCS) and schematic representation of the location of the EEG and optical probes on a child's head. The figure was reproduced from Nourhashemi et al. (2023). (c) The hybrid DCS system for neonatal blood flow monitoring, figures reproduced from Ref. Rajaram et al. (2020).

Freeman, 2008). DCS can quantify changes in human cerebral blood flow in response to various stimuli, including sensorimotor cortex activation (Durduran et al., 2004), visual cortex activation (Jaillon et al., 2007; Li et al., 2008), Broca's area activation (Tellis et al., 2018), transcranial magnetic stimulation (TMS) (Mesquita et al., 2013), and vasoactive stimuli (Cowdrick et al., 2023). These studies presented noninvasive and straightforward means of monitoring cognitive neuronal activity in human brains. Older adults with mild cognitive impairment exhibit significantly higher CBF increments during motor and dual-task activities, whereas their counterparts display normal cognitive functions (Udina et al., 2022). Another investigation highlighted the consistency of CBF with the posture changes within a healthy population (aged 20 to 78 years). Zavriyev *et al.* examined the role of DCS during hypothermic circulatory arrests (HCA) therapy among older people (mean age 61.8 ± 19.4 years) (Zavriyev et al., 2021). These findings offer good references for future research on age-related alterations in CBF (Edlow et al., 2010). In addition, DCS has been effectively applied for assessing cerebral hemodynamics under hypotension (Shoemaker et al., 2023), obstructive sleep apnea (Busch et al., 2016), and adult comatose (Johnson et al., 2022). However, most state-of-the-art DCS setups are relatively limited for measuring blood flow in deeper cerebral tissue since the most common source-detector separations only enable measurements at ~1-1.5cm depth, which barely penetrates the non-cerebral tissues of the scalp and skull.

5.3.2. *Cardio-cerebrovascular diseases*

Several studies have assessed human artery diseases and treatments. For example, Carotid endarterectomy (CEA) can lead to hypoperfusion syndrome and potential cerebral ischemia, making cerebral hemodynamics monitoring crucial during and after the procedure. Shang *et al.* found that DCS measured CBF more responsively to internal carotid artery clamping compared to EEG (Shang et al., 2011). Furthermore, Kaya et al. (2022) integrated DCS with NIRS to demonstrate the feasibility of real-time cerebral hemodynamics and oxygen metabolism monitoring during CEA procedures. Mesquita et al. (2013) also established a physiological connection between CBF and oxygenation in patients with peripheral artery disease. CBF during the cardiac cycle has been acquired using DCS before and during ventricular arrhythmia in adults (Lafontant et al., 2022). DCS has also been used for monitoring CBF (Durduran et al., 2009; Favilla et al., 2014) and critical closing pressure (CrCP) (Wu et al., 2021) of ischemic stroke patients, intrathecal nicardipine treatment after subarachnoid hemorrhage (Sathialingam et al., 2023), and thrombolysis therapy evaluation in ischemic stroke (Zirak et al., 2014). In neurocritical care, DCS combined with NIRS serves as an effective bedside tool for managing CBF and head-of-bed treatment for critical brain injuries (Kim et al., 2010; Kim et al., 2014).

5.3.3. *Skeletal muscle health*

DCS is valuable for investigating human skeletal muscle physiology and assessing tissue vascular diseases. Yu *et al.* compared muscle blood flow and oxygenation between healthy individuals and those with peripheral arterial disease during cuff occlusion and plantar flexion exercise (Yu et al., 2005), integrating MRI-ASL with DCS for monitoring BFi (Yu et al., 2007). Shang *et al.* studied muscle blood flow, oxygenation, and metabolism in women with fibromyalgia during exercise (Shang et al., 2012). Matsuda et al. (2022) evaluated local skeletal muscle blood flow during manipulative therapy, which enhanced blood flow with minimal effects on systemic circulatory function (Matsuda et al., 2022). Nevertheless, conventional technologies like DUS, electromyography (EMG), and MRI face challenges with motion artifacts, leading to inaccurate blood flow measurements. DCS offers more reliable measurement (Bangalore-Yogananda et al., 2018), though muscle fiber motion artifacts may still result in overestimating BFi changes. Methods such as dynamometer co-registration (Shang et al., 2010), hardware-integrated gating (Gurley et al., 2012; Henry et al., 2015), and a random walk correction model with FD-NIRS (Quaresima et al., 2019) have been proposed to address this.

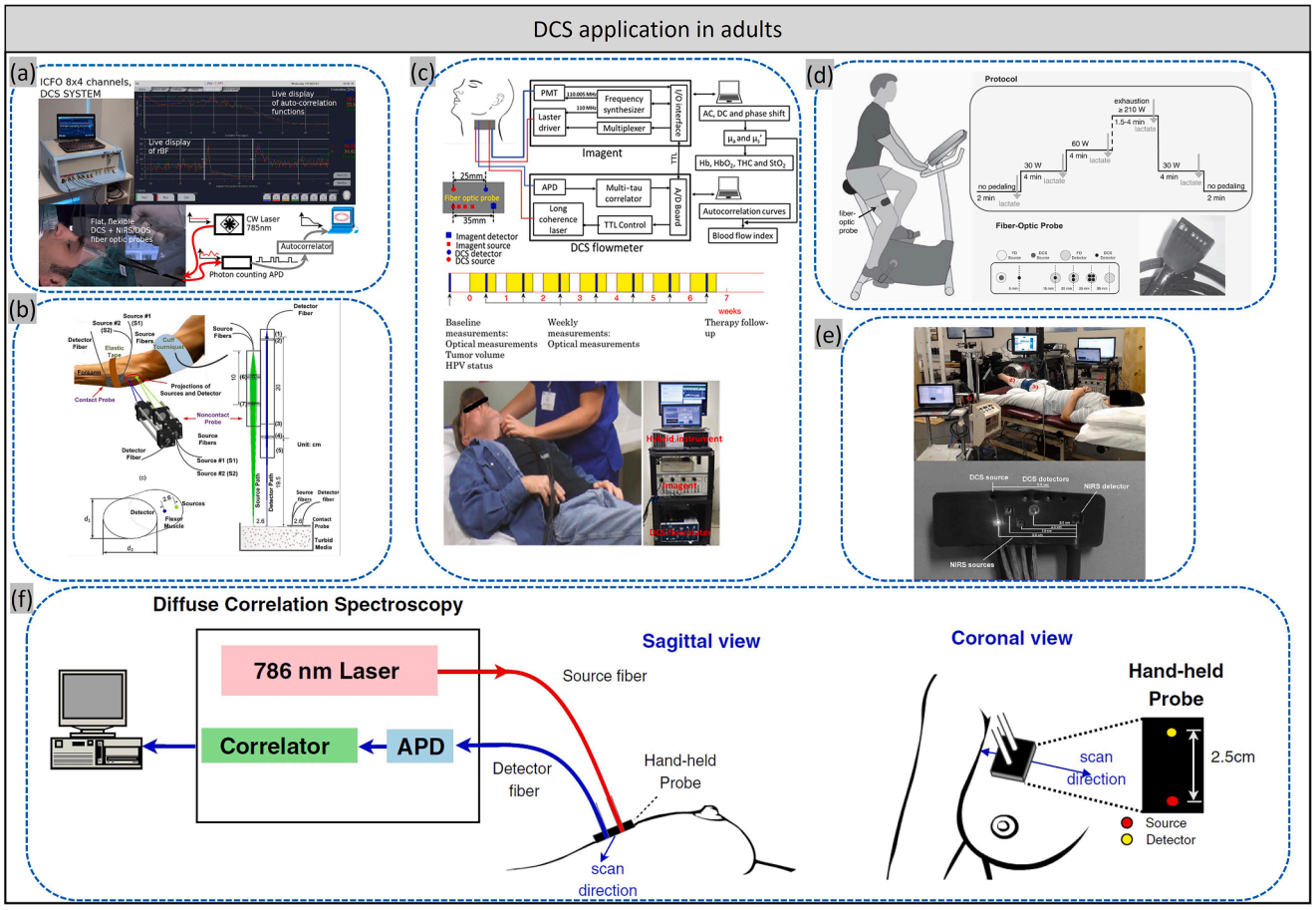

Fig. 17. (a) Hybrid DCS system applied to the human forehead, image reprinted from Ref. Durduran and Yodh (2014); (b) Experimental configuration with a contactless probe, figures adopted from Ref. Li et al. (2013); (c) Schematic of hybrid instrument, hybrid Imagent/DCS instrument for simultaneous measurement of tumor oxygenation and blood flow during chemoradiation therapy, images adopted from Ref. Dong et al. (2016); (d) Drawing of a subject cycling on a stationary bicycle with a multi-distance FDNIRS-DCS probe attached to the right superficial rectus femoris. The figure was adopted from Ref. Zavriyev et al. (2021); (e) Hybrid DCS/NIRS device for muscle measurement. Figures were adopted from Ref. Henry et al. (2015); (f) Diagram of DCS working on a breast, figures adopted from Ref. Choe et al. (2014).

5.3.4. *Tumor diagnosis and therapy evaluation*

DCS has been employed in the diagnosis of human breast cancer, prostate, and neck tumors. Durduran et al. (2005) conducted an initial comparative analysis of blood flow disparities between tumor and normal tissues in the human breast. The investigation revealed a noteworthy increase in blood flow within tumor tissues, paving the way for noninvasive tumor diagnosis. Choe et al. (2014) confirmed these findings, and non-contacted DCT has enabled 3D visualization of blood flow in human breast tumors. Yu et al. (2006) combined DCS with NIRS to measure BF and oxygenation in human prostate cancer and head/neck tumors (Sunar et al., 2006), assessing treatment efficacy. Also, DCS has been used to evaluate photosensitizer 2-1[hexyloxyethyl]-2-devinylpyropheophorbide-a (HPPH)- mediated PDT (HPPH-PDT), showing significant drug photobleaching and reductions in blood flow and oxygenation (Sunar et al., 2010). Additionally, DCS can evaluate chemotherapy (Zhou et al., 2007; Chung et al., 2015) or radiation delivery (Dong et al., 2012) in human tumors.

However, more extensive patient studies are needed for accurate clinical applications, as most studies involved only 7 to 11 patients (Choe and Durduran, 2012) with varying response definitions. Longitudinal studies with larger populations and refined DCS models are necessary for precise clinical use (Yu, 2012; Shang et al., 2017).

In addition to the applications listed above (Figs. 15–17), DCS has also been used for critical care (Poon et al., 2022), anesthesiology (Tagliabue et al., 2023), and thyroid blood flow measurements (Lindner et al., 2016).

6. Discussion and outlook

Non-invasive DCS techniques have great potential for early diagnosis, prognosis, and a broad range of clinical conditions. Although DCS is simple and cost-effective, human applications still face challenges. Increasing DCS's SNR is crucial for effective probing through thick near-surface tissue layers, especially at larger source-detector separations. A solution for increasing SNR is simply increasing the amount of light delivered to tissues under the maximum permissible exposure (MPE) limited by safety standards (ANSI safety limit (ANS Institute, 2007)) or using high photon detection efficiency sensors that collect more scattered photons. Additionally, with new CMOS manufacturing techniques, the improvement in SNR has been shown in multi-speckle DCS systems using SPAD arrays with 5 × 5 (Johansson et al., 2019), 32 × 32 (Sie et al., 2020; Xu et al., 2022; Liu et al., 2021), 192 × 128 (Mattioli della Rocca et al., 2023), 500 × 500 (Wayne et al., 2023), or 512 × 512 (Mattioli della Rocca et al., 2024) pixels. The latest parallelized DCS system with a SPAD array of 500 × 500 pixels has already been demonstrated to boost the SNR by 500, compared to a single SPAD pixel of the same device. In 2020, a SPAD camera with 1024 × 1000 pixels was demonstrated (Morimoto et al., 2020), although its relatively low frame rate of 24 kfps still prevented a practical use in DCS. We believe this ongoing development of larger and faster SPAD technologies (Morimoto et al., 2020; Bruschini et al., 2019) will continue to boost the SNR of DCS, thereby allowing feasible measurements at longer source-detection separation and effectively enabling the measurement

of deeper blood flow.

Another method that has a similar goal is the interferometric approach based on a Mach-Zehnder interferometer. Over the past five years, the interferometric detection for diffusely scattered light in biological tissues has been investigated (Zhou et al., 2021; Zhou et al., 2022; Zhou et al., 2018; Robinson et al., 2020; Kholiqov et al., 2020; James and Powell, 2020; Xu et al., 2020; Zhou et al., 2021; Borycki et al., 2017; Kholiqov et al., 2022). There are many advantages, including:

1) offering comparable or superior functionality to photon counting but at a significantly lower cost per pixel (Zhou et al., 2021; Zhou et al., 2018; Robinson et al., 2020; Zhou et al., 2021);
2) altering the temporal coherence of light proves to be an effective and adaptable method for attaining Time-of-flight (ToF) resolution or discrimination within an interferometric arrangement, eliminating uncertainties for precise signal interpretation (Zhou et al., 2018; Kholiqov et al., 2020; Borycki et al., 2017; Kholiqov et al., 2022);
3) holding significant promise for analyzing blood flow fluctuations, whereas conventional DCS is hindered by its expensive nature and limited throughput (Zhou et al., 2021; Dietsche et al., 2007);
4) insensitive to ambient light, which is a considerable benefit for practical use cases. Recently, Robinson et al. (2023) proposed long wavelength (1064 nm), interferometric DCS (LW-iDCS), which outperforms the long wavelength DCS (LW-DCS) based on SNSPD (Ozana et al., 2021) in terms of SNR and implementation cost. Safi et al. (2021) presented a novel coherence-gated DCS instrument designed for pathlength-resolved measurement of flow and tissue optical properties, utilizing a CW low-coherence source with an interferometric approach, in which specialized pulsed/modulated laser sources with high temporal coherence and speed improvements to traditional DCS detectors are not required. Similarly, Robinson et al. (2024) proposed an enhanced DCS method called pathlength-selective, interferometric DCS (PaLS-iDCS), which improves upon both the sensitivity of the measurement to deep tissue hemodynamics and the SNR of the measurement using pathlength-specific coherent gain. Moreover, PaLS-iDCS does not require expensive time-tagging electronic and low-jitter detectors because of the interferometric detection. However, the drawback of the interferometric approach is its relatively complex setup with a reference arm and higher stability requirements for the platform accommodating the setup.

One substantial advantage of TD-DCS techniques, as described in Section 3.5, is their capability to reduce the superficial layer contamination by selecting photons propagated into the deep tissues. Although TD-DCS measurements are typically conducted at a short ρ, due to the limited coherence length of the currently available emitters, this feature overcomes the influence of short ρ measurements and provides a higher depth sensitivity than CW-DCS methods. Therefore, TD-DCS requires a pulsed lasers and a TCSPC (or time-gating) module, which increases cost. To reduce the cost, Moka et al. (2022) proposed FD-DCS. A faster acquisition speed can be achieved using FD-DCS as BF and oxygenation information is implicit in the collected data. This can be a good solution for some traditional DOS and DCS systems. Moreover, implementing FD-DCS is simplified using an intensity-modulated coherence laser, which can be cost-effective.

Indeed, large arrays comprising thousands of SPADs equipped either with in-pixel Time-to-Digital Converters (TDCs) (Villa et al., 2014; Villa et al., 2012; Gersbach et al., 2012) or with a set of TDCs shared across various pixels (Jahromi et al., 2015; Charbon, 2014) are being developed in cost-effective CMOS process. Despite recent advances in SPAD technologies, state-of-the-art TD-DCS has not yet been implemented using TCSPC techniques based on TDC techniques (Wang et al., 2024; Wang et al., 2023). There is no doubt that large SPAD arrays with embedded TCSPC can be a parallelizable solution for next-generation TD-DCS, with a potential breakthrough in the SNR of the measurements and the depth-encoding. We expect this kind of TD-DCS system to be released in the coming years.

Combining DCS and DRS (Munk et al., 2012; Shang et al., 2009; Cheung et al., 2001) for concurrent BF and oxygenation measurements is also a trend. Quantifying blood oxygenation, metabolism, and tissue BF is essential for the diagnosis and therapeutic assessments of vascular/cellular diseases (Barth et al., 2010; Caprara and Grimm, 2012; Edul et al., 2011; Schober and Schwarte, 2012; White et al., 2012; Wolf et al., 2003). However, most relevant instruments assess tissue hemodynamics and metabolism by employing optical probes in direct contact with tissue surfaces. Contact measurements pose notable challenges, such as an elevated risk of infection in ulcerous tissues and potential deformation of delicate tissues (e.g., breasts and muscles) due to probe-tissue contact. This deformation can lead to distortions in the measured tissue properties. Thus, noncontact probes have been designed for deep tissues (Lin et al., 2012; Cheung et al., 2001; Yu et al., 2005).

Regarding data processing, traditional nonlinear fitting methods are usually based on analytical models (homogenous semi-infinite one-(Boas et al., 2016), two-Wu et al., 2022; Gagnon et al., 2008a), and three- layer (Li et al., 2005; Verdecchia et al., 2016; Zhao et al., 2021; Li et al., 2017) models). However, they are computationally demanding and less accurate as the SNR decreases, especially for multi-layer fitting (Wang et al., 2024). Deep learning methods have been proposed in DCS analysis since 2019(Zhang et al., 2019), including 2DCNN (Poon et al., 2020), LSTM (Nakabayashi et al., 2023; Li et al., 2021), ConvGRU (Feng et al., 2023), and DCS-NET (Wang et al., 2024). New AI techniques will be introduced to DCS applications soon.

Over the past 25 years, we have witnessed the emergence of DCS to quantify BF dynamics of deep tissues more accurately with a higher SNR. We expect low-cost, user-friendly DCS technologies will be introduced and applied soon. Combining NIRS with DCS will provide a better solution for critical bottlenecks in neuroscience and clinical applications. Although the speckle contrast optical spectroscopy (SCOS) setup, particularly the fiber-based configuration, is similar to that of DCS, SCOS can achieve a much higher SNR at a reduced cost (using inexpensive detectors). Recent studies (Zilpelwar et al., 2022; Robinson et al., 2024; Kim et al., 2023; Cheng et al., 2024) from Boas's research group have used SCOS for measuring human brain functions at a larger ρ, demonstrating greater sensitivity to CBF, suggesting that SCOS could provide an alternative approach to functional neuroimaging for cognitive neuroscience applications.

Funding

This work has been funded by the Engineering and Physical Science Research Council (Grant No. EP/T00097X/1): the Quantum Technology Hub in Quantum Imaging (QuantIC) and the University of Strathclyde.

CRediT authorship contribution statement

Quan Wang: Writing – review & editing, Writing – original draft, Visualization, Validation, Supervision, Software, Methodology, Formal analysis, Data curation, Conceptualization. **Mingliang Pan:** Writing – review & editing, Writing – original draft, Visualization, Validation, Software. **Lucas Kreiss:** Writing – review & editing, Writing – original draft, Visualization, Validation, Software. **Saeed Samaei:** Writing – review & editing, Writing – original draft, Visualization, Validation, Software. **Stefan A. Carp:** Writing – review & editing, Writing – original draft, Visualization, Validation, Supervision, Resources. **Johannes D. Johansson:** Writing – review & editing, Writing – original draft, Visualization, Validation, Supervision. **Yuanzhe Zhang:** Writing – review & editing, Writing – original draft, Visualization, Validation. **Melissa Wu:** Writing – review & editing, Writing – original draft, Visualization, Validation. **Roarke Horstmeyer:** Writing – review & editing, Writing – original draft, Supervision, Resources. **Mamadou Diop:** Writing – review & editing, Writing – original draft, Visualization, Validation,

Supervision, Resources. **David Day-Uei Li:** Writing – review & editing, Writing – original draft, Visualization, Validation, Supervision, Resources, Project administration, Investigation, Funding acquisition, Conceptualization.

Declaration of competing interest

The authors declare no conflicts of interest.

Data availability

Data will be made available on request.

Acknowledgments

We thank Professor David A. Boas from the Department of Biomedical Engineering at Boston University for his invaluable insights and contributions. We also thank Professor Robert Henderson from the School of Engineering at the University of Edinburgh for supporting us with SPAD sensors. Furthermore, special thanks to Dr. Wenhui Liu from the Yangtze Delta Region Academy, Beijing Institute of Technology, Jiaxing, for the insightful discussions.

Appendix 1. Optical-based blood flow monitoring modalities

The tree diagram in Fig. 18 shows the optical-based blood flow monitoring modalities, including LSCI (Briers et al., 2013), LDF (Fredriksson et al., 2007; Vo-Dinh, 2014), DCS, SCOS, and DSCA (Bi et al., 2013b; Bi et al., 2013a; Bi et al., 2020), all sharing the advantage of non-invasive measurement of blood flow using non-ionizing radiation. Goodman developed the fundamental principles linking temporal statistics of fluctuations in laser speckle patterns in the 1960s (Goodman, 1975). In the 1970s, the study of time-varying speckles, induced by motion, emerged as a focal point for research. LSCI is an excellent BF imaging technique that transforms a featureless laser speckle image of a tissue surface into a high-contrast BF image, but it is only suitable for shallow-depth tissue. DSCA methodology has drawn heavily from concepts in LSCI, focusing primarily on measuring average values rather than imaging BF. Consequently, advances in LSCI can be readily implemented in DSCA with minimal difficulty. After two original papers were published by Bi et al. (2013b), Bi et al. (2013a), Bi et al., (2015), DSCA has been extensively studied theoretically (Liu et al., 2014; Liu et al., 2017; Liu et al., 2017) and experimentally (Yeo et al., 2017; Yeo et al., 2016; Choo et al., 2022). DSCA can be categorized into spatial DSCA and temporal DSCA depending on how the statistics are applied when calculating speckle contrast. LDF relies on measuring the Doppler shift caused by moving red blood cells to the illuminating coherent light. Since its introduction to the commercial market in the early 1980s, it has maintained a modest yet consistent and progressively expanding presence (Rajan et al., 2009; Humeau et al., 2007). SCOS, also known as DSCA, was initially introduced in Valdes (Valdes et al., 2014) *et al.*'s study. In the research conducted by Kim et al. (2023), they confirmed that SCOS outperforms DCS, delivering over a 10-fold improvement in SNR at a comparable cost. Notably, fiber-based SCOS offers a viable avenue for functional neuroimaging in cognitive neuroscience and health science domains. Unlike techniques like LDF and LSCI, designed for superficial tissue measurement, DCS is a deep-tissue blood flow monitoring modality. Initially employing a continuous wave laser source, known as CW-DCS, various approaches have since been developed, including heterodyne/interferometric, multi-speckle, time-domain, long-wavelength, and Fourier-domain methods. Readers are encouraged to consult the review papers from Carp et al. (2023), and James and Munro (2023) to delve into the detailed comparisons among these approaches.

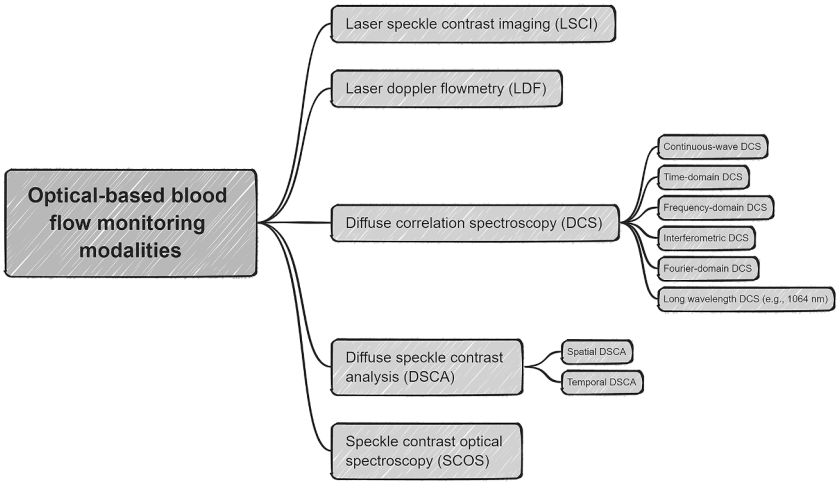

Fig. 18. Optics-based blood flow monitoring modalities, including laser speckle contrast imaging (LSCI), laser doppler flowmetry (LDF), diffuse correlation spectroscopy (DCS), diffuse speckle contrast analysis (DSCA)/speckle contrast optical spectroscopy (SCOS).

Appendix 2. Other novel representative DCS instruments

We present additional novel representative DCS instrument diagrams not previously shown. Fig. 19(a) depicts the optimized functional TD-DCS system (Ozana et al., 2022), which integrates a custom 1064 nm pulse-shaped, quasi transform-limited, amplified laser source with a high-resolution time-tagging system and SNSPD sensors. Fig. 19(b) illustrates the setup of functional interferometric diffuse wave (Zhou et al., 2021), with the interferometer detection path depicted in horizontal and vertical views. Fig. 19(c) showcases a Fourier domain implementation of the off-axis heterodyne parallel speckle detection instrument (James and Powell, 2020). Fig. 19(d) is the schematic of the fiber-based SCOS setup and the corresponding data analysis pipeline (Kim et al., 2023).

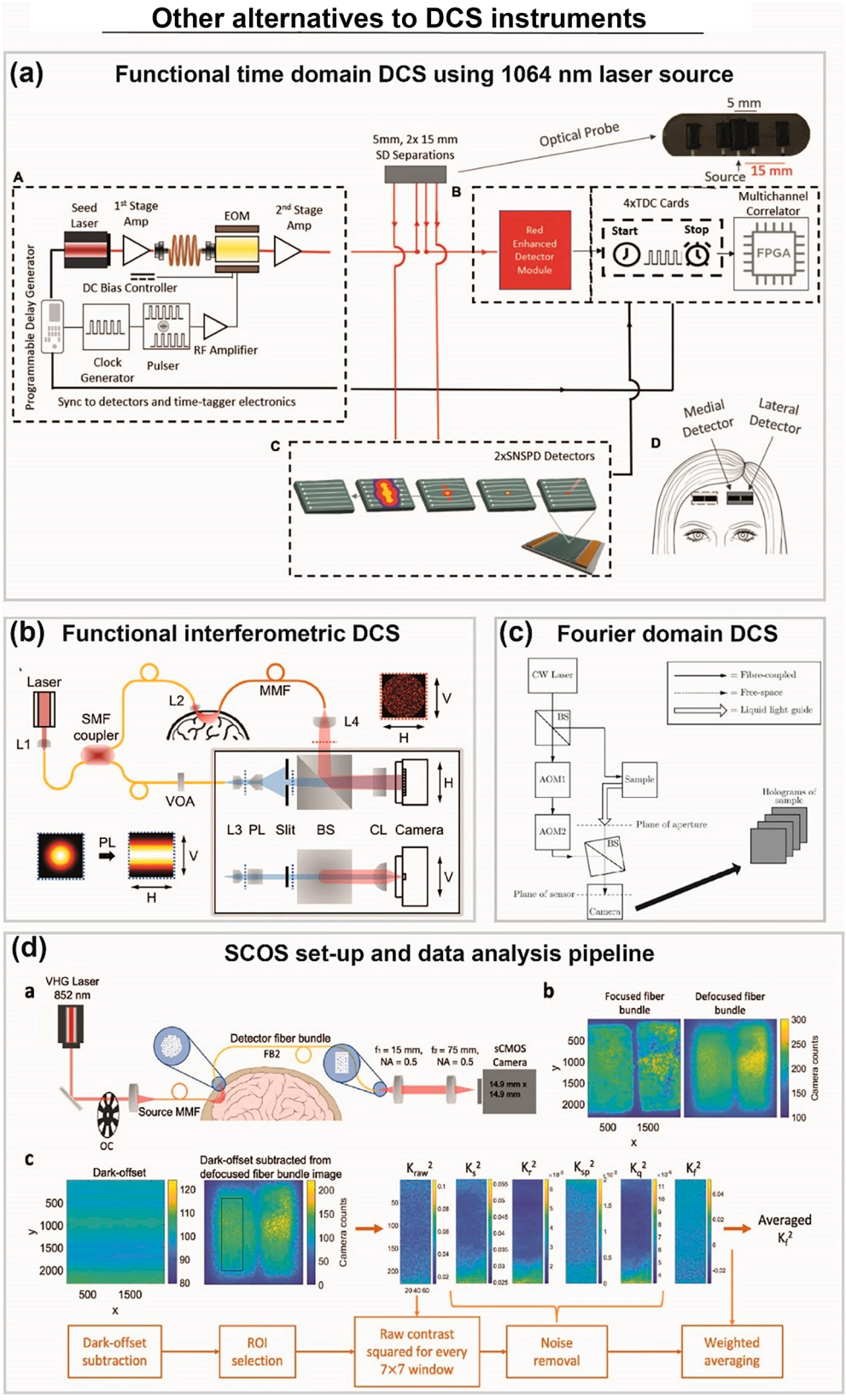

Fig. 19. (a) Schematic diagram of functional TD-DCS at 1064 nm; the figure adopted from Ref. Ozana et al. (2022). (b) Schematic of functional interferometric DWS; the figure adopted from Ref. Zhou et al. (2021). (c) Schematic of the off-axis heterodyne parallel speckle detection (the Fourier-domain approach); the figure adopted from Ref. James and Powell (2020). (d) The schematic of the fiber-based SCOS set-up and the corresponding data analysis pipeline (Kim et al., 2023).

Appendix 3. Correlation between acquisition time and spatial resolution across various BFi measurement modalities

Fig. 20 illustrates the correlation between acquisition time and spatial resolution across various BFi measurement modalities. Although DCS does not have a high spatial resolution, it outperforms others regarding acquisition speed.

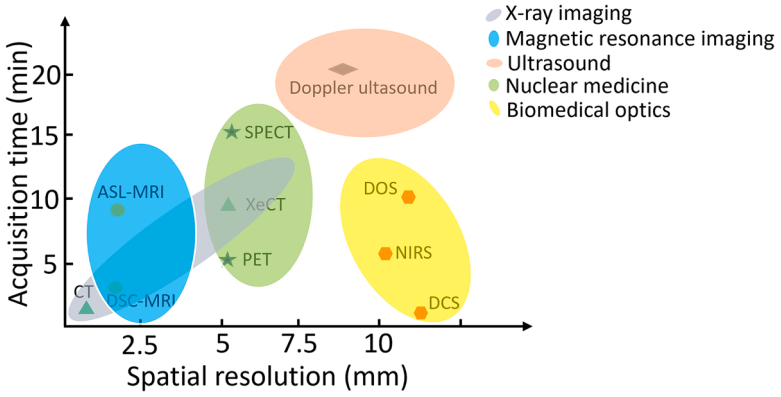

Fig. 20. Available techniques for measuring CBF in terms of the spatial resolution and acquisition time. (Note: SPECT: single photon emission computed tomography; PET: positron emission tomography; CT: computed tomography; DSC-MRI: dynamic susceptibility contrasts magnetic resonance imaging; ASL: arterial spin labeling; TCD: transcranial Doppler; TDF: thermal diffusion flowmetry; LDF: laser Doppler flowmetry; DCS: diffuse correlation spectroscopy; NIRS: near-infrared spectroscopy; CHS: coherent hemodynamics spectroscopy).

Appendix 4. DCS simulation tools

The Monte Carlo (MC) method for simulating light propagation through tissue is a benchmark technique (Wang et al., 1995), extensively discussed in Zhu and Liu's review paper (Zhu and Liu, 2013). MC has been widely used in the NIRS and DCS communities. To aid researchers in performing and documenting more intricate experimental analyses, various analysis platforms and specialized software tools (Hernandez and Pollonini, 2020; Zhao et al., 2021) have been created. The exhaustive NIRS/DCS MC software tools are listed in another review paper (Ayaz et al., 2022). Here, we only list the tools commonly used in DCS, as shown in Table 6. MCML, developed by Jacques (1989), is a steady-state MC tool for analyzing multi-layered turbid media using an infinitely narrow photon beam as the light source. Operating in a 3D environment, it provides outputs including the radial position, angular dependence of local reflectance and transmittance, and the internal distribution of energy deposition and fluence rate within the multilayered medium. The program can be easily modified. Alternative software packages like Monte Carlo eXtreme (MCX) (Fang and Boas, 2009) or mesh-based Monte Carlo (MMC) (Fang, 2010), developed by Fang and his colleagues, can simulate arbitrary optode placements on diverse, intricate tissue models with heterogeneity. MCX and MMC can record the path lengths and momentum transfer from the detected photons to obtain the electric field autocorrelation function (Wang et al., 2024; Boas et al., 2016). ScatterBrains, developed by Wu et al. (2023), is an open database of human head models with companion optode locations of interest and a toolkit designed for generating specifications to execute MC simulations of light propagation, including the code to create input files compatible with MMC. Additionally, an illustration of post-processing techniques for DCS is provided.

Table 6
Existing software tools related to DCS.

Name	Language	Website
MCML (Wang and Jacques, 1995)	Standalone	https://omlc.org/software/mc/
MMC (Fang, 2010)	Standalone/Matlab	http://mcx.space/#mmc
MCX (Fang and Boas, 2009)	Standalone/Matlab	http://mcx.space/
scatterBrains (Wu et al., 2023)	Matlab	https://github.com/wumelissa/scatterBrains

References

ANS Institute, 2007. American National Standard for Safe Use of Lasers. Laser Institute of Aemerica.

Ackerson, B.J., et al., 1992. Correlation transfer - Application of radiative transfer solution methods to photon correlation problems. J. Thermophys. Heat Transf. 6 (4), 577–588. https://doi.org/10.2514/3.11537.

https://www.alvgmbh.de/Products/Correlators/Discontinued_Models_/ALV-5000_EPP/alv-5000_epp.html, 2024.

ANS Institute, 2007. American National Standard for Safe Use of Lasers. Laser Institute of America.

Ayaz, H., et al., 2022. Optical imaging and spectroscopy for the study of the human brain: status report. Neurophotonics 9 (S2). https://doi.org/10.1117/1.NPh.9.S2.S24001.

Baker, W.B., et al., 2014. Modified Beer-Lambert law for blood flow. Biomed. Opt. Express 5 (11), 4053. https://doi.org/10.1364/BOE.5.004053.

Baker, W.B., et al., 2015. Pressure modulation algorithm to separate cerebral hemodynamic signals from extracerebral artifacts. Neurophotonics 2 (3), 035004. https://doi.org/10.1117/1.NPh.2.3.035004.

Bangalore-Yogananda, C.G., et al., 2018. Concurrent measurement of skeletal muscle blood flow during exercise with diffuse correlation spectroscopy and Doppler ultrasound. Biomed. Opt. Express 9 (1), 131. https://doi.org/10.1364/BOE.9.000131.

Barbier, E.L., Lamalle, L., Décorps, M., 2001. Methodology of brain perfusion imaging: methodology of brain perfusion imaging. J. Magn. Reson. Imaging 13 (4), 496–520. https://doi.org/10.1002/jmri.1073.

Barth, M., et al., 2010. Correlation of clinical outcome with pressure-, oxygen-, and flow-related indices of cerebrovascular reactivity in patients following aneurysmal SAH. Neurocrit. Care 12 (2), 234–243. https://doi.org/10.1007/s12028-009-9287-8.

Becker, W., et al., 2004. Advanced time-correlated single photon counting techniques for spectroscopy and imaging in biomedical systems. In: Proceedings of the Lasers and Applications in Science and Engineering. San Jose, Ca, p. 104. https://doi.org/10.1117/12.529143, 1 June.

https://www.becker-hickl.com/applications/dcs-diffuse-correlation/, 2024.

Belau, M., et al., 2010. Noninvasive observation of skeletal muscle contraction using near-infrared time-resolved reflectance and diffusing-wave spectroscopy. J. Biomed. Opt. 15 (5), 057007 https://doi.org/10.1117/1.3503398.

Bellini, T., et al., 1991. Effects of finite laser coherence in quasielastic multiple scattering. Phys. Rev. A 44 (8), 5215–5223. https://doi.org/10.1103/PhysRevA.44.5215.
Benaron, D.A., et al., 1992. Noninvasive methods for estimating *in vivo* oxygenation. Clin. Pediatr. 31 (5), 258–273. https://doi.org/10.1177/000992289203100501 (Phila).
Berne, B.J., Pecora, R., 1990. Dynamic Light Scattering with Applications to Chemistry, Biology, and Physics. Krieger, New York, NY.
Berne, B.J., Pecora, R., 2000. Dynamic Light Scattering: With Applications to Chemistry, Biology, and Physics. Courier Corporation.
Bi, R., Dong, J., Lee, K., 2013a. Deep tissue flowmetry based on diffuse speckle contrast analysis. Opt. Lett. 38 (9), 1401. https://doi.org/10.1364/OL.38.001401.
Bi, R., Dong, J., Lee, K., 2013b. Multi-channel deep tissue flowmetry based on temporal diffuse speckle contrast analysis. Opt. Express 21 (19), 22854. https://doi.org/10.1364/OE.21.022854.
Bi, R., et al., 2015. Optical methods for blood perfusion measurement—theoretical comparison among four different modalities. J. Opt. Soc. Am. A 32 (5), 860. https://doi.org/10.1364/JOSAA.32.000860.
Bi, R., Du, Y., Singh, G., Ho, C.J., Zhang, S., Attia, A.B.E., Li, X., Olivo, M., 2020. Fast pulsatile blood flow measurement in deep tissue through a multimode detection fiber. J. Biomed. Opt. 25 (5), 1–10. https://doi.org/10.1117/1.JBO.25.5.055003.
Bi, R., Zhang, R., Meng, L., Du, Y., Low, J., Qi, Y., Rajarahm, P., Lai, A.Y.F., Tan, V.S.Y., Ho, P., Olivo, M., 2024. A portable optical pulsatile flowmetry demonstrates strong clinical relevance for diabetic foot perfusion assessment. APL Bioeng. 8 (1), 016109 https://doi.org/10.1063/5.0182670.
Bigio, I.J., Fantini, S., 2016. Quantitative Biomedical Optics: Theory, Methods, and Applications. Cambridge University Press.
Biswas, A., et al., 2021. Fast diffuse correlation spectroscopy with a low-cost, fiber-less embedded diode laser. Biomed. Opt. Express 12 (11), 6686. https://doi.org/10.1364/BOE.435136.
Boas, D.A., Yodh, A.G., 1997. Spatially varying dynamical properties of turbid media probed with diffusing temporal light correlation. J. Opt. Soc. Am. A 14 (1), 192. https://doi.org/10.1364/JOSAA.14.000192.
Boas, D.A., Campbell, L.E., Yodh, A.G., 1995. Scattering and imaging with diffusing temporal field correlations. Phys. Rev. Lett. 75 (9), 1855–1858. https://doi.org/10.1103/PhysRevLett.75.1855.
Boas, D.A., et al., 1996. Diffusion of temporal field correlation with selected applications. In: Proceedings of the CIS Selected Papers: Coherence Domain Methods in Biomedical Optics. Saratov, Russia, pp. 34–46. https://doi.org/10.1117/12.231685, 9 February.
Boas, D.A., et al., 2016. Establishing the diffuse correlation spectroscopy signal relationship with blood flow. Neurophotonics 3 (3), 031412. https://doi.org/10.1117/1.NPh.3.3.031412.
Boas D.A., 1996. Diffuse photon probes of structural and dynamical properties of turbid media: theory and biomedical application. PhD thesis. University of Pennsylvania.
Borycki, D., Kholiqov, O., Srinivasan, V.J., 2017. Reflectance-mode interferometric near-infrared spectroscopy quantifies brain absorption, scattering, and blood flow index *in vivo*. Opt. Lett. 42 (3), 591. https://doi.org/10.1364/OL.42.000591.
Briers, D., et al., 2013. Laser speckle contrast imaging: theoretical and practical limitations. J. Biomed. Opt. 18 (6), 066018 https://doi.org/10.1117/1.JBO.18.6.066018.
Bruschini, C., et al., 2019. Single-photon avalanche diode imagers in biophotonics: review and outlook. Light Sci. Appl. 8 (1), 87. https://doi.org/10.1038/s41377-019-0191-5.
Buckley, E.M., et al., 2009. Cerebral hemodynamics in preterm infants during positional intervention measured with diffuse correlation spectroscopy and transcranial Doppler ultrasound. Opt. Express OE 17 (15), 12571–12581. https://doi.org/10.1364/OE.17.012571.
Buckley, E.M., et al., 2013. Early postoperative changes in cerebral oxygen metabolism following neonatal cardiac surgery: effects of surgical duration. J. Thorac. Cardiovasc. Surg. 145 (1), 196–205. https://doi.org/10.1016/j.jtcvs.2012.09.057 e1.
Buckley, E.M., et al., 2014. Diffuse correlation spectroscopy for measurement of cerebral blood flow: future prospects. Neurophotonics 1 (1), 011009. https://doi.org/10.1117/1.NPh.1.1.011009.
Busch, T.M., et al., 2009. Fluence rate-dependent intratumor heterogeneity in physiologic and cytotoxic responses to Photofrin photodynamic therapy. Photochem. Photobiol. Sci. 8 (12), 1683–1693. https://doi.org/10.1039/b9pp00004f.
Busch, D.R., et al., 2016. Cerebral blood flow response to hypercapnia in children with obstructive sleep apnea syndrome. Sleep 39 (1), 209–216. https://doi.org/10.5665/sleep.5350.
Campbell, B.C., et al., 2013. Failure of collateral blood flow is associated with infarct growth in ischemic stroke. J. Cereb. Blood Flow Metab. 33 (8), 1168–1172. https://doi.org/10.1038/jcbfm.2013.77.
Caprara, C., Grimm, C., 2012. From oxygen to erythropoietin: relevance of hypoxia for retinal development, health and disease. Prog. Retin. Eye Res. 31 (1), 89–119. https://doi.org/10.1016/j.preteyeres.2011.11.003.
Carp, S.A., et al., 2010. Validation of diffuse correlation spectroscopy measurements of rodent cerebral blood flow with simultaneous arterial spin labeling MRI; towards MRI-optical continuous cerebral metabolic monitoring. Biomed. Opt. Express 1 (2), 553. https://doi.org/10.1364/BOE.1.000553.
Carp, S.A., et al., 2017. Combined multi-distance frequency domain and diffuse correlation spectroscopy system with simultaneous data acquisition and real-time analysis. Biomed. Opt. Express 8 (9), 3993. https://doi.org/10.1364/BOE.8.003993.
Carp, S.A., et al., 2020. Diffuse correlation spectroscopy measurements of blood flow using 1064 nm light. J. Biomed. Opt. 25 (09) https://doi.org/10.1117/1.JBO.25.9.097003.
Carp, S.A., Robinson, M.B., Franceschini, M.A., 2023. Diffuse correlation spectroscopy: current status and future outlook. Neurophotonics 10 (01). https://doi.org/10.1117/1.NPh.10.1.013509.
Charbon, E., 2014. Single-photon imaging in complementary metal oxide semiconductor processes. Philos. Trans. R. Soc. A 372 (2012), 20130100. https://doi.org/10.1098/rsta.2013.0100.
Cheng, R., et al., 2012. Noninvasive optical evaluation of spontaneous low frequency oscillations in cerebral hemodynamics. NeuroImage 62 (3), 1445–1454. https://doi.org/10.1016/j.neuroimage.2012.05.069.
Cheng, X., et al., 2018. Time domain diffuse correlation spectroscopy: modeling the effects of laser coherence length and instrument response function. Opt. Lett. 43 (12), 2756. https://doi.org/10.1364/OL.43.002756.
Cheng, X., et al., 2021. Measuring neuronal activity with diffuse correlation spectroscopy: a theoretical investigation. Neurophotonics 8 (03). https://doi.org/10.1117/1.NPh.8.3.035004.
Cheng, T.Y., et al., 2024. Choosing a camera and optimizing system parameters for speckle contrast optical spectroscopy. Sci. Rep. 14 (1), 11915. https://doi.org/10.1038/s41598-024-62106-y.
Cheung, C., et al., 2001. *In vivo* cerebrovascular measurement combining diffuse near-infrared absorption and correlation spectroscopies. Phys. Med. Biol. 46 (8), 2053–2065. https://doi.org/10.1088/0031-9155/46/8/302.
Ching, T., et al., 2018. Opportunities and obstacles for deep learning in biology and medicine. J. R. Soc. Interface 15 (141), 20170387. https://doi.org/10.1098/rsif.2017.0387.
Choe, R., Durduran, T., 2012. Diffuse optical monitoring of the neoadjuvant breast cancer therapy. IEEE J. Sel. Top. Quantum Electron. 18 (4), 1367–1386. https://doi.org/10.1109/JSTQE.2011.2177963.
Choe, R., et al., 2014. Optically measured microvascular blood flow contrast of malignant breast tumors. PLoS ONE 9 (6), e99683. https://doi.org/10.1371/journal.pone.0099683. J. Najbauer, Ed.
Choo, T.W.J., Zhang, R., Bi, R., Olivo, M., 2022. Experimental characterization of diffuse speckle pulsatile flowmetry system. Front. Phys. 10, 1006484. https://doi.org/10.3389/fphy.2022.1006484.
Chu, B., 1991. Laser Light Scattering: Basic Principles and Practice. Academic Press, New York, NY.
Chung, S.H., et al., 2015. Macroscopic optical physiological parameters correlate with microscopic proliferation and vessel area breast cancer signatures. Breast Cancer Res. 17 (1), 72. https://doi.org/10.1186/s13058-015-0578-z.
Cipelletti, L., Weitz, D.A., 1999. Ultralow-angle dynamic light scattering with a charge coupled device camera based multispeckle, multitau correlator. Rev. Sci. Instrum. 70 (8), 3214–3221. https://doi.org/10.1063/1.1149894.
Clark, N.A., Lunacek, J.H., Benedek, G.B., 1970. A study of brownian motion using light scattering. Am. J. Phys. 38 (5), 575–585.
Colombo, L., et al., 2019. Effects of the instrument response function and the gate width in time-domain diffuse correlation spectroscopy: model and validations. Neurophotonics 6 (03), 1. https://doi.org/10.1117/1.NPh.6.3.035001.
Colombo, L., et al., 2020. *In vivo* time-domain diffuse correlation spectroscopy above the water absorption peak. Opt. Lett. 45 (13), 3377. https://doi.org/10.1364/OL.392355.
Colombo, L., et al., 2020. Coherent fluctuations in time-domain diffuse optics. APL Photonics 5 (7), 071301. https://doi.org/10.1063/5.0011838.
Cortese, L., et al., 2021. Recipes for diffuse correlation spectroscopy instrument design using commonly utilized hardware based on targets for signal-to-noise ratio and precision. Biomed. Opt. Express 12 (6), 3265. https://doi.org/10.1364/BOE.423071.
Cowdrick, K.R., et al., 2023. Agreement in cerebrovascular reactivity assessed with diffuse correlation spectroscopy across experimental paradigms improves with short separation regression. Neurophotonics 10 (2), 025002. https://doi.org/10.1117/1.NPh.10.2.025002.
Cowdrick, K.R., et al., 2023. Agreement in cerebrovascular reactivity assessed with diffuse correlation spectroscopy across experimental paradigms improves with short separation regression. Neurophotonics 10 (02). https://doi.org/10.1117/1.NPh.10.2.025002.
Cowdrick, K.R., et al., 2023. Impaired cerebrovascular reactivity in pediatric sickle cell disease using diffuse correlation spectroscopy. Biomed. Opt. Express 14 (11), 5696. https://doi.org/10.1364/BOE.499274.
Culver, J.P., et al., 2003. Diffuse optical tomography of cerebral blood flow, oxygenation, and metabolism in rat during focal ischemia. J. Cereb. Blood Flow Metab. 23 (8), 911–924. https://doi.org/10.1097/01.WCB.0000076703.71231.BB.
Danen, R.M., et al., 1998. Regional imager for low-resolution functional imaging of the brain with diffusing near-infrared light. Photochem. Photobiol. 67 (1), 33–40. https://doi.org/10.1111/j.1751-1097.1998.tb05162.x.
Dechter, R., 1986. Learning while searching in constraint-satisfaction-problems. In: Proceedings of the Fifth AAAI National Conference on Artificial Intelligence. Philadelphia, Pennsylvania. AAAI Press, pp. 178–183.
Dehaes, M., et al., 2014. Cerebral oxygen metabolism in neonatal hypoxic ischemic encephalopathy during and after therapeutic hypothermia. J. Cereb. Blood Flow Metab. 34 (1), 87–94. https://doi.org/10.1038/jcbfm.2013.165.
Delpy, D.T., et al., 1988. Estimation of optical pathlength through tissue from direct time of flight measurement. Phys. Med. Biol. 33 (12), 1433–1442. https://doi.org/10.1088/0031-9155/33/12/008.
Devor, A., et al., 2012. Frontiers in optical imaging of cerebral blood flow and metabolism. J. Cereb. Blood Flow Metab. 32 (7), 1259–1276. https://doi.org/10.1038/jcbfm.2011.195.

Dietsche, G., et al., 2007. Fiber-based multispeckle detection for time-resolved diffusing-wave spectroscopy: characterization and application to blood flow detection in deep tissue. Appl. Opt. 46 (35), 8506. https://doi.org/10.1364/AO.46.008506.
Diop, M., et al., 2010. Time-resolved near-infrared technique for bedside monitoring of absolute cerebral blood flow. In: Proceedings of the Advanced Biomedical and Clinical Diagnostic Systems VIII. SPIE, pp. 115–123. https://doi.org/10.1117/12.842521, 7555.
Diop, M., et al., 2010. Comparison of time-resolved and continuous-wave near-infrared techniques for measuring cerebral blood flow in piglets. JBO 15 (5), 057004. https://doi.org/10.1117/1.3488626.
Diop, M., et al., 2011. Calibration of diffuse correlation spectroscopy with a time-resolved near-infrared technique to yield absolute cerebral blood flow measurements. Biomed. Opt. Express 2 (7), 2068. https://doi.org/10.1364/BOE.2.002068.
Dong, J., et al., 2012. Diffuse correlation spectroscopy with a fast Fourier transform-based software autocorrelator. J. Biomed. Opt. 17 (9), 0970041 https://doi.org/10.1117/1.JBO.17.9.097004.
Dong, L., et al., 2012. Noninvasive diffuse optical monitoring of head and neck tumor blood flow and oxygenation during radiation delivery. Biomed. Opt. Express 3 (2), 259. https://doi.org/10.1364/BOE.3.000259.
Dong, L., et al., 2013. Simultaneously extracting multiple parameters via fitting one single autocorrelation function curve in diffuse correlation spectroscopy. IEEE Trans. Biomed. Eng. 60 (2), 361–368. https://doi.org/10.1109/TBME.2012.2226885.
Dong, L., et al., 2016. Diffuse optical measurements of head and neck tumor hemodynamics for early prediction of chemoradiation therapy outcomes. J. Biomed. Opt. 21 (8), 085004 https://doi.org/10.1117/1.JBO.21.8.085004.
Dougherty, R.L., et al., 1994. Correlation transfer: development and application. J. Quant. Spectrosc. Radiat. Transf. 52 (6), 713–727. https://doi.org/10.1016/0022-4073(94)90037-X.
Duncan, A., et al., 1996. Measurement of cranial optical path length as a function of age using phase resolved near infrared spectroscopy. Pediatr. Res. 39 (5), 889–894. https://doi.org/10.1203/00006450-199605000-00025.
Durduran, T., Yodh, A.G., 2014. Diffuse correlation spectroscopy for non-invasive, micro-vascular cerebral blood flow measurement. NeuroImage 85, 51–63. https://doi.org/10.1016/j.neuroimage.2013.06.017.
Durduran, T., et al., 2004. Diffuse optical measurement of blood flow, blood oxygenation, and metabolism in a human brain during sensorimotor cortex activation. Opt. Lett. 29 (15), 1766. https://doi.org/10.1364/OL.29.001766.
Durduran, T., et al., 2005. Diffuse optical measurement of blood flow in breast tumors. Opt. Lett. 30 (21), 2915. https://doi.org/10.1364/OL.30.002915.
Durduran, T., et al., 2009. Transcranial optical monitoring of cerebrovascular hemodynamics in acute stroke patients. Opt. Express 17 (5), 3884. https://doi.org/10.1364/OE.17.003884.
Durduran, T., et al., 2010. Optical measurement of cerebral hemodynamics and oxygen metabolism in neonates with congenital heart defects. J. Biomed. Opt. 15 (3), 037004 https://doi.org/10.1117/1.3425884.
Durduran, T., et al., 2010. Diffuse optics for tissue monitoring and tomography. Rep. Prog. Phys. 73 (7), 076701 https://doi.org/10.1088/0034-4885/73/7/076701.
Durduran, T., 2004. Noninvasive measurements of tissue hemodynamics with hybrid diffuse optical methods. Med. Phys. 31 (7), 2178. https://doi.org/10.1118/1.1763412. –2178.
Edlow, B.L., et al., 2010. The effects of healthy aging on cerebral hemodynamic responses to posture change. Physiol. Meas. 31 (4), 477–495. https://doi.org/10.1088/0967-3334/31/4/002.
Edul, V., Dubin, A., Ince, C., 2011. The microcirculation as a therapeutic target in the treatment of sepsis and shock. Semin. Respir. Crit. Care Med. 32 (05), 558–568. https://doi.org/10.1055/s-0031-1287864.
Esmaeil Zadeh, I., et al., 2021. Superconducting nanowire single-photon detectors: a perspective on evolution, state-of-the-art, future developments, and applications. Appl. Phys. Lett. 118 (19), 190502 https://doi.org/10.1063/5.0045990.
EU FP6 MEGAFRAME, https://cordis.europa.eu/project/id/029217, June 2006 - May 2009.
Fang, Q., Boas, D.A., 2009. Monte Carlo simulation of photon migration in 3D turbid media accelerated by graphics processing units. Opt. Express 17 (22), 20178. https://doi.org/10.1364/OE.17.020178.
Fang, Q., 2010. Mesh-based Monte Carlo method using fast ray-tracing in Plücker coordinates. Biomed. Opt. Express 1 (1), 165. https://doi.org/10.1364/BOE.1.000165.
Fantini, S., et al., 2016. Cerebral blood flow and autoregulation: current measurement techniques and prospects for noninvasive optical methods. Neurophotonics 3 (3), 031411. https://doi.org/10.1117/1.NPh.3.3.031411.
Farrell, T.J., Patterson, M.S., Wilson, B., 1992. A diffusion theory model of spatially resolved, steady-state diffuse reflectance for the noninvasive determination of tissue optical properties *in vivo*. Med. Phys. 19 (4), 879–888. https://doi.org/10.1118/1.596777.
Farzam, P., et al., 2017. Pre-clinical longitudinal monitoring of hemodynamic response to anti-vascular chemotherapy by hybrid diffuse optics. Biomed. Opt. Express 8 (5), 2563. https://doi.org/10.1364/BOE.8.002563.
Favilla, C.G., et al., 2014. Optical bedside monitoring of cerebral blood flow in acute ischemic stroke patients during head-of-bed manipulation. Stroke 45 (5), 1269–1274. https://doi.org/10.1161/STROKEAHA.113.004116.
Feng, J., et al., 2023. Cerebral blood flow monitoring using a ConvGRU model based on diffuse correlation spectroscopy. Infrared Phys. Technol. 129, 104541 https://doi.org/10.1016/j.infrared.2022.104541.
Ferreira, D., Bachelard, R., Guerin, W., Kaiser, R., Fouché, M., 2020. Connecting field and intensity correlations: The Siegert relation and howtotest it. Am. J. Phys. 88 (10), 831–837. https://doi.org/10.1119/10.0001630.
Forti, R.M., et al., 2023. Optimizing a two-layer method for hybrid diffuse correlation spectroscopy and frequency-domain diffuse optical spectroscopy cerebral measurements in adults. Neurophotonics 10 (02). https://doi.org/10.1117/1.NPh.10.2.025008.
Forti, R.M., et al., 2023. Non-invasive diffuse optical monitoring of cerebral physiology in an adult swine-model of impact traumatic brain injury. Biomed. Opt. Express 14 (6), 2432. https://doi.org/10.1364/BOE.486363.
Fredriksson, I., Fors, C., Johansson, J., 2007. Laser Doppler flowmetry - a theoretical frame work. https://api.semanticscholar.org/. Corpus ID: 15815850.
Freund, I., Goodman, J.W., 2007. Speckle Phenomena in Optics: Theory and Applications, 130. Roberts & Company, pp. 413–414. https://doi.org/10.1007/s10955-007-9440-8 (Englewood, Colorado), 2007," J Stat Phys.
Fuller, G.G., et al., 1980. The measurement of velocity gradients in laminar flow by homodyne light-scattering spectroscopy. J. Fluid Mech. 100 (03), 555. https://doi.org/10.1017/S0022112080001280.
Gagnon, L., et al., 2008a. Investigation of diffuse correlation spectroscopy in multi-layered media including the human head. Opt. Express 16 (20), 15514. https://doi.org/10.1364/OE.16.015514.
Gagnon, L., et al., 2008b. Double-layer estimation of intra- and extracerebral hemoglobin concentration with a time-resolved system. J. Biomed. Opt. 13 (5), 054019 https://doi.org/10.1117/1.2982524.
Gersbach, M., et al., 2012. A time-resolved, low-noise single-photon image sensor fabricated in deep-submicron CMOS technology. IEEE J. Solid-State Circuits 47 (6), 1394–1407. https://doi.org/10.1109/JSSC.2012.2188466.
Goodman, J.W., 1975. Statistical properties of laser speckle patterns. Laser Speckle and Related Phenomena. Springer, Berlin, Heidelberg, pp. 9–75. https://doi.org/10.1007/978-3-662-43205-1_2. J. C. Dainty, Ed.
Grosenick, D., et al., 2016. Review of optical breast imaging and spectroscopy. J. Biomed. Opt. 21 (9), 091311 https://doi.org/10.1117/1.JBO.21.9.091311.
Gurley, K., Yu, G., 2013. Diffuse correlation spectroscopy (DCS) for assessment of tissue blood flow in skeletal muscle: recent progress. Anat. Physiol. 03 (02) https://doi.org/10.4172/2161-0940.1000128.
Gurley, K., Shang, Y., Yu, G., 2012. Noninvasive optical quantification of absolute blood flow, blood oxygenation, and oxygen consumption rate in exercising skeletal muscle. J. Biomed. Opt. 17 (7), 0750101 https://doi.org/10.1117/1.JBO.17.7.075010.
Habazettl, H., et al., 2010. Near-infrared spectroscopy and indocyanine green derived blood flow index for noninvasive measurement of muscle perfusion during exercise. J. Appl. Physiol. 108.
Han, S., et al., 2015. Non-invasive monitoring of temporal and spatial blood flow during bone graft healing using diffuse correlation spectroscopy. PLoS ONE 10 (12), e0143891. J. Cray, Ed. 10.1371/journal.pone.0143891.
Han, S., et al., 2016. Non-invasive diffuse correlation tomography reveals spatial and temporal blood flow differences in murine bone grafting approaches. Biomed. Opt. Express 7 (9), 3262. https://doi.org/10.1364/BOE.7.003262.
Hawrysz, D.J., Sevick-Muraca, E.M., 2000. Developments toward diagnostic breast cancer imaging using near-infrared optical measurements and fluorescent contrast agents1. Neoplasia 2 (5), 388–417. https://doi.org/10.1038/sj.neo.7900118.
He, L., et al., 2013. Using optical fibers with different modes to improve the signal-to-noise ratio of diffuse correlation spectroscopy flow-oximeter measurements. J. Biomed. Opt. 18 (3), 037001 https://doi.org/10.1117/1.JBO.18.3.037001.
He, L., et al., 2015. Noncontact diffuse correlation tomography of human breast tumor. J. Biomed. Opt. 20 (8), 086003 https://doi.org/10.1117/1.JBO.20.8.086003.
Helton, M., et al., 2023. Numerical approach to quantify depth-dependent blood flow changes in real-time using the diffusion equation with continuous-wave and time-domain diffuse correlation spectroscopy. Biomed. Opt. Express 14 (1), 367. https://doi.org/10.1364/BOE.469419.
Henry, B., et al., 2015. Hybrid diffuse optical techniques for continuous hemodynamic measurement in gastrocnemius during plantar flexion exercise. J. Biomed. Opt. 20 (12), 125006 https://doi.org/10.1117/1.JBO.20.12.125006.
Hernandez, S.M., Pollonini, L., 2020. NIRSplot: a tool for quality assessment of fNIRS scans. In: Proceedings of the Biophotonics Congress: Biomedical Optics 2020 (Translational, Microscopy, OCT, OTS, BRAIN). Washington, DC. Optica Publishing Group, p. BM2C.5. https://doi.org/10.1364/BRAIN.2020.BM2C.5.
Huang, C., et al., 2016. Low-cost compact diffuse speckle contrast flowmeter using small laser diode and bare charge-coupled-device. J. Biomed. Opt. 21 (8), 080501 https://doi.org/10.1117/1.JBO.21.8.080501.
Huang, C., et al., 2021. Speckle contrast diffuse correlation tomography of cerebral blood flow in perinatal disease model of neonatal piglets. J. Biophotonics 14 (4), e202000366. https://doi.org/10.1002/jbio.202000366.
Humeau, A., et al., 2007. Laser Doppler perfusion monitoring and imaging: novel approaches. Med. Bio Eng. Comput. 45 (5), 421. https://doi.org/10.1007/s11517-007-0170-5.
Irwin, D., et al., 2011. Influences of tissue absorption and scattering on diffuse correlation spectroscopy blood flow measurements. Biomed. Opt. Express 2 (7), 1969. https://doi.org/10.1364/BOE.2.001969.
Jöbsis, F.F., 1977. Noninvasive, infrared monitoring of cerebral and myocardial oxygen sufficiency and circulatory parameters. Science 198 (4323), 1264–1267. https://doi.org/10.1126/science.929199.
Jö Bsis-Vandervliet, F.F., Jöbsis, P.D., 1999. Biochemical and physiological basis of medical near-infrared spectroscopy. J. Biomed. Opt. 4 (4), 397. https://doi.org/10.1117/1.429953.

Jö Bsis-Vandervliet, F.F., 1999. Discovery of the near-infrared window into the body and the early development of near-infrared spectroscopy. J. Biomed. Opt. 4 (4), 392. https://doi.org/10.1117/1.429952.
Jacques, S.L., 1989. Time resolved propagation of ultrashort laser pulses within turbid tissues. Appl. Opt. 28 (12), 2223. https://doi.org/10.1364/AO.28.002223.
Jahromi, S., et al., 2015. A single chip laser radar receiver with a 9×9 SPAD detector array and a 10-channel TDC. In: Proceedings of the ESSCIRC Conference 2015 - 41st European Solid-State Circuits Conference (ESSCIRC). Graz, Austria. IEEE, pp. 364–367. https://doi.org/10.1109/ESSCIRC.2015.7313903.
Jaillon, F., et al., 2007. Activity of the human visual cortex measured non-invasively by diffusing-wave spectroscopy. Opt. Express 15 (11), 6643. https://doi.org/10.1364/OE.15.006643.
James, E., Munro, P.R.T., 2023. Diffuse correlation spectroscopy: a review of recent advances in parallelisation and depth discrimination techniques. Sensors 23 (23), 9338. https://doi.org/10.3390/s23239338.
James, E., Powell, S., 2020. Fourier domain diffuse correlation spectroscopy with heterodyne holographic detection. Biomed. Opt. Express 11 (11), 6755. https://doi.org/10.1364/BOE.400525.
Johansson, J.D., et al., 2019. A multipixel diffuse correlation spectroscopy system based on a single photon avalanche diode array. J. Biophotonics 12 (11). https://doi.org/10.1002/jbio.201900091.
Johnson, T.W., et al., 2022. Cerebral blood flow hemispheric asymmetry in comatose adults receiving extracorporeal membrane oxygenation. Front. Neurosci. 16, 858404 https://doi.org/10.3389/fnins.2022.858404.
Kaiser, M.G., During, M.J., 1995. Combining laser doppler flowmetry with microdialysis: a novel approach to investigate the coupling of regional cerebral blood flow to neuronal activity. J. Neurosci. Methods 60 (1–2), 165–173. https://doi.org/10.1016/0165-0270(95)00008-I.
Kaya, K., et al., 2022. Intraoperative cerebral hemodynamic monitoring during carotid endarterectomy via diffuse correlation spectroscopy and near-infrared spectroscopy. Brain Sci. 12 (8), 1025. https://doi.org/10.3390/brainsci12081025.
Keller, E., et al., 2003. Noninvasive measurement of regional cerebral blood flow and regional cerebral blood volume by near-infrared spectroscopy and indocyanine green dye dilution. NeuroImage 20 (2), 828–839. https://doi.org/10.1016/S1053-8119(03)00315-X.
Kholiqov, O., et al., 2020. Time-of-flight resolved light field fluctuations reveal deep human tissue physiology. Nat. Commun. 11 (1), 391. https://doi.org/10.1038/s41467-019-14228-5.
Kholiqov, O., et al., 2022. Scanning interferometric near-infrared spectroscopy. Opt. Lett. 47 (1), 110. https://doi.org/10.1364/OL.443533.
Kiechl-Kohlendorfer, U., et al., 2009. Adverse neurodevelopmental outcome in preterm infants: risk factor profiles for different gestational ages. Acta Paediatr. 98 (5), 792–796. https://doi.org/10.1111/j.1651-2227.2009.01219.x.
Kienle, A., Glanzmann, T., 1999. *In vivo* determination of the optical properties of muscle with time-resolved reflectance using a layered model. Phys. Med. Biol. 44 (11), 2689–2702. https://doi.org/10.1088/0031-9155/44/11/301.
Kienle, A., Patterson, M.S., 1997. Improved solutions of the steady-state and the time-resolved diffusion equations for reflectance from a semi-infinite turbid medium. J. Opt. Soc. Am. A 14 (1), 246. https://doi.org/10.1364/JOSAA.14.000246.
Kienle, A., Patterson, M.S., 1997. Determination of the optical properties of semi-infinite turbid media from frequency-domain reflectance close to the source. Phys. Med. Biol. 42 (9), 1801–1819. https://doi.org/10.1088/0031-9155/42/9/011.
Kienle, A., et al., 1998. Investigation of two-layered turbid media with time-resolved reflectance. Appl. Opt. 37 (28), 6852. https://doi.org/10.1364/AO.37.006852.
Kienle, A., et al., 1998. Noninvasive determination of the optical properties of two-layered turbid media. Appl. Opt. 37 (4), 779. https://doi.org/10.1364/AO.37.000779.
Kim, M.N., et al., 2010. Noninvasive measurement of cerebral blood flow and blood oxygenation using near-infrared and diffuse correlation spectroscopies in critically brain-injured adults. Neurocrit. Care 12 (2), 173–180. https://doi.org/10.1007/s12028-009-9305-x.
Kim, M.N., et al., 2014. Continuous optical monitoring of cerebral hemodynamics during Head-of-Bed manipulation in brain-injured adults. Neurocrit. Care 20 (3), 443–453. https://doi.org/10.1007/s12028-013-9849-7.
Kim, B., et al., 2023. Measuring human cerebral blood flow and brain function with fiber-based speckle contrast optical spectroscopy system. Commun. Biol. 6 (1), 844. https://doi.org/10.1038/s42003-023-05211-4.
Koban, L., et al., 2010. Processing of emotional words measured simultaneously with steady-state visually evoked potentials and near-infrared diffusing-wave spectroscopy. BMC Neurosci. 11 (1), 85. https://doi.org/10.1186/1471-2202-11-85.
Koppel, D.E., 1974. Statistical accuracy in fluorescence correlation spectroscopy. Phys. Rev. A 10 (6), 1938–1945. https://doi.org/10.1103/PhysRevA.10.1938.
L. Kreiss et al., "Beneath the surface: revealing deep-tissue blood flow in human subjects with massively parallelized diffuse correlation spectroscopy," arXiv:2403.03968, arXiv (2024).
Kwong, K.K., et al., 1992. Dynamic magnetic resonance imaging of human brain activity during primary sensory stimulation. Proc. Natl. Acad. Sci. USA 89 (12), 5675–5679. https://doi.org/10.1073/pnas.89.12.5675.
Lafontant, A., et al., 2022. Comparison of optical measurements of critical closing pressure acquired before and during induced ventricular arrhythmia in adults. Neurophotonics 9 (03). https://doi.org/10.1117/1.NPh.9.3.035004.
Lawrence, W.G., et al., 2008. A comparison of avalanche photodiode and photomultiplier tube detectors for flow cytometry. In: Proceedings of the Biomedical Optics (BiOS) 2008. San Jose, CA, p. 68590M. https://doi.org/10.1117/12.758958, 7 February.
Le Francois, E., et al., 2021. Combining time of flight and photometric stereo imaging for 3D reconstruction of discontinuous scenes. Opt. Lett. 46 (15), 3612. https://doi.org/10.1364/OL.424000.
Lee, S.Y., et al., 2019. Noninvasive optical assessment of resting-state cerebral blood flow in children with sickle cell disease. Neurophotonics 6 (3), 035006. https://doi.org/10.1117/1.NPh.6.3.035006.
Lee, S.Y., et al., 2022. Quantifying the cerebral hemometabolic response to blood transfusion in pediatric sickle cell disease with diffuse optical spectroscopies. Front. Neurol. 13, 869117 https://doi.org/10.3389/fneur.2022.869117.
Lee, K., 2020. Diffuse speckle contrast analysis (DSCA) for deep tissue blood flow monitoring. Adv. Biomed. Eng. 9 (0), 21–30. https://doi.org/10.14326/abe.9.21.
Lesage, F., Gagnon, L., Dehaes, M., 2008. Diffuse optical-MRI fusion and applications. In: Proceedings of the Biomedical Optics (BiOS) 2008. San Jose, CA, p. 68500C. https://doi.org/10.1117/12.766745, 7 February.
Li, J., et al., 2005. Noninvasive detection of functional brain activity with near-infrared diffusing-wave spectroscopy. J. Biomed. Opt. 10 (4), 044002 https://doi.org/10.1117/1.2007987.
Li, J., et al., 2008. Transient functional blood flow change in the human brain measured noninvasively by diffusing-wave spectroscopy. Opt. Lett. 33 (19), 2233. https://doi.org/10.1364/OL.33.002233.
Li, D.U., et al., 2010. Real-time fluorescence lifetime imaging system with a 32 × 32 013μm CMOS low dark-count single-photon avalanche diode array. Opt. Express 18 (10), 10257. https://doi.org/10.1364/OE.18.010257.
Li, T., et al., 2013. Simultaneous measurement of deep tissue blood flow and oxygenation using noncontact diffuse correlation spectroscopy flow-oximeter. Sci. Rep. 3 (1), 1358. https://doi.org/10.1038/srep01358.
Li, J., et al., 2017. Analytical models for time-domain diffuse correlation spectroscopy for multi-layer and heterogeneous turbid media. Biomed. Opt. Express 8 (12), 5518. https://doi.org/10.1364/BOE.8.005518.
Li, Z., et al., 2021. Quantification of blood flow index in diffuse correlation spectroscopy using long short-term memory architecture. Biomed. Opt. Express 12 (7), 4131. https://doi.org/10.1364/BOE.423777.
Li, Z., Feng, J., Jia, K., 2022. Diffusion correlation spectroscopy for tissue blood flow monitoring and its clinical applications. Laser Optoelectron. Prog. 59 (6), 0617006 https://doi.org/10.3788/LOP202259.0617006.
Lin, Y., et al., 2012. Noncontact diffuse correlation spectroscopy for noninvasive deep tissue blood flow measurement. J. Biomed. Opt. 17 (1), 010502 https://doi.org/10.1117/1.JBO.17.1.010502.
Lin, P.Y., et al., 2016. Reduced cerebral blood flow and oxygen metabolism in extremely preterm neonates with low-grade germinal matrix- intraventricular hemorrhage. Sci. Rep. 6 (1), 25903. https://doi.org/10.1038/srep25903.
Lin, F., et al., 2023. Cerebral blood flow measured by diffuse correlation spectroscopy in children with autism spectrum disorder. J. Biophotonics 16 (11), e202300151. https://doi.org/10.1002/jbio.202300151.
Lindner, C., et al., 2016. Diffuse optical characterization of the healthy human thyroid tissue and two pathological case studies. PLOS ONE.
Liu, J., et al., 2014. Quantitatively assessing flow velocity by the slope of the inverse square of the contrast values versus camera exposure time. Opt. Express 22 (16), 19327. https://doi.org/10.1364/OE.22.019327.
Liu, J., et al., 2017. Simultaneously extracting multiple parameters via multi-distance and multi-exposure diffuse speckle contrast analysis. Biomed. Opt. Express 8 (10), 4537. https://doi.org/10.1364/BOE.8.004537.
Liu, J., et al., 2017. Quantitative model of diffuse speckle contrast analysis for flow measurement. J. Biomed. Opt. 22 (7), 076016 https://doi.org/10.1117/1.JBO.22.7.076016.
Liu, T., et al., 2018. Fast blind instrument function estimation method for industrial infrared spectrometers. IEEE Trans. Ind. Inform. 1–1 https://doi.org/10.1109/TII.2018.2794449.
Liu, H., et al., 2019. DISR: deep infrared spectral restoration algorithm for robot sensing and intelligent visual tracking systems. In: Proceedings of the IEEE/RSJ International Conference on Intelligent Robots and Systems (IROS). Macau, China. IEEE, pp. 8012–8017. https://doi.org/10.1109/IROS40897.2019.8967891.
Liu, T., et al., 2020. Flexible FTIR spectral imaging enhancement for industrial robot infrared vision sensing. IEEE Trans. Ind. Inform. 16 (1), 544–554. https://doi.org/10.1109/TII.2019.2934728.
Liu, W., et al., 2021. Fast and sensitive diffuse correlation spectroscopy with highly parallelized single photon detection. APL Photonics 6 (2), 026106. https://doi.org/10.1063/5.0031225.
Liu, X., et al., 2021. Deep learning in ECG diagnosis: a review. Knowl. Based Syst. 227, 107187 https://doi.org/10.1016/j.knosys.2021.107187.
Liu, X., et al., 2024. Wearable fiber-free optical sensor for continuous monitoring of neonatal cerebral blood flow and oxygenation. Pediatr. Res. 1–8. https://doi.org/10.1038/s41390-024-03137-z.
Ljungberg, M., Pretorius, P.H., 2018. SPECT/CT: an update on technological developments and clinical applications. BJR 91 (1081), 20160402. https://doi.org/10.1259/bjr.20160402.
https://lsinstruments.ch/en/products/lsi-correlator, 2024.
Ma, K.F., et al., 2019. A systematic review of diagnostic techniques to determine tissue perfusion in patients with peripheral arterial disease. Expert Rev. Med. Devices 16 (8), 697–710. https://doi.org/10.1080/17434440.2019.1644166.
Ma, W., et al., 2021. Deep learning for the design of photonic structures. Nat. Photonics 15 (2), 77–90. https://doi.org/10.1038/s41566-020-0685-y.
Magatti, D., Ferri, F., 2001. Fast multi-tau real-time software correlator for dynamic light scattering. Appl. Opt. 40 (24), 4011. https://doi.org/10.1364/AO.40.004011.

Magatti, D., Ferri, F., 2003. 25 ns software correlator for photon and fluorescence correlation spectroscopy. Rev. Sci. Instrum. 74 (2), 1135–1144. https://doi.org/10.1063/1.1525876.
Maret, G., Wolf, P.E., 1987. Multiple light scattering from disordered media. The effect of brownian motion of scatterers. Z. Phys. B Condens. Matter 65 (4), 409–413. https://doi.org/10.1007/BF01303762.
Marrero, A., et al., 2011. Aminolevulinic acid-photodynamic therapy combined with topically applied vascular disrupting agent vadimezan leads to enhanced antitumor responses. Photochem. Photobiol. 87 (4), 910–919. https://doi.org/10.1111/j.1751-1097.2011.00943.x.
Martelli, F., et al., 2016. There's plenty of light at the bottom: statistics of photon penetration depth in random media. Sci. Rep. 6 (1), 27057. https://doi.org/10.1038/srep27057.
Mater, A.C., Coote, M.L., 2019. Deep learning in chemistry. J. Chem. Inf. Model. 59 (6), 2545–2559. https://doi.org/10.1021/acs.jcim.9b00266.
Matsuda, Y., et al., 2022. Evaluation of local skeletal muscle blood flow in manipulative therapy by diffuse correlation spectroscopy. Front. Bioeng. Biotechnol. 9, 800051 https://doi.org/10.3389/fbioe.2021.800051.
Mattioli della Rocca, F.M., et al., 2023. Field programmable gate array compression for large array multispeckle diffuse correlation spectroscopy. J. Biomed. Opt. 28 (05) https://doi.org/10.1117/1.JBO.28.5.057001.
Mattioli della Rocca, F.M., et al., 2024. A 512x512 SPAD laser speckle autocorrelation imager in stacked 65/40nm CMOS. IEEE Symposium on VLSI Technology & Circuits, Honolulu, Hawaii, 16-20 June 2024.
Mazumder, D., et al., 2021. Optimization of time domain diffuse correlation spectroscopy parameters for measuring brain blood flow. Neurophotonics 8 (03). https://doi.org/10.1117/1.NPh.8.3.035005.
Menon, C., et al., 2003. An integrated approach to measuring tumor oxygen status using human melanoma xenografts as a model. Cancer Res. 63 (21), 7232–7240.
Mesquita, R.C., et al., 2011. Direct measurement of tissue blood flow and metabolism with diffuse optics. Philos. Trans. R. Soc. A 369 (1955), 4390–4406. https://doi.org/10.1098/rsta.2011.0232.
Mesquita, R.C., et al., 2013. Diffuse optical characterization of an exercising patient group with peripheral artery disease. J. Biomed. Opt. 18 (5), 057007 https://doi.org/10.1117/1.JBO.18.5.057007.
Mesquita, R.C., et al., 2013. Blood flow and oxygenation changes due to low-frequency repetitive transcranial magnetic stimulation of the cerebral cortex. J. Biomed. Opt. 18 (6), 067006 https://doi.org/10.1117/1.JBO.18.6.067006.
Mesquita, R.C., et al., 2013. Optical monitoring and detection of spinal cord ischemia. PLoS ONE 8 (12), e83370. J. A. Coles, Ed. 10.1371/journal.pone.0083370.
Milej, D., et al., 2020. Characterizing dynamic cerebral vascular reactivity using a hybrid system combining time-resolved near-infrared and diffuse correlation spectroscopy. Biomed. Opt. Express 11 (8), 4571. https://doi.org/10.1364/BOE.392113.
Milej, D., et al., 2020. Direct assessment of extracerebral signal contamination on optical measurements of cerebral blood flow, oxygenation, and metabolism. Neurophotonics 7 (04). https://doi.org/10.1117/1.NPh.7.4.045002.
Moka, S., et al., 2022. Frequency domain diffuse correlation spectroscopy: a new method for simultaneous estimation of static and dynamic tissue optical properties. In: Proceedings of the Multiscale Imaging and Spectroscopy III. San Francisco, United States. SPIE, p. 20. https://doi.org/10.1117/12.2610115. K. C. Maitland, D. M. Roblyer, and P. J. Campagnola, Eds.
Moore, C.H., Lin, W., 2022. FPGA correlator for applications in embedded smart devices. Biosensors 12 (4), 236. https://doi.org/10.3390/bios12040236.
C. Moore, U. Sunar, and W. Lin, "A device-on-chip solution for real-time diffuse correlation spectroscopy using FPGA" (2024) doi: 10.20944/preprints202405.0056.v1.
Morimoto, K., et al., 2020. Megapixel time-gated SPAD image sensor for 2D and 3D imaging applications. Optica 7 (4), 346. https://doi.org/10.1364/OPTICA.386574.
Mosconi, D., et al., 2006. CMOS single-photon avalanche diode array for time-resolved fluorescence detection. In: Proceedings of the 32nd European Solid-State Circuits Conference 2006. Montreux. IEEE, pp. 564–567. https://doi.org/10.1109/ESSCIR.2006.307487.
Munk, N., et al., 2012. Noninvasively measuring the hemodynamic effects of massage on skeletal muscle: a novel hybrid near-infrared diffuse optical instrument. J. Bodywork Mov. Ther. 16 (1), 22–28. https://doi.org/10.1016/j.jbmt.2011.01.018.
Nakabayashi, M., et al., 2023. Deep-learning-based separation of shallow and deep layer blood flow rates in diffuse correlation spectroscopy. Biomed. Opt. Express 14 (10), 5358. https://doi.org/10.1364/BOE.498693.
Niclass, C., et al., 2005. Design and characterization of a CMOS 3-D image sensor based on single photon avalanche diodes. IEEE J. Solid-State Circuits 40 (9), 1847–1854. https://doi.org/10.1109/JSSC.2005.848173.
Nourhashemi, M., et al., 2023. Preictal neuronal and vascular activity precedes the onset of childhood absence seizure: direct current potential shifts and their correlation with hemodynamic activity. Neurophotonics 10 (2), 025005. https://doi.org/10.1117/1.NPh.10.2.025005.
Ohuma, E.O., et al., 2023. National, regional, and global estimates of preterm birth in 2020, with trends from 2010: a systematic analysis. Lancet 402 (10409), 1261–1271. https://doi.org/10.1016/S0140-6736(23)00878-4.
Ozana, N., et al., 2021. Superconducting nanowire single-photon sensing of cerebral blood flow. Neurophotonics 8 (03). https://doi.org/10.1117/1.NPh.8.3.035006.
Ozana, N., et al., 2022. Functional time domain diffuse correlation spectroscopy. Front. Neurosci. 16, 932119 https://doi.org/10.3389/fnins.2022.932119.
Pagliazzi, M., et al., 2017. Time domain diffuse correlation spectroscopy with a high coherence pulsed source: *in vivo* and phantom results. Biomed. Opt. Express 8 (11), 5311. https://doi.org/10.1364/BOE.8.005311.
Pagliazzi, M., et al., 2018. *In vivo* time-gated diffuse correlation spectroscopy at quasi-null source-detector separation. Opt. Lett. 43 (11), 2450. https://doi.org/10.1364/OL.43.002450.
Parfentyeva, V., et al., 2023. Fast time-domain diffuse correlation spectroscopy with superconducting nanowire single-photon detector: system validation and *in vivo* results. Sci. Rep. 13 (1), 11982. https://doi.org/10.1038/s41598-023-39281-5.
Pasley, B.N., Freeman, R.D., 2008. Neurovascular coupling. Scholarpedia 3 (3), 5340. https://doi.org/10.4249/scholarpedia.5340.
https://www.photon-force.com/, 2024.
Pine, D.J., et al., 1990. Diffusing-wave spectroscopy: dynamic light scattering in the multiple scattering limit. J. Phys. Fr. 51 (18), 2101–2127. https://doi.org/10.1051/jphys:0199000510180210100.
Poon, C.S., Long, F., Sunar, U., 2020. Deep learning model for ultrafast quantification of blood flow in diffuse correlation spectroscopy. Biomed. Opt. Express 11 (10), 5557. https://doi.org/10.1364/BOE.402508.
Poon, C.S., et al., 2022. First-in-clinical application of a time-gated diffuse correlation spectroscopy system at 1064 nm using superconducting nanowire single photon detectors in a neuro intensive care unit. Biomed. Opt. Express 13 (3), 1344. https://doi.org/10.1364/BOE.448135.
Pope, C.G., Stevens, M.F., 1953. Preliminary communication. Lancet 262 (6797), 1190. https://doi.org/10.1016/S0140-6736(53)90736-3.
https://www.who.int/news-room/fact-sheets/detail/preterm-birth. Accessed August 21, 2023.
Quaresima, V., Bisconti, S., Ferrari, M., 2012. A brief review on the use of functional near-infrared spectroscopy (fNIRS) for language imaging studies in human newborns and adults. Brain Lang. 121 (2), 79–89. https://doi.org/10.1016/j.bandl.2011.03.009.
Quaresima, V., et al., 2019. Diffuse correlation spectroscopy and frequency-domain near-infrared spectroscopy for measuring microvascular blood flow in dynamically exercising human muscles. J. Appl. Physiol. 127 (5), 1328–1337. https://doi.org/10.1152/japplphysiol.00324.2019.
Rajan, V., et al., 2009. Review of methodological developments in laser Doppler flowmetry. Lasers Med. Sci. 24 (2), 269–283. https://doi.org/10.1007/s10103-007-0524-0.
Rajaram, A., et al., 2020. Perfusion and metabolic neuromonitoring during ventricular taps in infants with post-hemorrhagic ventricular dilatation. Brain Sci. 10 (7), 452. https://doi.org/10.3390/brainsci10070452.
Rajaram, A., et al., 2022. Assessing cerebral blood flow, oxygenation and cytochrome c oxidase stability in preterm infants during the first 3 days after birth. Sci. Rep. 12 (1), 181. https://doi.org/10.1038/s41598-021-03830-7.
Rhee, C.J., et al., 2018. Neonatal cerebrovascular autoregulation. Pediatr. Res. 84 (5), 602–610. https://doi.org/10.1038/s41390-018-0141-6.
Richardson, J.A., Grant, L.A., Henderson, R.K., 2009. Low dark count single-photon avalanche diode structure compatible with standard nanometer scale CMOS technology. IEEE Photonics Technol. Lett. 21 (14), 1020–1022. https://doi.org/10.1109/LPT.2009.2022059.
Richardson, J., et al., 2009. A 32×32 50ps resolution 10 bit time to digital converter array in 130nm CMOS for time correlated imaging. Presented at the 2009. IEEE Custom Integrated Circuits Conference, pp. 77–80. https://doi.org/10.1109/CICC.2009.5280890.
Robinson, M.B., et al., 2020. Interferometric diffuse correlation spectroscopy improves measurements at long source–detector separation and low photon count rate. J. Biomed. Opt. 25 (09) https://doi.org/10.1117/1.JBO.25.9.097004.
Robinson, M.B., et al., 2023. Portable, high speed blood flow measurements enabled by long wavelength, interferometric diffuse correlation spectroscopy (LW-iDCS). Sci. Rep. 13 (1), 8803. https://doi.org/10.1038/s41598-023-36074-8.
M. B. Robinson et al., "Pathlength-selective, interferometric diffuse correlation spectroscopy (PaLS-iDCS)" (2024) doi: 10.1101/2024.06.21.600096.
Robinson, M.B., et al., 2024. Comparing the performance potential of speckle contrast optical spectroscopy and diffuse correlation spectroscopy for cerebral blood flow monitoring using Monte Carlo simulations in realistic head geometries. Neurophotonics 11 (01). https://doi.org/10.1117/1.NPh.11.1.015004.
Roche-Labarbe, N., et al., 2010. Noninvasive optical measures of CBV, StO2, CBF index, and rCMRO2 in human premature neonates' brains in the first six weeks of life. Hum. Brain Mapp. 31 (3), 341–352. https://doi.org/10.1002/hbm.20868.
Ruesch, A., et al., 2020. Estimating intracranial pressure using pulsatile cerebral blood flow measured with diffuse correlation spectroscopy. Biomed. Opt. Express 11 (3), 1462. https://doi.org/10.1364/BOE.386612.
Safi, A.M., et al., 2021. Quantitative measurement of static and dynamic tissue optical properties with continuous wave pathlength resolved diffuse correlation spectroscopy. In: Proceedings of the Biophotonics Congress 2021. Washington, DC. Optica Publishing Group, p. BTh1B.6. https://doi.org/10.1364/BRAIN.2021.BTh1B.6.
Samaei, S., et al., 2021. Time-domain diffuse correlation spectroscopy (TD-DCS) for noninvasive, depth-dependent blood flow quantification in human tissue *in vivo*. Sci. Rep. 11 (1), 1817. https://doi.org/10.1038/s41598-021-81448-5.
Samaei, S., et al., 2021. New hybrid time-domain device for diffuse correlation spectroscopy and near-infrared spectroscopy for brain hemodynamic assessment. Diffuse Optical Spectroscopy and Imaging VIII. SPIE, Germany, p. 7. https://doi.org/10.1117/12.2615209. D. Contini, Y. Hoshi, and T. D. O'Sullivan, Eds.Online Only.
Samaei, S., et al., 2021. Performance assessment of laser sources for time-domain diffuse correlation spectroscopy. Biomed. Opt. Express 12 (9), 5351. https://doi.org/10.1364/BOE.432363.
Samaei, S., et al., 2022. Continuous-wave parallel interferometric near-infrared spectroscopy (CW πNIRS) with a fast two-dimensional camera. Biomed. Opt. Express 13 (11), 5753. https://doi.org/10.1364/BOE.472643.

Sathialingam, E., et al., 2018. Small separation diffuse correlation spectroscopy for measurement of cerebral blood flow in rodents. Biomed. Opt. Express 9 (11), 5719. https://doi.org/10.1364/BOE.9.005719.
Sathialingam, E., et al., 2023. Microvascular cerebral blood flow response to intrathecal nicardipine is associated with delayed cerebral ischemia. Front. Neurol. 14 https://doi.org/10.3389/fneur.2023.1052232. Frontiers.
Schätzel, K., Drewel, M., Stimac, S., 1988. Photon correlation measurements at large lag times: improving statistical accuracy. J. Mod. Opt. 35 (4), 711–718. https://doi.org/10.1080/09500348814550731.
Schätzel, K., 1983. Noise in photon correlation and photon structure functions. Opt. Acta Int. J. Opt. 30 (2), 155–166. https://doi.org/10.1080/713821145.
Schätzel, K., 1987. Correlation techniques in dynamic light scattering. Appl. Phys. B 42 (4), 193–213. https://doi.org/10.1007/BF00693937.
Schatzel, K., 1990. Noise on photon correlation data. I. Autocorrelation functions. Quantum Opt. 2 (4), 287–305. https://doi.org/10.1088/0954-8998/2/4/002.
Schober, P., Schwarte, L.A., 2012. From system to organ to cell: oxygenation and perfusion measurement in anesthesia and critical care. J. Clin. Monit. Comput. 26 (4), 255–265. https://doi.org/10.1007/s10877-012-9350-4.
Schuck, C., et al., 2013. Matrix of integrated superconducting single-photon detectors with high timing resolution. IEEE Trans. Appl. Supercond. 23 (3), 2201007 https://doi.org/10.1109/TASC.2013.2239346. –2201007.
Shang, Y., Yu, G., 2014. A N th-order linear algorithm for extracting diffuse correlation spectroscopy blood flow indices in heterogeneous tissues. Appl. Phys. Lett. 105 (13), 133702 https://doi.org/10.1063/1.4896992.
Shang, Y., Yu, G., 2014. A Nth-order linear algorithm for extracting diffuse correlation spectroscopy blood flow indices in heterogeneous tissues. Appl. Phys. Lett. 105 (13), 133702 https://doi.org/10.1063/1.4896992.
Shang, Y., et al., 2009. Portable optical tissue flow oximeter based on diffuse correlation spectroscopy. Opt. Lett. 34 (22), 3556. https://doi.org/10.1364/OL.34.003556.
Shang, Y., et al., 2010. Effects of muscle fiber motion on diffuse correlation spectroscopy blood flow measurements during exercise. Biomed. Opt. Express 1 (2), 500. https://doi.org/10.1364/BOE.1.000500.
Shang, Y., et al., 2011. Cerebral monitoring during carotid endarterectomy using near-infrared diffuse optical spectroscopies and electroencephalogram. Phys. Med. Biol. 56 (10), 3015. https://doi.org/10.1088/0031-9155/56/10/008.
Shang, Y., et al., 2011. Diffuse optical monitoring of repeated cerebral ischemia in mice. Opt. Express 19 (21), 20301. https://doi.org/10.1364/OE.19.020301.
Shang, Y., et al., 2012. Noninvasive optical characterization of muscle blood flow, oxygenation, and metabolism in women with fibromyalgia. Arthritis Res. Ther. 14 (6), R236. https://doi.org/10.1186/ar4079.
Shang, Y., et al., 2014. Extraction of diffuse correlation spectroscopy flow index by integration of N th-order linear model with Monte Carlo simulation. Appl. Phys. Lett. 104 (19), 193703 https://doi.org/10.1063/1.4876216.
Shang, Y., Li, T., Yu, G., 2017. Clinical applications of near-infrared diffuse correlation spectroscopy and tomography for tissue blood flow monitoring and imaging. Physiol. Meas. 38 (4), R1–R26. https://doi.org/10.1088/1361-6579/aa60b7.
Shaw, K., et al., 2023. The use of novel diffuse optical spectroscopies for improved neuromonitoring during neonatal cardiac surgery requiring antegrade cerebral perfusion. Front. Pediatr. 11, 1125985 https://doi.org/10.3389/fped.2023.1125985.
Shepherd, A.P., Öberg, P.Å., 2013. Laser-Doppler Blood Flowmetry. Springer Science & Business Media.
Shoemaker, L., et al., 2023. Using depth-enhanced diffuse correlation spectroscopy and near-infrared spectroscopy to isolate cerebral hemodynamics during transient hypotension. Neurophotonics 10 (2), 025013. https://doi.org/10.1117/1.NPh.10.2.025013.
Sie, E.J., et al., 2020. High-sensitivity multispeckle diffuse correlation spectroscopy. Neurophotonics 7 (03). https://doi.org/10.1117/1.NPh.7.3.035010.
Stapels, C.J., et al., 2016. A scalable correlator for multichannel diffuse correlation spectroscopy. In: Proceedings of the SPIE BiOS. San Francisco, California, United States, 969816. https://doi.org/10.1117/12.2213114, 7 March.
Stephen, M.J., 1988. Temporal fluctuations in wave propagation in random media. Phys. Rev. B 37 (1), 1–5. https://doi.org/10.1103/PhysRevB.37.1.
Stoppa, D., et al., 2007. A CMOS 3-D imager based on single photon avalanche diode. IEEE Trans. Circuits Syst. I 54 (1), 4–12. https://doi.org/10.1109/TCSI.2006.888679.
Sunar, U., et al., 2006. Noninvasive diffuse optical measurement of blood flow and blood oxygenation for monitoring radiation therapy in patients with head and neck tumors: a pilot study. J. Biomed. Opt. 11 (6), 064021 https://doi.org/10.1117/1.2397548.
Sunar, U., et al., 2007. Hemodynamic responses to antivascular therapy and ionizing radiation assessed by diffuse optical spectroscopies. Opt. Express 15 (23), 15507. https://doi.org/10.1364/OE.15.015507.
Sunar, U., et al., 2010. Monitoring photobleaching and hemodynamic responses to HPPH-mediated photodynamic therapy of head and neck cancer: a case report. Opt. Express 18 (14), 14969. https://doi.org/10.1364/OE.18.014969.
Sunwoo, J., et al., 2022. Diffuse correlation spectroscopy blood flow monitoring for intraventricular hemorrhage vulnerability in extremely low gestational age newborns. Sci. Rep. 12 (1), 12798. https://doi.org/10.1038/s41598-022-16499-3.
Sutin, J., et al., 2016. Time-domain diffuse correlation spectroscopy. Optica 3 (9), 1006. https://doi.org/10.1364/OPTICA.3.001006.
Sutin, J., et al., 2023. Association of cerebral metabolic rate following therapeutic hypothermia with 18-month neurodevelopmental outcomes after neonatal hypoxic ischemic encephalopathy. eBioMedicine 94. https://doi.org/10.1016/j.ebiom.2023.104673.
Tagliabue, S., et al., 2023. Comparison of cerebral metabolic rate of oxygen, blood flow, and bispectral index under general anesthesia. Neurophotonics 10 (01). https://doi.org/10.1117/1.NPh.10.1.015006.
Tamborini, D., et al., 2019. Portable system for time-domain diffuse correlation spectroscopy. IEEE Trans. Biomed. Eng. 66 (11), 3014–3025. https://doi.org/10.1109/TBME.2019.2899762.
Tellis, G.M., Mesquita, R.C., Yodh, A.G., 2018. Use of Diffuse Correlation Spectroscopy To Measure Brain Blood Flow Differences During Speaking and Nonspeaking Tasks for Fluent Speakers and Persons Who Stutter. ASHA Wire. https://doi.org/10.1044/ffd21.3.96, 30 Decemberaccessed 22 July 2024.
Tupprasoot, R., Blaise, B.J., 2023. Continuous cerebral blood flow monitoring: what should we do with these extra numbers? BJA Open 7, 100148. https://doi.org/10.1016/j.bjao.2023.100148.
Udina, C., et al., 2022. Dual-task related frontal cerebral blood flow changes in older adults with mild cognitive impairment: a functional diffuse correlation spectroscopy study. Front. Aging Neurosci. 14, 958656 https://doi.org/10.3389/fnagi.2022.958656.
Uludağ, K., et al., 2004. Coupling of cerebral blood flow and oxygen consumption during physiological activation and deactivation measured with fMRI. NeuroImage 23 (1), 148–155. https://doi.org/10.1016/j.neuroimage.2004.05.013.
Valdes, C.P., et al., 2014. Speckle contrast optical spectroscopy, a non-invasive, diffuse optical method for measuring microvascular blood flow in tissue. Biomed. Opt. Express 5 (8), 2769. https://doi.org/10.1364/BOE.5.002769.
Van de Hulst, H.C., 1981. Light Scattering by Small Particles. Dover, New York, NY.
Vapnik, V.N., 1999. An overview of statistical learning theory. IEEE Trans. Neural Netw. 10 (5), 988–999. https://doi.org/10.1109/72.788640.
Vaquero, J.J., Kinahan, P., 2015. Positron emission tomography: current challenges and opportunities for technological advances in clinical and preclinical imaging systems. Annu. Rev. Biomed. Eng. 17 (1), 385–414. https://doi.org/10.1146/annurev-bioeng-071114-040723.
Veerappan, C., et al., 2011. A 160×128 single-photon image sensor with on-pixel 55ps 10b time-to-digital converter. In: Proceedings of the IEEE International Solid-State Circuits Conference. San Francisco, CA, USA. IEEE, pp. 312–314. https://doi.org/10.1109/ISSCC.2011.5746333.
Verdecchia, K., et al., 2013. Quantifying the cerebral metabolic rate of oxygen by combining diffuse correlation spectroscopy and time-resolved near-infrared spectroscopy. J. Biomed. Opt. 18 (2), 027007 https://doi.org/10.1117/1.JBO.18.2.027007.
Verdecchia, K., et al., 2016. Assessment of a multi-layered diffuse correlation spectroscopy method for monitoring cerebral blood flow in adults. Biomed. Opt. Express 7 (9), 3659. https://doi.org/10.1364/BOE.7.003659.
Villa, F., et al., 2012. SPAD smart pixel for time-of-flight and time-correlated single-photon counting measurements. IEEE Photonics J. 4 (3), 795–804. https://doi.org/10.1109/JPHOT.2012.2198459.
Villa, F., et al., 2014. CMOS imager with 1024 SPADs and TDCs for single-photon timing and 3-D time-of-flight. IEEE J. Sel. Top. Quantum Electron. 20 (6), 364–373. https://doi.org/10.1109/JSTQE.2014.2342197.
Villringer, A., Chance, B., 1997. Non-invasive optical spectroscopy and imaging of human brain function. Trends Neurosci. 20 (10), 435–442. https://doi.org/10.1016/S0166-2236(97)01132-6.
Vo-Dinh, T., 2014. Biomedical Photonics Handbook: Biomedical Diagnostics. CRC Press.
Von Lühmann, A., et al., 2020. Using the general linear model to improve performance in fNIRS single trial analysis and classification: a perspective. Front. Hum. Neurosci. 14, 30. https://doi.org/10.3389/fnhum.2020.00030.
M. Wahl and P. GmbH, "Time-correlated single photon counting" (2009).
Wang, L., Jacques, S.L., 1995. Monte Carlo modeling of light transport in multi-layered tissues in standard C. Comput. Methods Programs Biomed. 47 (2), 131–146.
Wang, L., Jacques, S.L., Zheng, L., 1995. MCML–Monte Carlo modeling of light transport in multi-layered tissues. Comput. Methods Programs Biomed. 47 (2), 131–146. https://doi.org/10.1016/0169-2607(95)01640-f.
Wang, D., et al., 2016. Fast blood flow monitoring in deep tissues with real-time software correlators. Biomed. Opt. Express 7 (3), 776. https://doi.org/10.1364/BOE.7.000776.
Wang, Y., et al., 2023. High-resolution time-to-digital converters (TDCs) with a bidirectional encoder. Measurement 206, 112258. https://doi.org/10.1016/j.measurement.2022.112258.
Wang, Q., et al., 2024. Quantification of blood flow index in diffuse correlation spectroscopy using a robust deep learning method. J. Biomed. Opt. 29 (01) https://doi.org/10.1117/1.JBO.29.1.015004.
Wang, Y., et al., 2024. A two-stage interpolation time-to-digital converter implemented in 20 and 28 nm FGPAs. IEEE Trans. Ind. Electron. 1–11. https://doi.org/10.1109/TIE.2024.3370941.
Wayne, M.A., et al., 2023. Massively parallel, real-time multispeckle diffuse correlation spectroscopy using a 500 × 500 SPAD camera. Biomed. Opt. Express 14 (2), 703. https://doi.org/10.1364/BOE.473992.
Weigl, W., et al., 2016. Application of optical methods in the monitoring of traumatic brain injury: a review. J. Cereb. Blood Flow Metab. 36 (11), 1825–1843. https://doi.org/10.1177/0271678X16667953.
White, S.M., et al., 2012. Longitudinal *in vivo* imaging to assess blood flow and oxygenation in implantable engineered tissues. Tissue Eng. Part C Methods 18 (9), 697–709. https://doi.org/10.1089/ten.tec.2011.0744.
Wintermark, M., et al., 2005. Comparative overview of brain perfusion imaging techniques. Stroke 36 (9). https://doi.org/10.1161/01.STR.0000177884.72657.8b.
Wolf, U., et al., 2003. Localized irregularities in hemoglobin flow and oxygenation in calf muscle in patients with peripheral vascular disease detected with near-infrared

spectrophotometry. J. Vasc. Surg. 37 (5), 1017–1026. https://doi.org/10.1067/mva.2003.214.
Wu, K.C., et al., 2021. Validation of diffuse correlation spectroscopy measures of critical closing pressure against transcranial Doppler ultrasound in stroke patients. J. Biomed. Opt. 26 (3), 036008 https://doi.org/10.1117/1.JBO.26.3.036008.
Wu, J., et al., 2022. Two-layer analytical model for estimation of layer thickness and flow using diffuse correlation spectroscopy. PLoS ONE 17 (9), e0274258. A. Dalla Mora, Ed. 10.1371/journal.pone.0274258.
Wu, K.C., et al., 2023. Enhancing diffuse correlation spectroscopy pulsatile cerebral blood flow signal with near-infrared spectroscopy photoplethysmography. Neurophotonics 10 (03). https://doi.org/10.1117/1.NPh.10.3.035008.
Wu, M.M., Horstmeyer, R., Carp, S.A., 2023. scatterBrains: an open database of human head models and companion optode locations for realistic Monte Carlo photon simulations. J. Biomed. Opt. 28 (10) https://doi.org/10.1117/1.JBO.28.10.100501.
Xiao, D., et al., 2021. Dynamic fluorescence lifetime sensing with CMOS single-photon avalanche diode arrays and deep learning processors. Biomed. Opt. Express 12 (6), 3450. https://doi.org/10.1364/BOE.425663.
Xu, J., et al., 2020. Interferometric speckle visibility spectroscopy (ISVS) for human cerebral blood flow monitoring. APL Photonics 5 (12), 126102. https://doi.org/10.1063/5.0021988.
Xu, S., et al., 2022. Imaging dynamics beneath turbid media via parallelized single-photon detection. Adv. Sci. 9 (24), 2201885 https://doi.org/10.1002/advs.202201885.
Xu, S., et al., 2022. Transient Motion classification through turbid volumes via parallelized single-photon detection and deep contrastive embedding. Front. Neurosci. 16, 908770 https://doi.org/10.3389/fnins.2022.908770.
Yazdi, H.S., et al., 2017. Mapping breast cancer blood flow index, composition, and metabolism in a human subject using combined diffuse optical spectroscopic imaging and diffuse correlation spectroscopy. J. Biomed. Opt. 22 (4), 045003 https://doi.org/10.1117/1.JBO.22.4.045003.
Yeo, C., et al., 2016. Avian embryo monitoring during incubation using multi-channel diffuse speckle contrast analysis. Biomed. Opt. Express 7 (1), 93. https://doi.org/10.1364/BOE.7.000093.
Yeo, C., Kim, H., Song, C., 2017. Cerebral blood flow monitoring by diffuse speckle contrast analysis during MCAO surgery in the rat. Curr. Opt. Photonics 1 (5), 433–439. https://doi.org/10.3807/COPP.2017.1.5.433.
Yodh, A.G., Kaplan, P.D., Pine, D.J., 1990. Pulsed diffusing-wave spectroscopy: high resolution through nonlinear optical gating. Phys. Rev. B 42 (7), 4744–4747. https://doi.org/10.1103/PhysRevB.42.4744.
Yonas, H., Pindzola, R.R., Johnson, D.W., 1996. Xenon/computed tomography cerebral blood flow and its use in clinical management. Neurosurg. Clin. N. Am. 7 (4), 605–616. https://doi.org/10.1016/S1042-3680(18)30349-8.
Yu, G., et al., 2005. Noninvasive monitoring of murine tumor blood flow during and after photodynamic therapy provides early assessment of therapeutic efficacy. Clin. Cancer Res. 11 (9), 3543–3552. https://doi.org/10.1158/1078-0432.CCR-04-2582.
Yu, G., et al., 2005. Time-dependent blood flow and oxygenation in human skeletal muscles measured with noninvasive near-infrared diffuse optical spectroscopies. J. Biomed. Opt. 10 (2), 024027 https://doi.org/10.1117/1.1884603.
Yu, G., et al., 2006. Real-time *in situ* monitoring of human prostate photodynamic therapy with diffuse light. Photochem. Photobiol. 82 (5), 1279. https://doi.org/10.1562/2005-10-19-RA-721.
Yu, G., et al., 2007. Validation of diffuse correlation spectroscopy for muscle blood flow with concurrent arterial spin labeled perfusion MRI. Opt. Express 15 (3), 1064. https://doi.org/10.1364/OE.15.001064.
Yu, G., et al., 2011. Intraoperative evaluation of revascularization effect on ischemic muscle hemodynamics using near-infrared diffuse optical spectroscopies. J. Biomed. Opt. 16 (2), 027004 https://doi.org/10.1117/1.3533320.
Yu, G., 2012. Diffuse Correlation Spectroscopy (DCS): a diagnostic tool for assessing tissue blood flow in vascular-related diseases and therapies. CMIR 8 (3), 194–210. https://doi.org/10.2174/157340512803759875.
Yu, G., 2012. Near-infrared diffuse correlation spectroscopy in cancer diagnosis and therapy monitoring. J. Biomed. Opt. 17 (1), 010901 https://doi.org/10.1117/1.JBO.17.1.010901.
Zauner, A., et al., 2002. Brain oxygenation and energy metabolism: part I–biological function and pathophysiology. Neurosurgery 51 (2), 289.
Zavriyev, A.I., et al., 2021. The role of diffuse correlation spectroscopy and frequency-domain near-infrared spectroscopy in monitoring cerebral hemodynamics during hypothermic circulatory arrests. JTCVS Tech. 7, 161–177. https://doi.org/10.1016/j.xjtc.2021.01.023.
Zhang, P., et al., 2018. Approaches to denoise the diffuse optical signals for tissue blood flow measurement. Biomed. Opt. Express 9 (12), 6170. https://doi.org/10.1364/BOE.9.006170.
Zhang, P., et al., 2019. Signal processing for diffuse correlation spectroscopy with recurrent neural network of deep learning. In: Proceedings of the IEEE Fifth International Conference on Big Data Computing Service and Applications (BigDataService). Newark, CA, USA. IEEE, pp. 328–332. https://doi.org/10.1109/BigDataService.2019.00058.
Zhang, Y., et al., 2020. An investigation of deep learning models for EEG-based emotion recognition. Front. Neurosci. 14, 622759 https://doi.org/10.3389/fnins.2020.622759.
Zhao, H., Sathialingam, E., Buckley, E.M., 2021. Accuracy of diffuse correlation spectroscopy measurements of cerebral blood flow when using a three-layer analytical model. Biomed. Opt. Express 12 (11), 7149. https://doi.org/10.1364/BOE.438303.
Zhao, Y., et al., 2021. NIRS-ICA: a MATLAB toolbox for independent component analysis applied in fNIRS studies. Front. Neuroinform. 15, 683735 https://doi.org/10.3389/fninf.2021.683735.
Zhao, H., et al., 2023. Comparison of diffuse correlation spectroscopy analytical models for measuring cerebral blood flow in adults. J. Biomed. Opt. 28 (12) https://doi.org/10.1117/1.JBO.28.12.126005.
Zhou, C., et al., 2006. Diffuse optical correlation tomography of cerebral blood flow during cortical spreading depression in rat brain. Opt. Express 14 (3), 1125. https://doi.org/10.1364/OE.14.001125.
Zhou, C., et al., 2007. Diffuse optical monitoring of blood flow and oxygenation in human breast cancer during early stages of neoadjuvant chemotherapy. J. Biomed. Opt. 12 (5), 051903 https://doi.org/10.1117/1.2798595.
Zhou, C., et al., 2009. Diffuse optical monitoring of hemodynamic changes in piglet brain with closed head injury. J. Biomed. Opt. 14 (3), 034015 https://doi.org/10.1117/1.3146814.
Zhou, W., et al., 2018. Highly parallel, interferometric diffusing wave spectroscopy for monitoring cerebral blood flow dynamics. Optica 5 (5), 518. https://doi.org/10.1364/OPTICA.5.000518.
Zhou, W., et al., 2021. Multi-exposure interferometric diffusing wave spectroscopy. Opt. Lett. 46 (18), 4498. https://doi.org/10.1364/OL.427746.
Zhou, W., et al., 2021. Functional interferometric diffusing wave spectroscopy of the human brain. Sci. Adv. 7 (20), eabe0150. https://doi.org/10.1126/sciadv.abe0150.
Zhou, W., Zhao, M., Srinivasan, V.J., 2022. Interferometric diffuse optics: recent advances and future outlook. Neurophotonics 10 (01). https://doi.org/10.1117/1.NPh.10.1.013502.
C. Zhou, "*In-vivo* optical imaging and spectroscopy of cerebral hemodynamics." (2007). PhD thesis.
Zhu, C., Liu, Q., 2013. Review of Monte Carlo modeling of light transport in tissues. J. Biomed. Opt. 18 (5), 050902 https://doi.org/10.1117/1.JBO.18.5.050902.
Zhu, Y., et al., 2020. Experimental validation of microvasculature blood flow modeling by diffuse correlation spectroscopy. IEEE Access 8, 15945–15951. https://doi.org/10.1109/ACCESS.2020.2966750.
Zilpelwar, S., et al., 2022. Model of dynamic speckle evolution for evaluating laser speckle contrast measurements of tissue dynamics. Biomed. Opt. Express 13 (12), 6533. https://doi.org/10.1364/BOE.472263.
Zirak, P., et al., 2010. Effects of acetazolamide on the micro- and macro-vascular cerebral hemodynamics: a diffuse optical and transcranial doppler ultrasound study. Biomed. Opt. Express 1 (5), 1443. https://doi.org/10.1364/BOE.1.001443.
Zirak, P., et al., 2014. Transcranial diffuse optical monitoring of microvascular cerebral hemodynamics after thrombolysis in ischemic stroke. J. Biomed. Opt. 19 (1), 018002 https://doi.org/10.1117/1.JBO.19.1.018002.